Title

Non-classical Behavior of Bethe-Zelʾdovich-Thompson Gas and Numerical Computation of Dense Gas Flow

Permalink

https://escholarship.org/uc/item/4sn14455

Author

ZENG, JINGYI

Publication Date

2023

UNIVERSITY OF CALIFORNIA,
IRVINE

Non-classical Behavior of Bethe-Zel'dovich-Thompson Gas and Numerical Computation of Dense Gas Flow

DISSERTATION

submitted in partial satisfaction of the requirements
for the degree of

DOCTOR OF PHILOSOPHY

in Mechanical and Aerospace Engineering

by

Jingyi Zeng

Dissertation Committee:
Professor Feng Liu, Chair
Professor William Sirignano
Professor Dimitri Papamoschou

2023

DEDICATION

To Mom and Dad, who made me who I am,
Whose love and guidance were my compass and map.
Through every hurdle, every trial,
You stood by my side with a steadfast smile.
Thank you for all the support and sacrifice,
And for being the best parents in every way.

TABLE OF CONTENTS

LIST OF FIGURES

Page

LIST OF TABLES

Page

ACKNOWLEDGMENTS

Completing a Ph.D. journey is not an individual accomplishment. It is the result of countless hours of hard work, support, and encouragement from a community of individuals who have made it possible. I would like to take this opportunity to express my gratitude to the people who have helped me to reach this milestone.

First and foremost, I am deeply grateful to my advisor, Feng Liu, for his unwavering support, guidance, and encouragement throughout my doctoral studies. His expertise, patience, and kindness have been instrumental in shaping my research and intellectual growth. His constructive feedback, insightful comments, and thoughtful suggestions have challenged me to be a better researcher and scholar. I am fortunate to have had such a dedicated and inspiring mentor.

I would also like to thank the members of my dissertation committee, Professor William Sirignano and Professor Dimitri Papamoschou, for their valuable feedback and constructive criticism. Their knowledge, expertise, and insights have helped me to broaden my understanding and develop a more comprehensive research project. I am grateful for their time and efforts in reviewing my work and providing me with thoughtful feedback.

I extend my heartfelt thanks to my colleagues and friends who have made my journey here more enjoyable and meaningful. Their camaraderie, intellectual discussions, and moral support have been invaluable in helping me to overcome the challenges of graduate school. I am fortunate to have met such a talented and diverse group of individuals.

Finally, I am deeply grateful to my family for their unwavering support, encouragement, and love. Their faith in me has been a constant source of motivation, and I am forever indebted to them. I am particularly grateful to my love, Siwei Wang, who has been my rock during the ups and downs of this long journey.

And, of course, I cannot forget to thank my faithful feline companion, Coco, who kept me company during all the challenging moments. I feel truly blessed to have had him by my side, and I will always cherish the memories of our time together.

In conclusion, I am grateful for the countless individuals who have contributed to my success in completing this Ph.D. study. Their support and encouragement have made this achievement possible, and I will always be thankful for their role in my life.

VITA

Jingyi Zeng

EDUCATION

Doctor of Philosophy in Mechanical and Aerospace Engineering **2023**
University of California, Irvine *Irvine, California*

Master of Science in Mechanical and Aerospace Engineering **2020**
University of California, Irvine *Irvine, California*

Bachelor of Science in Energy, Power Engineering & Automation **2016**
Xi'an Jiaotong University *Xi'an, China*

RESEARCH EXPERIENCE

Graduate Student Researcher **2016–2023**
University of California, Irvine *Irvine, California*

Research Assistant **2015–2016**
Xi'an Jiaotong University *Xi'an, China*

TEACHING EXPERIENCE

Teaching Assistant **2018–2023**
University of California, Irvine *Irvine, California*

ABSTRACT OF THE DISSERTATION

Non-classical Behavior of Bethe-Zel'dovich-Thompson Gas and Numerical Computation of Dense Gas Flow

By

Jingyi Zeng

Doctor of Philosophy in Mechanical and Aerospace Engineering

University of California, Irvine, 2023

Professor Feng Liu, Chair

In recent decades, the escalating global energy consumption has increased interest in thermodynamic power cycles, such as the Organic Rankine Cycle (ORC), which are known for their high waste heat recovery efficacy. The fluids in such power cycles have complicated molecular structures and are typically operated near the saturation vapor line and critical point. These gases exhibit similar behaviors to those investigated by Bethe (1942), who established a thermodynamic property known as the fundamental derivative (Γ), which measures the variation of the sound speed of a gas with pressure change during an isentropic process. Gases with Γ values less than 1 are referred to as Bethe-Zel'dovich-Thompson (BZT) gases and are commonly used as working fluids in the ORC. BZT gases demonstrate a range of qualitatively distinct phenomena compared to conventional gases, especially when $\Gamma < 0$. These include expansion shock waves, double sonic shock waves, compression fans, and expansion shock fans. Despite the lack of experimental evidence to confirm such non-classical gas flow behaviors, the increasing interest in using supercritical heavy gases and academic curiosity warrant further in-depth study. A comprehensive literature review of past studies on the fundamental derivative and corresponding non-classical gas behaviors is conducted.

In order to enhance the prediction accuracy of the thermodynamic properties of dense gases and address the existing gap in the availability of precise and accurate equation of state within the Bethe-Zel'dovich-Thompson (BZT) region, this research investigates the potential of machine learning algorithms' application in the thermodynamics field. By meticulously analyzing the influence of various hyperparameters, an optimized artificial neural network (ANN) model has been developed and subsequently incorporated into our in-house code, which solves the Navier-Stokes equations using a finite-volume method. The successful implementation of the optimized ANN model to calculate the thermodynamics properties demonstrates the potential to significantly decrease the reliance on traditional real gas equations of state for simulation results. This advancement offers a more robust and reliable approach to predicting thermodynamic properties, thereby contributing to the broader field of thermodynamics research.

Besides the state-of-art technology in the thermodynamics part, this study also employs the Van der Waals model to illustrate the existence of negative fundamental derivative regions for dense gases and numerically investigates the unique phenomena of dense gas flow. A numerical solver based on the Jameson-Schmidt-Turkel scheme for dense gas flow is developed, and various counter-classical gas dynamics flow behaviors of real gases in different Γ regimes are demonstrated through selected cases. The simulation results of dense gas flow across various geometries are presented and analyzed, revealing intricate wave fields.

In conjunction with the traditional density-based solvers, this study also proposes an innovative pressure-based solution methodology for compressible flow, specifically designed to address the stiffness issue encountered near the critical point due to the heightened sensitivity of pressure with respect to density. A comprehensive derivation of the novel approach is presented, emphasizing its theoretical underpinnings and practical applications.

NOMENCLATURE

A = cross-sectional area, m^2

a = measure of the average attraction between particles, $Pa \cdot m^6/kg^2$

b = the volume excluded by a mole of particles, m^3/kg

c = speed of sound, m/s

c_v = heat capacity at constant volume, J/K

c_p = heat capacity at constant pressure, J/K

e = internal energy, J

E = total energy, J

Γ = fundamental derivative

γ = specific heat ratio

h = enthalpy, J

h_0 = total enthalpy/stagnation enthalpy, J

κ = coefficient of thermal conductivity, $W/(m \cdot K)$

M = Mach number

M_g = Molecular weight, kg/mol

μ = coefficient of dynamic viscosity, $N \cdot s/m^2$

p = pressure, Pa

p_0 = total pressure/stagnation pressure, Pa

p_c = critical pressure, Pa

q = heat flux, W/m^2

R = specific gas constant, $J/(kg \cdot K)$

ρ = density, kg/m^3

ρ_0 = total density/stagnation density, kg/m^3

s = entropy, J/K

$\mathbf{S}$ = stress tensor, N/m^2

t = time, s

T = temperature, K

T_0 = total temperature/stagnation temperature, K

T_c = critical temperature, K

u = flow velocity in the x direction, m/s

v = specific volume, m^3/kg

$\mathbf{V}$ = velocity vector, m/s

Subscript:

c = property at critical conclusion

r = property ratio to that at critical conclusion

Chapter 1

Introduction

1.1 Thermo-Cycles that Use Dense Gases

Expanding urbanization and population growth are predominantly responsible for the global energy consumption increase. According to statistics from 2017[4], over 80% of the world's energy supply was derived from fossil fuels, including coal, lignite, shale, oil, and natural gas. However, the combustion of fossil fuels produces a number of deleterious byproducts, including carbon monoxide, sulfur dioxide, nitrogen oxides, ammonia, particulate matter, volatile organic compounds, and ozone[5], which have negative effects on human health and the environment. In addition, emissions of greenhouse gases from the combustion of fossil fuels are a primary contributor to global warming, which has significant environmental impacts, such as rising sea levels, increasing frequency of extreme weather events, and loss of biodiversity[6]. To address these environmental concerns and to comply with increasingly stringent regulations on greenhouse gas emissions, academics and industry professionals are investigating innovative and sustainable solutions to meet the growing energy demand. One of the critical strategies is improving the energy efficiency of the existing industrial and power generation facilities, as almost 50% of energy is wasted throughout the world during the energy consumption process[7]. Consequently, there is a developing interest in waste heat recovery technology research.

Diverse technologies have emerged in order to maximize the use of low and medium-grade thermal energy sources, such as geothermal energy, solar energy, industrial waste heat, biomass, and ocean thermal energy. The Organic Rankine Cycle (ORC)[8] has acquired popularity as one of the most promising approaches for converting low and medium-grade thermal energy into electricity. This closed-loop system employs organic fluids as working fluids to convert thermal energy into mechanical energy, which is then used to generate electricity. The ORC system has a number of advantages, including its ability to operate at low temperatures, its flexibility in adapting to varying heat sources, and its suitability for small-scale and decentralized applications. However, its operation in the vicinity of the critical point or close to the saturation vapor line poses significant challenges. In this region, the inter-molecular force plays an important role in determining the thermodynamic properties of the fluid[9], and the ideal-gas law, which neglects this force, can no longer accurately predict the behavior of the gas. Therefore, more complex equations of state are required to achieve accurate prediction[10][11][12].

Furthermore, the fluid dynamic design of efficient turbo machinery components, such as the compressor, turbine, and diffuser, becomes the most challenging aspect of power cycle design in or close to the non-ideal compressible fluid region. The design and performance analysis of conventional thermodynamics cycle components extensively relies on the ideal-gas law[13], which neglects the inter-molecular force. However, in the region close to the critical point and saturation vapor line, the inter-molecular force plays a significant role, and a considerable departure from the behavior of ideal gases is observed[9]. In this region, fluids with high molecular complexity can exhibit qualitatively distinct fluid dynamic behavior, such as expansion shock and mixed shock/fan waves[14][15]. This region is therefore commonly referred to as the nonclassical region. A comprehensive understanding of the non-ideal and nonclassical behavior of gases is of major importance for the development of more effective component design and performance analysis for engineering applications. With further research and development, innovative solutions can be implemented to resolve the challenges associated with ORC technology, such as the optimization of turbomachinery components and the selection of appropriate working fluids to achieve greater efficiency and cost-effectiveness.

To address these challenges, researchers are exploring various approaches, including machine learning algorithms, to derive a real-gas equation of state, which can provide more accurate predictions of gas properties in the non-ideal region[16]. Machine learning algorithms can learn from large data sets and identify patterns that are difficult to detect using traditional methods. The approach involves training machine learning models on a large data set of experimental or simulated gas data and then using the models to predict the thermodynamic properties of fluids under different conditions. The machine learning models can then be incorporated into a real-gas equation of state to provide more accurate predictions of gas behaviors.

In conclusion, the ever-increasing need for energy, in conjunction with the environmental challenges that are associated with the widespread consumption of fossil fuels, necessitates a holistic strategy that considers technical, economic, and policy factors. The development of waste heat recovery technologies, coupled with the effective utilization of low and medium-grade thermal energy sources, such as the ORC technology, may make a substantial contribution to the accomplishment of these goals. Additionally, the adoption of renewable energy sources, working together with the deployment of energy storage technologies, can contribute to enhancing energy security and reducing greenhouse gas emissions.

1.2 Nonclassical Gasdynamics

Thermal analysis and engineering applications often rely on the assumption of an ideal gas in the compressible flow analysis. The ideal-gas approximation provides a useful and convenient framework for analyzing gas behavior under a wide range of conditions where pressure and temperature are far from the critical point of the gas. However, as the working conditions approach the liquid-vapor saturation curve, the ideal-gas hypothesis becomes invalid, and real-gas effects need to be considered. In the region near the critical point of the gas, which is referred to as the dense gas region, the gas dynamics exhibit significant differences from those of an ideal gas. Super-critical CO_2 power cycles in turbo-machinery [17][18][19]have recently received substantial attention[17][18][19]. In such applications, a precise understanding of the behavior of dense gases and their thermal properties near or above the critical point is crucial to enhance compressor and turbine performance and stability margins[20][21]. Given the importance of understanding the behavior of dense gases, researchers have been exploring various real-gas equations of state to achieve greater accuracy in modeling gas dynamics. Among these equations of state, the Van der Waals (VdW), Soave-Redlich-Kwong (SRK), and Peng-Robinson (PR) equations of state are commonly used to achieve more accurate results. The Van der Waals equation is an early attempt to explain the behavior of real gases by considering the existence of a finite molecular size and the occurrence of molecular interactions or attractions. The SRK and PR equations of state are modifications of the VdW equation and provide more accurate predictions for real gases. Both of these equations adjust the attractive term (originally 'a' in the VdW equation) to be temperature-dependent. The choice of equation of state would depend on the specific system under consideration, including factors like the nature of the compounds involved, temperature and pressure conditions, and whether phase equilibria are important.

In addition to super-critical CO_2 as a working fluid, research on other non-conventional fluids and their simulations has gained attention. As a result, there is a growing need for accurate modeling and simulation tools that can handle the complexities of non-ideal gases. These tools enable researchers and engineers to investigate and improve the performance of a wide range of industrial processes involving compressible flow analysis, such as the design of power cycles, heat exchangers, and chemical reactors.

Early researchers investigated the thermodynamics and transport properties of dense gases, as well as gas dynamic behavior near the critical point. In 1942, Bethe [22] utilized the Van der Waals gas model to demonstrate that there was a specific region in the pressure-specific volume plane where the isentropes exhibited negative curvature. This observation revealed that when a dense gas is in this region, it behaves significantly differently from what classical analysis predicted. The conventional perfect gas theory suggested that only compression shock waves could occur to satisfy the Second Law of Thermodynamics. However, Bethe[22], Duhem[23], Weyl[24], Courant and Friedrichs[25], and other researchers proposed the possibility that rarefaction shocks might occur in single-phase vapors. Bethe indicated that an expansion shock was possible only when the normalized specific heat at constant volume c_v/R is greater than 17.5, which he considered impossible for a real fluid. Later, Zel'dovich[26] explored the possibility of such fluids and reached the same conclusion. Subsequently, Landau and Lifshitz [27] described the basic gas behavior with a non-dimensional form of $(\partial^2 v/\partial p^2)_s$ and defined it as the fundamental derivative Γ.

In 1971, Thompson[14] determined that the sign of this non-dimensional thermodynamic quantity could determine the possibility of forming rarefaction shocks in an arbitrary fluid. Thompson pointed out that the existence of rarefaction shocks requires a negative fundamental derivative and other conditions to be satisfied. These significant findings promoted the development of dense gas dynamics. Thompson and Lambrakis[28] also provided theoretical evidence for the existence of such fluids and listed several candidate fluids, such as $C_{11}F_{22}$. These candidate fluids have finite negative fundamental derivative regions in the vicinity of the critical point and the liquid-vapor saturated line due to molecular complexity and inter-molecular forces[15]. To distinguish them from classical gases of low molecular complexity, a particular class of dense gas called the Bethe-Zel'dovich-Thompson (BZT) gas was named. BZT fluids have embedded regions of negative fundamental derivative near the critical point. Cramer and Tarkenton[29] investigated some steady transonic flow behaviors of these fluids. More recently, Colonna et al.[30] presented additional BZT fluids, including siloxanes, a working fluid currently used in organic Rankine cycle engines. These works support the existence of BZT fluids and lay the groundwork for further research to comprehend the nonclassical gas behavior of BZT fluids.

Dense gas effects were taken into consideration in nozzle flow analyses dating back to the early twentieth century. Callendar's work in 1901[31] marked the beginning of a series of investigations on dense gas effects in nozzle flow. Since then, there has been a significant amount of research conducted on non-ideal gas flow and its practical applications. One of the earliest attempts to develop a comprehensive understanding of non-ideal gas flow was undertaken by Sullivan in 1981[32]. In his review, Sullivan compared five isentropic equations, the polytrope, Walker, Van der Waals, Rayleigh, and Callendar models, and discussed their historical development and limitations. The work of Arp et al.[33] attempted to determine the occurrence of the Gruneisen parameter, which relates thermodynamic properties to lattice vibrational spectra and has long been used in equations of state for solids[34]. Leung and Epstein[35] focused on one-dimensional isentropic flow and developed a generalized critical flow model for the non-ideal gas flow. By adopting the Redlich-Kwong (R-K) equation of state, their computation results for various common gases were compared with Johnson's work[36] as well as the experimental data. Similarly, Bober and Chow[37] conducted numerical computations on the convergent-divergent nozzle and obtained a method for one-dimensional non-ideal gas flow by applying the R-K equation of state. They utilized methane gas as the working fluid and presented plots of pressure, temperature, and area ratios as functions of Mach number. More recently, Sirignano[38][39] discussed the modifications necessary for compressible flow at high pressures due to the effects of real gases.

He analyzed normal compressive shock waves with supercritical upstream thermodynamic conditions using the SRK model and presented calculation results for common gases such as argon, nitrogen, and carbon dioxide. These studies have contributed significantly to the understanding of nozzle flow, with a particular emphasis on non-ideal-gas flow and the various models used to describe it. While the early studies by Callendar were focused on dense gas effects, the recent research has extended to more general non-ideal gas flows and has produced models and equations that are better suited for practical applications. The ongoing research in this field promises to yield further insights and innovations in the design and operation of nozzle systems.

In addition to the behaviors of single-component fluids, the study of the non-conventional gas behaviors of multi-component fluids has been a topic of interest for researchers due to its numerous real-world applications. Unlike mixtures of ideal gases, molecular interactions between different molecules play a critical role in the thermodynamic properties of dense vapors of multi-component mixtures. As a result, the behavior of these mixtures is far from being a simple linear function of the mole fractions of each compound, posing a considerable challenge to the study of such systems. To better understand the non-conventional gas behaviors of multi-component fluids, various researchers have proposed novel approaches to tackle this complex problem. Colonna and Silva [40] introduced a procedure to evaluate the equation of state for highly non-ideal mixtures and the fundamental derivative for Siloxanes. Meanwhile, Angelino and Invernizzi [41] conducted experimental studies on the thermal stability of siloxane mixtures. Guardone et al. [42] presented a review on the nonclassical gas dynamics of mixtures and demonstrated numerical simulations of a supersonic expansion using mixtures of siloxanes and perfluorocarbons. Their findings indicated that mixing compounds of the same fluid family did not enhance nonclassical gas dynamic phenomena for the considered mixtures.

However, previous studies have focused primarily on the real-gas effect and provided results for common gases. While some cases were for gases near their critical region, they did not fall into the negative fundamental derivative region. In contrast, the present work aims to contribute to the advancement of knowledge in this field by focusing on a family of organosilicon compounds as the working fluid. This decision was based on the relatively large region of negative fundamental derivatives associated with this family of compounds. Moreover, the fundamental derivative is considered a local thermodynamic variable rather than a constant throughout the flow. The present work provides a complete set of theories for the nonclassical behavior of BZT gases, including the general relation of the fundamental derivative to other thermodynamic variables. This approach offers a comprehensive understanding of the non-conventional gas behaviors of multi-component fluids and contributes to the development of accurate models for such systems. The present study is limited to theoretical and computational analyses. There is a need for experimental validation of the proposed theories and the development of more accurate equations of state for highly non-ideal mixtures. It is hoped that such efforts may lead to improved designs for various industrial processes, such as the production of specialty chemicals and the development of more efficient energy systems.

1.3 Experimental and Numerical Simulation Verification of Nonclassical Phenomena

The development of experimental facilities has been necessitated to understand the nonclassical gas behavior in the dense-gas region and to validate the existence of rarefaction shock waves. In this regard, a number of studies have been conducted to explore the nonclassical gas dynamics and to demonstrate the existence of rarefaction shock waves.

Borisov et al.[43] conducted one of the earliest experiments on rarefaction shock waves using Freon-13 as the working fluid near the gas critical liquid-vapor point. The researchers attempted to confirm that rarefaction shock waves are unique phenomena that can only occur in the gas critical region. To validate their hypothesis, experiments using Freon-13 far away from the critical point and experiments using nitrogen were also conducted to provide a comparison. The experiments showed an abnormal decrease in the speed of sound near the critical point with the increasing pressure, which was taken as evidence of the existence of rarefaction shock waves. Later, Kutateladze, Nakoryakov, and Borisov [44] qualitatively compared the experimental data with calculated results and attributed this nonclassical phenomenon to the abnormal adiabats in the critical region. However, the validity of the rarefaction shock wave observed in these experiments was later questioned by other researchers who suspected that the observed wave was caused by anomalous behavior of the test gas at or very near the critical point, rather than a true expansion shock [45, 46].

To further investigate rarefaction shock waves, Fergason [47] designed a dense gas shock tube with a single copper diaphragm to initiate each experimental trial. The experiment aimed to generate a nonclassical rarefaction shock in fluid PP10, but no rarefaction wave was captured. The results of the study showed that the diaphragm opening time significantly affected the experiments. In 1989, Cramer [48] showed the possibilities of the shock splitting, the sonic shock, and the double sonic shock [49]. Briefly, sonic shocks are shocks that have a speed identically equal to the convected sound speed immediately before or after the shock wave. Double sonic shocks are shocks that have sonic conditions on both sides of the shock. The split shock is two sonic shocks separated by a compression fan. To further advance research on shock-splitting and double sonic shock, Cramer [45] applied the Martin-Hou equation to calculate the fundamental derivatives of candidate BZT fluids and showed seven of the commercially available fluids which have relatively larger critical regions. Moreover, Thompson, Carofano, and Kim [50] observed nonclassical phenomena in a two-phase vapor, including the liquefaction shock, mixture-evaporation shock, and condensation waves, along with numerical simulation results in both single-phase and two-phase flows. Furthermore, Gulen, Thompson, and Cho [51] conducted shock-tube experiments to obtain near-critical states and determine corresponding thermodynamic properties, including Γ, to investigate the possibility of rarefaction shocks.

The study of nonclassical gas behavior in two-phase flow conducted by Thompson et al. [50] sparked interest in further investigating this phenomenon. To that end, Fergason, Ho, Argrow, and Emanuel [52] performed a shock tube study at the University of Colorado, Boulder, to produce rarefaction shock waves in single-phase flow. The study aimed to investigate the properties of nonclassical gas behavior under specific conditions. To achieve their goals, the researchers developed a global method that utilized the Van der Waals model to determine the initial conditions needed to produce the desired rarefaction shock wave field. The method allowed for the production of rarefaction shock waves with predetermined shock strengths, an essential aspect of studying the behavior of these waves. Furthermore, Fergason and Argrow [53] numerically investigated the effect of boundary-layer formation on rarefaction shock wave propagation. Their findings indicated that the boundary-layer effect has relatively less impact on nonclassical flow fields. This insight was indispensable in understanding the behavior of rarefaction shock waves and their propagation in single-phase flow. To construct the shock tube, Fergason and Argrow [54] developed a novel apparatus that could produce nonclassical phenomena in a single-phase flow. The researchers tested the shock tube using nitrogen as the testing fluid, comparing the results with those of the ideal Riemann problem. The findings of this investigation revealed the possibility of observing rarefaction shock waves in single-phase flow experimentally. However, the practical operation of the shock tube presents some challenges. Suitable initial conditions and proper experimental setup are necessary to produce the desired rarefaction-shock-wave field accurately. Additionally, some of the thermodynamic properties lack accurate data, making it challenging to precisely observe the shock waves. Furthermore, rarefaction shock waves constructed near the critical point are typically much weaker than those in regular cases, which increases the difficulties associated with manufacturing the diaphragm and observing the shock waves.

Figure 1.1: Picture of FAST [1].

At TU Delft, researchers have conducted experimental investigations on dense gases, focusing on the wave velocity of dense vapor. To achieve this, they developed the Flexible Asymmetric Shock Tube (FAST), a Ludwieg tube[55] that can generate shocks with Mach numbers up to 8 [56]. The FAST has been a valuable tool for studying non-ideal gas behavior under high-pressure and high-temperature conditions, particularly in dense gases. Measurements were conducted at the Politecnico di Milano's compressible fluid dynamics for renewable energy applications laboratory (CREA) using the Test Rig for Organic Vapors (TROVA). The TROVA is a blow-down wind tunnel that was designed explicitly for non-ideal compressible fluid studies, particularly for detecting nonclassical effects of expanding flows [57]. Spinelli obtained preliminary results for the linear siloxane fluid MDM in the non-ideal thermodynamic zone, where the fluid was subject to high-pressure and high-temperature conditions [58][59]. Although nonclassical effects have not been observed in the TROVA experiments, the results have been promising, and researchers have identified areas for future research. In particular, the TROVA has demonstrated its potential as a tool for investigating non-ideal gas behavior in dense gases under high-pressure and high-temperature conditions. Furthermore, the FAST has proved to be a useful experimental apparatus for generating and observing shock waves in dense gases. The combination of the TROVA and the FAST has the potential to provide further insights into the properties and behavior of dense gases, which could have significant implications for various industrial applications. However, further research is needed to explore the full potential of these experimental tools, particularly in observing nonclassical effects in dense gases.

Nonclassical phenomena in single-phase flow are difficult to observe experimentally, but they have been the subject of several numerical studies based on solving the Euler equations. One such study was conducted by Argrow [60], who introduced a TVD predictor-corrector (TVD-MacCormack) scheme to solve the one-dimensional Euler equations for Van der Waals gas. Reflective boundary conditions were applied in the study, and it was found that the reflections observed at the shock tube end walls for a dense gas are much more complex than those observed for regular gases. However, the Van der Waals model has some shortcomings, and the evaluation of more refined state equations is necessary to cover them.

Aldo and Argrow [61] [62] developed a method of characteristics (MOC) for two-dimensional (planar) and axisymmetric flow of a Van der Waals gas and applied it in the design of minimum length nozzles (MLN). Since the MLN procedure is limited to cases where there is only one sonic point in the nozzle, they speculated that the design to employ two centered expansions separated by a finite converging wall may be able to accomplish the expansion in a minimum length. Following Argrow's studies, Brown and Argrow [63] [64] [65] extended the TVDM method to the computation of two-dimensional nonclassical flows under the Martin–Hou equation of state. Discussions on the wavefield structures and thermodynamic states for a dense gas flow were presented. Fergason and Argrow [53] then extended its application also to the simulations of two-dimensional viscous flow for nonclassical gases by solving the two-dimensional planar Navier-Stokes equations. Displacement thicknesses were quantified and analyzed. Furthermore, Guardone, Selmin, and Vigevano [66], and Guardone and Vigevano [67] extended the widely used Roe linearization method for the ideal gas to the polytropic Van der Waals gas. These studies have contributed significantly to our understanding of nonclassical phenomena in single-phase flow. Although it is challenging to experimentally observe these phenomena, the numerical studies presented in the literature provide insight into the complex behavior of dense gases, highlighting the need for more sophisticated models and methods to represent such flows accurately. The use of TVD and MOC schemes in the numerical simulations of nonclassical flows has opened up opportunities for further exploration into the design of novel propulsion systems and the optimization of existing ones.

Moreover, to gain a better understanding of the transonic flow of BZT fluids over thin airfoils or turbine blades, researchers have made significant efforts to modify existing equations and develop new numerical methods. One such effort was made by Cramer and Tarkenton [29] who presented a modified form of the classical transonic small-disturbance equations and compared it with the classical theory to investigate the transonic flow of BZT fluids. Later, Monaco, Cramer, and Watson [68] presented a numerical example of two-dimensional isentropic supersonic cascade flow, where they utilized the explicit predictor-corrector method of MacCormack to analyze BZT fluids and compared the results with those of lighter fluids. However, numerical simulations for dense gas flows pose significant challenges as the cases are more complex due to the existence of mixed waves, unlike the standard numerical schemes for solving classical compressible Euler equations. As a result, researchers have proposed various numerical methods to address these challenges. For instance, Cinnella and Congedo [69] proposed a high-order centered numerical method that can generate lower entropy errors at the leading edges of airfoils and blades. However, the accuracy of this method close to the flow discontinuities is slightly lower than the well-known second-order upwind scheme. Moreover, it is crucial to note that the standard pressure-based sensor may fail to detect the expansion shock or isentropic compression fan in dense gas flows, thus requiring the development of new and improved sensors to accurately detect these phenomena.

1.4 The Role of Dense Gas Dynamics in Organic Rankine Cycle Engines

The organic Rankine cycle (ORC) has emerged as a viable alternative to the conventional Rankine cycle, particularly in cases where the high temperature required to produce steam cannot be achieved. This cycle has a rich history that dates back to the early 19th century[70], around a century after the invention of the steam engine. At that time, the pressure limitations of boilers made it difficult to achieve high temperatures and led researchers to explore liquids that could be vaporized at lower temperatures. The concept of using high molecular mass fluids to reduce turbine RPM and the number of turbine stages was first proposed by Luigi D'Amelio in 1935 [71]. Since then, a wide range of organic fluids and mixtures have been identified, proposed, and employed in Rankine engines. Early examples of such fluids include pentane, butane, and ethers, while more recent examples include refrigerants, silicone oils, and other specialty fluids[72–96].

Compared with the multistage steam turbine systems of the Rankine cycle engines or other small engines that are mechanically more complex, a typical organic Rankine cycle engine usually requires only a single-stage turbine. Some recent developments on the organic Rankine cycle systems have focused on using renewable energy resources, including solar energy [91, 97] and waste heat streams resulting from industrial processes [98, 99]. Researchers also have attempted to investigate the BZT gas dynamic behaviors in the organic Rankine cycle engine. As discussed above, BZT fluids have shown many unconventional phenomena near the liquid-vapor critical point. The generation of shock waves is one of the major losses in the organic Rankine cycle engines. Applying the BZT fluids in the organic Rankine cycle engines may significantly reduce the shock-related losses (both the wave drag from shocks and losses from boundary-layer separation due to shock reflections) and enable the design of supersonic shock-free turbine cascades. Brown and Argrow [65] simulated the cascade flow using PP10 ($C_{13}H_{22}$), a proposed BZT fluid, as the working fluid and compared the simulation results with using Toluene (C_7H_8). All performance parameters for the PP10 cascade flow were enhanced. Wheeler and Ong [100] proposed a new method for the design of nozzles operating with dense gases and ran a two-dimensional simulation to determine the turbine performance. Results showed that the turbine efficiency is highly dependent on the choice of the working fluid.

1.5 Objectives of This Research

It is essential to understand the differences between the behavior of ideal and real gases, particularly in the context of nonclassical gas flow. To this end, a set of theories for nonclassical gas flow needs to be developed. Such theories would help to identify trends in gas dynamic behavior that are not observed in classical ideal-gas flow theory. One critical problem is to locate the region where the fluid exhibits a negative fundamental derivative. This region is of particular interest as it can be associated with the onset of rarefaction shocks and compression fans. Numerical simulation methods can be applied to analyze the flow behavior in the regions where the fluid exhibits a negative fundamental derivative, capturing unconventional gas dynamic behavior. However, the specific gas behavior analysis and the corresponding thermodynamic relations should be derived from basic conservation laws and the real-gas equation of state. Furthermore, the study of nonclassical gas flow is also important in the context of the ORC engine flow. This type of flow can exhibit a wide range of complex behaviors, including non-equilibrium and non-steady-state phenomena. In such scenarios, the use of models based on ideal-gas law can lead to significant errors in the prediction of flow behavior. The development of nonclassical gas flow theories and numerical simulation methods can help to improve the accuracy of the predictions. The identification of unconventional gas dynamic behavior through the development of theories and numerical simulation methods can improve the accuracy of predictions in scenarios where ideal-gas law based models are not applicable. The derivation of gas behavior analysis and corresponding thermodynamic relations from basic conservation laws and the real-gas equation of state is imperative for accurate gas flow modeling.

The objectives of this dissertation are as follows:

- Locate the region of the negative fundamental derivative.
- Develop a theoretical foundation and methodology for analyzing the nonclassical gas behaviors within this particular region.
- Analyze the thermodynamic properties of gases and select appropriate gas models.
- Understand the nonclassical gas behavior of the dense gas in one-dimensional flow and quasi-one-dimensional flow.
- Develop a fast, accurate, and robust computational method for calculating real-gas flows.
- Apply numerical simulation of real-gas solver under different scenarios and analyze its performance and effectiveness.
- Provide a better understanding of the behavior of dense gases in practical applications.

1.6 Outline of the Dissertation

The following outline constitutes the framework of this dissertation.

In Chapter 1, an in-depth introduction to the related topics is provided, presenting a comprehensive background on nonclassical gas dynamics. Experimental and numerical simulation verification of nonclassical phenomena, as well as the significance of dense gas dynamics in Organic Rankine Cycle engines, are discussed. Furthermore, this chapter delineates research objectives and offers a methodical outline of the research approach.

In Chapter 2, the fundamental properties of BZT gas and its behavior in quasi-one-dimensional (Q1D) flow are investigated. The major focuses are to identify the region characterized by a negative fundamental derivative, as well as explore the nonclassical gas dynamics occurring within this specific region. The association between the fundamental derivative and other thermodynamic variables is examined, leading to the derivation of the pertinent thermodynamic relations and flow equations within isentropic quasi-one-dimensional flows. This investigation delves into the expression of isentropic exponents, the stagnation properties, the Mach number - velocity relation, the Mach - number area ratio relation, etc. To effectively illustrate the nonclassical gas dynamics, the appropriate candidate for BZT fluids which will be subsequently utilized in simulations is determined. Moreover, test cases involving isentropic flows with different inlet conditions are presented to demonstrate these nonclassical behaviors.

In Chapter 3, following the completion of the one-dimensional analysis, a comprehensive examination of the nonclassical gas dynamics in non-isentropic flows and more intricate scenarios is undertaken. Particular emphasis is placed on the investigation of unconventional wave phenomena, specifically the formation of expansion shock waves and compression fans. Through the derivation and scrutiny of these phenomena, a deeper understanding is attained. Additionally, the conservation equations pertinent to normal shock waves, along with normal shock relations, are explored in detail. Sample cases involving normal shock for a BZT gas are presented, which serve to provide a profound comprehension of these phenomena within the context of nonclassical gas dynamics.

In Chapter 4, a sophisticated machine-learning algorithm, specifically an artificial neural network (ANN), is introduced for the purpose of predicting the thermodynamic properties of dense gases. A comprehensive description of the general structure, essential features, and training functions of the ANN is provided, elucidating the fundamental principles underlying its design and implementation. Furthermore, the procedure for generating the training data set is described in detail, alongside an evaluation of the accuracy and performance of various models. Following a thorough analysis and discussion of the simulation results, the comparison to analytical solutions is highlighted. This comprehensive examination not only demonstrates the efficacy of the ANN in predicting the thermodynamic properties of dense gases but also serves as a foundation for further research and optimization of the algorithm in relevant applications.

In Chapter 5, a numerical algorithm is presented to compute the transonic flow of dense gases exhibiting nonclassical BZT gas behavior in two dimensions. As previously noted, although a limited number of studies have provided simulation results for BZT gas flows, the majority employed standard flow solvers designed for regular gases. As the gas approaches its critical point, the computation time significantly increases, and the corresponding accuracy declines. To address this issue, a fast, accurate, and robust computational method for solving the Navier-Stokes equations specifically tailored to the transonic flow of BZT gases is developed. In this context, the numerical dissipation operator within an artificial viscosity method is reevaluated. A matrix dissipation method, which incorporates the dense gas effects, is proposed in this work to overcome the challenges associated with modeling BZT gas behaviors. Simulation results for shock tube and corner flow scenarios are meticulously discussed to validate the efficacy of the proposed numerical method, demonstrating its potential for advancing research on nonclassical gas dynamics in complex environments.

In Chapter 6, an innovative pressure-based solution method for compressible flow is proposed to address the challenges associated with conventional density-based solvers. Although pressure-based solvers are typically less suited for compressible flows with high Mach numbers, the development of a novel pressure-based solution method for compressible flow seeks to bridge this gap. The newly devised method offers a unified approach to solving a wide range of flow problems with a single solver. Background information on the method is provided, accompanied by a detailed explanation of the proposed pressure-based algorithm. Preliminary numerical results are presented, showcasing the algorithm's performance and illustrating its potential applicability to various flow problems.

In Chapter 7, a comprehensive summary of the research findings and their implications within the field of nonclassical gas dynamics is presented. Potential future research endeavors in nonclassical gas dynamics and their applications across various engineering domains are emphasized, showcasing the significance and impact of the study.

This scholarly investigation advances the field by integrating cutting-edge technologies and dense gas flow theories into computational fluid dynamics frameworks, facilitating the analysis and comprehension of nonclassical dense gas flow in compressors, turbines, and a wide array of engineering applications. By employing these state-of-the-art theoretical constructs, the study explores the complexities of nonclassical gas dynamics, elucidating their behavior under a diverse range of conditions. These outcomes contribute to a more sophisticated understanding of nonclassical gas dynamics and highlight their potential applications in the conception and development of energy-efficient systems. The findings presented in this dissertation not only augment the existing body of knowledge on non-ideal dense gas flow but also establish a robust foundation for further exploration and optimization of advanced engineering applications. As a result, this work plays an instrumental role in shaping the future trajectory of research and innovation within the domains of dense gas dynamics and energy-efficient system design.

Chapter 2

The BZT Gas and its Fundamental Gas Dynamics Behavior in Quasi-one-dimensional Flow

2.1 The Fundamental Derivative of Gases

2.1.1 Definition of the Fundamental Derivative

The definition of the fundamental derivatives and why it is so important in dense gas dynamics were discussed by Landau and Lifshitz[27] and Thompson[14]. From their theory, the non-dimensional form of Γ is given as

$$\Gamma = \frac{c^4}{2v^3}\left(\frac{\partial^2 v}{\partial p^2}\right)_s \tag{2.1}$$

where c is the speed of sound, v is specific volume, p is pressure and the subscript s means the derivative is taken at constant entropy s.

2.1.2 Other Expressions for the Fundamental Derivative

From the definition above, the sign of Γ is related to the term $\left(\frac{\partial^2 v}{\partial p^2}\right)_s$ directly. No matter which gas model is used for analysis, the behavior of gas is associated with the curvature of the isentrope in the $p - v$ plane, measured by $\left(\frac{\partial^2 v}{\partial p^2}\right)_s$. For a better understanding of the relationship between Γ and the unconventional dense gas behavior, the first step is to rearrange the equation and to express Γ in terms of other thermodynamic variables.

For general equations of state, the speed of sound c is given by

$$c^2 = \left(\frac{\partial p}{\partial \rho}\right)_s = -v^2 \left(\frac{\partial p}{\partial v}\right)_s \geq 0 \tag{2.2}$$

Notice

$$\left(\frac{\partial v}{\partial p}\right)_s = \frac{1}{\left(\frac{\partial p}{\partial v}\right)_s} \tag{2.3}$$

Thus

$$\left(\frac{\partial^2 v}{\partial p^2}\right)_s = \frac{\partial}{\partial p}\left[\frac{1}{\left(\frac{\partial p}{\partial v}\right)_s}\right]_s = \frac{\partial}{\partial v}\left[\frac{1}{\left(\frac{\partial p}{\partial v}\right)_s}\right]_s \frac{1}{\left(\frac{\partial p}{\partial v}\right)_s} = -\frac{\left(\frac{\partial^2 p}{\partial v^2}\right)_s}{\left(\frac{\partial p}{\partial v}\right)_s^3} \tag{2.4}$$

Substituting above into Equation (2.1) and making use of Equation (2.2), we obtain

$$\Gamma = \frac{v^3}{2c^2}\left(\frac{\partial^2 p}{\partial v^2}\right)_s \tag{2.5}$$

Equation (2.5) is used more generally than the original definition due to the common form of the polynomial equation of state. Typically pressure is given as a function of other thermodynamic variables and thus it would be easier to derive the expression of $\left(\frac{\partial^2 p}{\partial v^2}\right)_s$

than the expression of $\left(\frac{\partial^2 v}{\partial p^2}\right)_s$. Equation (2.5) states that Γ is related to the curvature of the isentrope. Under most conditions, the isentrope is a concave curve in the $p - v$ diagram as shown on the left of figure 2.1. So conventionally Γ is supposed to be positive. For a dense gas, there can be a region near the saturation line where Γ turns negative as shown on the right of figure 2.1.

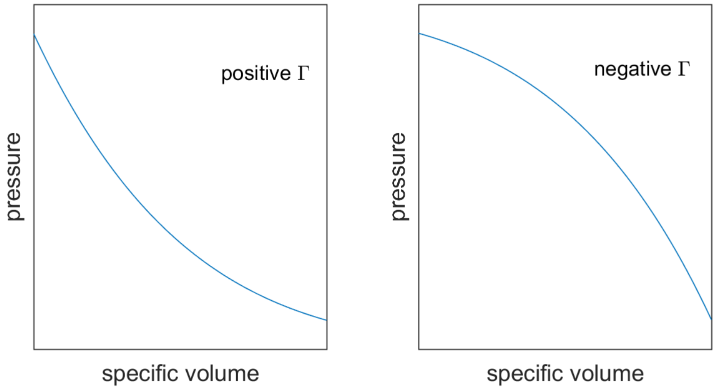

Figure 2.1: Sign of the fundamental derivative

Besides the sign of Γ, another variable to be concerned about is the speed of sound, which is tightly coupled with Γ. The second-order partial derivative in Equation (2.5) can be expressed in terms of density and the speed of sound

$$\left(\frac{\partial^2 p}{\partial v^2}\right)_s = \left(\frac{\partial}{\partial v}\left(\frac{\partial p}{\partial v}\right)_s\right)_s = \left(\frac{\partial}{\partial v}\left(-\frac{c^2}{v^2}\right)\right)_s = \frac{1}{v^2}\left(\frac{\partial(\rho c)^2}{\partial \rho}\right)_s = \frac{2c}{v^3}\left(\frac{\partial(\rho c)}{\partial \rho}\right)_s \tag{2.6}$$

which shows directly the relationship between the sound of speed and Γ

$$\Gamma = \frac{1}{c}\left(\frac{\partial \rho c}{\partial \rho}\right)_s = 1 + \frac{\rho}{c}\left(\frac{\partial c}{\partial \rho}\right)_s = 1 - \frac{v}{c}\left(\frac{\partial c}{\partial v}\right)_s \tag{2.7}$$

Consider an expansion process. When the gas is within $\Gamma < 1$ region (nonclassical gas), Equation (2.7) states that the speed of sound increases as density decreases, under isentropic conditions.

In addition to density variations, a compression or expansion process is usually reflected by pressure change. Note

$$\left(\frac{\partial \rho c}{\partial \rho}\right)_s = c + \rho\left(\frac{\partial c}{\partial \rho}\right)_s = c + \frac{1}{v}\left(\frac{\partial c}{\partial p}\right)_s\left(\frac{\partial p}{\partial \rho}\right)_s = c + \frac{c^2}{v}\left(\frac{\partial c}{\partial p}\right)_s \tag{2.8}$$

Substituting it back into Equation (2.7), we obtain

$$\Gamma = 1 + \frac{c}{v}\left(\frac{\partial c}{\partial p}\right)_s \tag{2.9}$$

Equations (2.1), (2.5), (2.7), (2.9) are four different but equivalent expressions for the fundamental derivative Γ in terms of different thermodynamic properties, each of which shows a significant physical insight into the meaning of Γ. There are two demarcation lines that are important in this analysis. For a perfect gas whose isentropic process can be expressed as $pv^\gamma = const$, it is easy to show $\Gamma = \dfrac{1+\gamma}{2} > 1$, which is the case with a conventional gas under normal conditions. When $\Gamma > 1$, the speed of sound increases with pressure increase, and the gas behavior is in qualitative agreement with the classical theory for a perfect gas. When Γ reaches 1, Equation (2.9) shows that the speed of sound remains as a constant in an isentropic process while pressure is increasing or decreasing, and pressure is a linear function of density only. When Γ is smaller than 1, the speed of sound turns to decrease with increasing pressure. Accompanying the change of the speed of sound, the gas starts to show some unconventional qualitative behavior. If Γ decreases below 0, Equation (2.5) shows that isentropes in this region have negative curvature and the gas dynamic behaviors are totally different or even opposite to those based on the classical theory. These unconventional behaviors will be discussed in later sections.

Table 2.1: Gas behavior related to the sign and value of the fundamental derivative Γ

$\Gamma > 1$	$\left(\frac{\partial c}{\partial v}\right)_s < 0$	classical near ideal-gas behavior
$0 < \Gamma \leqslant 1$	$0 < \left(\frac{\partial c}{\partial v}\right)_s < \frac{c}{v}$	classical real-gas behavior
$\Gamma \leqslant 0$	$\left(\frac{\partial c}{\partial v}\right)_s > \frac{c}{v}$	nonclassical behavior

2.1.3 Calculation of the Fundamental Derivative from the Equation of State

The four different expressions of the fundamental derivative Γ are listed below.

$$\Gamma = \frac{c^4}{2v^3}\left(\frac{\partial^2 v}{\partial p^2}\right)_s$$
$$\Gamma = \frac{v^3}{2c^2}\left(\frac{\partial^2 p}{\partial v^2}\right)_s$$
$$\Gamma = \frac{1}{c}\left(\frac{\partial \rho c}{\partial \rho}\right)_s = 1 - \frac{v}{c}\left(\frac{\partial c}{\partial v}\right)_s$$
$$\Gamma = 1 + \frac{c}{v}\left(\frac{\partial c}{\partial p}\right)_s$$

All of them are expressed in terms of derivative along an isentrope. By applying thermodynamic equations and Maxwell relation (see Appendix A.2), Bethe[101] gave an alternative expression for Γ by using v and T as the independent thermodynamic state variables (see Appendix A.3)

$$\Gamma(T,v) = \frac{v^3}{2c^2}\left[\frac{\partial^2 p}{\partial v^2} - \frac{3T}{c_v}\frac{\partial p}{\partial T}\frac{\partial^2 p}{\partial T \partial v} + \left(\frac{T}{c_v}\frac{\partial p}{\partial T}\right)^2\left[\frac{3}{T}\frac{\partial c_v}{\partial v} + \frac{1}{T}\frac{\partial p}{\partial T}\left(1 - \frac{T}{c_v}\frac{\partial c_v}{\partial T}\right)\right]\right] \tag{2.10}$$

where $p = p(T,v), c_v(T,v) = \dfrac{\partial e(T,v)}{\partial T}$.

Equation (2.10) provides a convenient way to calculate the value of Γ by using the equation of state directly. For example, if substituting the ideal-gas law and assuming constant specific heats, the equation of Γ can be simplified as

$$\Gamma = \frac{1}{2}\left(\frac{c_p}{c_v} + 1\right) = \frac{\gamma + 1}{2} \tag{2.11}$$

which gives the value of Γ for a perfect gas.

2.1.4 Van der Waals Gas Relations

Equation (2.10) has shown the method to calculate the value of the fundamental derivative from the equation of state. Real-gas equations of state like the Van der Waals equation or Soave-Redlich-Kwong equation are commonly used. The present work has selected Van der Waals equation of state for computation, as it was the first, simplest, and best-known equation of state to account for the real-gas effects. To be more specific, it accounts for intermolecular attraction and the volume that a real-gas molecule takes up. Due to the statistical nature of thermodynamic properties, the Van der Waals equation served as the earliest connection between the macroscopic behavior of the fluid and the microscopic interaction of molecules.

Table 2.2 lists the Van der Waals EoS and relevant resulting first-order and second-order derivatives from the Van der Waals gas model. These expressions are mathematically simple, but they nevertheless adequately predict and explain the non-conventional gas behavior near the critical point.

Table 2.2: Relations from Van der Waals gas model

Flow Variable	Calculation Formula
Equation of State	$p = \frac{\rho R T}{1 - b\rho} - a\rho^2$
$\left(\frac{\partial p}{\partial T}\right)_v$	$\frac{R\rho}{1 - b\rho}$
$\left(\frac{\partial^2 p}{\partial T^2}\right)_v$	0
$\left(\frac{\partial p}{\partial \rho}\right)_T$	$\frac{RT}{(1 - b\rho)^2} - 2a\rho$
$\left(\frac{\partial p}{\partial v}\right)_T$	$-\frac{RT}{(v-b)^2} + \frac{2a}{v^3}$
$\left(\frac{\partial^2 p}{\partial v^2}\right)_T$	$\frac{2RT}{(v-b)^3} - \frac{6a}{v^4}$
$\left(\frac{\partial^2 p}{\partial T \partial v}\right)_T$	$-\frac{RT}{(v-b)^2}$
$\left(\frac{\partial v}{\partial T}\right)_p$	$-\frac{\left(\frac{\partial p}{\partial T}\right)_v}{\left(\frac{\partial p}{\partial v}\right)_T}$
Specific Heat	$c_p = c_v\left(1 - \frac{T}{c_v}\frac{R^2}{2a\rho(1-b\rho)^2 - RT}\right)$
Speed of Sound	$c = \sqrt{v^2(\frac{RT}{(v-b)^2} - \frac{2a}{v^3} + \frac{T}{c_v}\frac{R}{(v-b)^2})}$
Enthalpy	$h = c_v T - \frac{a}{v} + pv$

The coefficient a in the Van der Waals EoS represents the strength of the intermolecular attractive forces in the fluid. The coefficient b represents the volume occupied by the molecules themselves, considering that real molecules are not point-like but have a finite size.

In a two-phase flow, these attractive forces can lead to phase change, such as vaporization or condensation. Meanwhile, the change in phase can considerably alter the effective volume of the system. Thus, the Van der Waals EoS and its related derivatives, as shown in Table 2.2, in combination with Maxwell's equal area rule, is used to predict phase transitions such as the boiling curves[102] and vapor-liquid equilibrium calculation[103], etc. Furthermore, we may rewrite the Van der Waals EoS in polynomial form

$$Z^3 - (1 + B)Z^2 + AZ - AB = 0 \tag{2.12}$$

where

$$Z = \frac{pv}{RT}, \qquad A = \frac{pa}{(RT)^2}, \qquad B = \frac{pb}{RT}$$

Here the coefficients A and B are non-dimensional parameters related to intermolecular attraction and repulsion, respectively. For a perfect gas, $A = B = 0$. The value of these coefficients can reflect how far a real gas deviates from the ideal-gas behavior.

These equations can also be extended to encompass both Soave-Redlich-Kwong (SRK) and Peng-Robinson (PR) fluid models. The outputs derived from SRK or PR approaches, while quantitatively distinct, maintain a qualitative resemblance to those generated via the Van der Waals Equation of State. However, in scenarios where the constants 'a' and 'b' are variables depending on pressure and temperature, the derived equations, as presented in Table 2.2, will exhibit substantial divergence. These modified forms will not only extend in length but also increase in complexity, presenting a more intricate mathematical landscape.

2.1.5 Specific Heat Function and Enthalpy

For an ideal gas, the specific heat capacities can be elegantly related to the universal gas constant

$$c_p - c_v = R$$

They can also be expressed as a function of the ratio of specific heats $\gamma \equiv c_p/c_v$ and the universal gas constant

$$c_p = \frac{\gamma R}{\gamma - 1} \quad \text{and} \quad c_v = \frac{R}{\gamma - 1}$$

Enthalpy is defined as a state function that in general depends on both pressure and temperature. For a thermally perfect gas, enthalpy is a function of temperature only, i.e.

$$h = h(T) \quad , \quad dh = c_p(T)dT$$

For the more restrictive case of a calorically perfect gas, the heat capacity is constant, i.e., $h = c_pT$.

The relation between the specific heat capacities for a real gas is given as (see Appendix A.4)

$$c_p - c_v = T\left(\frac{\partial v}{\partial T}\right)_p \left(\frac{\partial p}{\partial T}\right)_v \tag{2.13}$$

And the differential form of enthalpy change can be written as

$$dh = \left(\frac{\partial h}{\partial T}\right)_p dT + \left(\frac{\partial h}{\partial p}\right)_T dp \tag{2.14}$$

Equation 2.14 and its subsequent derivations hold true for all general real gas models, encompassing beyond just the Van der Waals Equation of State. Recall the enthalpy equation derived from the Gibbs relation

$$dh = vdp + Tds \tag{2.15}$$

Divide by dp on both sides of Equation (2.15)

$$\left(\frac{\partial h}{\partial p}\right)_T = v + T\left(\frac{\partial s}{\partial p}\right)_T \tag{2.16}$$

The second term on RHS can be rewritten by using the Maxwell relation

$$\left(\frac{\partial s}{\partial p}\right)_T = -\left(\frac{\partial v}{\partial T}\right)_p \tag{2.17}$$

Then Equation (2.16) becomes

$$\left(\frac{\partial h}{\partial p}\right)_T = v - T\left(\frac{\partial v}{\partial T}\right)_p \tag{2.18}$$

Substitute Equation (2.18) into Equation (2.14), the general form for calculating the enthalpy of a non-ideal gas is given as

$$dh = c_p dT + \left[v - T\left(\frac{\partial v}{\partial T}\right)_p\right] dp \tag{2.19}$$

Different gas models and equations of state can be applied to this equation. For the Van der Waals equation of state

$$p = \frac{RT}{v-b} - \frac{a}{v^2} \tag{2.20}$$

Take partial derivative of Equation (2.20)

$$\left(\frac{\partial T}{\partial p}\right)_v = \frac{v-b}{R} \tag{2.21}$$

$$\left(\frac{\partial p}{\partial v}\right)_T = \frac{-RT}{(v-b)^2} + \frac{2a}{v^3} \tag{2.22}$$

Recall the triple product rule of partial derivative (see Appendix A.1)

$$\left(\frac{\partial v}{\partial T}\right)_p \left(\frac{\partial T}{\partial p}\right)_v \left(\frac{\partial p}{\partial v}\right)_T = -1 \tag{2.23}$$

$\left(\frac{\partial v}{\partial T}\right)_p$ then can be expressed as

$$\left(\frac{\partial v}{\partial T}\right)_p = \frac{v^3(v-b)}{RTv^3 - 2a(v-b)^2} \tag{2.24}$$

Substituting Equation (2.24) into Equation (2.19), the differential form of enthalpy equation for Van der Waals gas is

$$dh = c_p dT + \left[v - \frac{Tv^3(v-b)}{RTv^3 - 2a(v-b)^2}\right] dp \tag{2.25}$$

Furthermore, let us expand upon this concept to encompass both the Soave-Redlich-Kwong (SRK) and Peng-Robinson (PR) fluid models which are also two widely used models in real gas analysis.

The SRK equation is an improvement over the simpler Redlich-Kwong equation. It introduces a correction factor to account for non-ideal behavior in real gases and liquids. This correction factor considers the attractive forces between molecules, resulting in a more accurate prediction of fluid properties. The SRK equation of state is given as follows:

$$p = \frac{RT}{v-b} - \frac{a\alpha(T)}{v(v+b)} \tag{2.26}$$

where a and b are substance-specific parameters, and $\alpha(T)$ is the temperature dependent function.

The function $\alpha(T)$ is given by:

$$\alpha(T) = \left[1 + (0.48508 + 1.55171\omega - 0.15613\omega^2)(1 - \sqrt{\frac{T}{T_c}})\right]^2$$

where ω is the acentric factor.

Take partial derivative of Equation (2.26)

$$\left(\frac{\partial p}{\partial T}\right)_v = \frac{R}{v-b} + \frac{aS}{v(v+b)\sqrt{TT_c}}(1 + S(1 - \sqrt{\frac{T}{T_c}})) \tag{2.27}$$

$$\left(\frac{\partial p}{\partial v}\right)_T = \frac{-RT}{(v-b)^2} + \frac{a\alpha(T)(b+2v)}{v^2(v+b)^2} \tag{2.28}$$

where $S = (0.48508 + 1.55171\omega - 0.15613\omega^2)$.

On the other hand, the PR equation incorporates both attractive and repulsive forces between molecules, making it more suitable for a wider range of fluids. This equation includes additional parameters that allow for a better representation of critical and near-critical behavior, as well as the prediction of vapor-liquid equilibrium. The PR equation of state is given as follows:

$$p = \frac{RT}{v-b} - \frac{a\alpha(T)}{(v^2 + 2bv - b^2)} \tag{2.29}$$

where a and b are substance-specific parameters, and $\alpha(T)$ is the temperature dependent function.

The function $\alpha(T)$ is given by:

$$\alpha(T) = \left[1 + (0.37464 + 1.54226\omega - 0.26992\omega^2)(1 - \sqrt{\frac{T}{T_c}})\right]^2$$

where ω is the acentric factor.

Take partial derivative of Equation (2.29)

$$\left(\frac{\partial p}{\partial T}\right)_v = \frac{R}{v-b} + \frac{aS}{(v^2+2bv-b^2)\sqrt{TT_c}}(1 + S(1 - \sqrt{\frac{T}{T_c}})) \tag{2.30}$$

$$\left(\frac{\partial p}{\partial v}\right)_T = \frac{-RT}{(v-b)^2} + \frac{2a\alpha(T)(b+v)}{(-b^2+2bv+v^2)^2} \tag{2.31}$$

where $S = (0.37464 + 1.54226\omega - 0.26992\omega^2)$.

In a manner congruent with the preceding methodology, Equations 2.27-2.28 and 2.30-2.31 are incorporated into Equation 2.23 to determine $\left(\frac{\partial v}{\partial T}\right)_p$. Subsequently, the derived variable is integrated into Equation 2.19. Utilizing this approach facilitates the derivation of the differential forms of the enthalpy equation for both the Soave-Redlich-Kwong (SRK) and Peng-Robinson (PR) models.

2.1.6 Thermodynamic properties of MDM

Regular gases usually do not have a negative fundamental derivative region because negative Γ requires gases of high molecular complexity. Earlier researchers had doubts about the existence of the so-called BZT gas and the related nonclassical gas behavior. Examples of BZT fluids have been identified for certain heavy hydrocarbons and some methylsiloxanes[104]. Some behaviors of BZT fluids have been studied extensively in recent years[105], focusing on the sonic shock and double-sonic shock. However, so far there is not yet a complete set of theory to describe how each flow variable changes along the isentrope.

In the present work, a compound gas named Octamethyltrisiloxane (also called MDM) is chosen as the working fluid. It is an organosilicon compound with the formula $C_8H_{24}O_2Si_3$. Organometallics are useful reagents, catalysts, and precursor materials with applications in thin film deposition, industrial chemistry, pharmaceuticals, LED manufacturing, and others. Figure 2.2 shows its chemical structure. Some basic properties of Octamethyltrisiloxane are given in Table 2.3. [106]

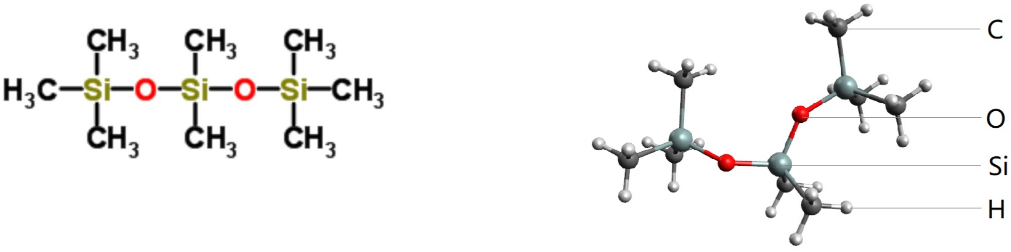

(a) 2D view

(b) 3D view

Figure 2.2: Chemical structure of $C_8H_{24}O_2Si_3$

Table 2.3: Properties of $C_8H_{24}O_2Si_3$

Gas	$C_8H_{24}O_2Si_3$
Molecular Weight	$M_g = 236.53146 \times 10^{-3}\ (kg/mol)$
Critical Pressure	$p_c = 1410045\ (Pa)$
Critical Temperature	$T_c = 564.09\ (K)$
Gas Constant	$R = 35.1516\ (J/(kg \cdot K))$
Degree of Freedom	$N = 57.96$
Specific Heat at constant volume	$c_v = N * R\ (J/(kg \cdot K))$
Constants in Van der Waals EoS	$a = \dfrac{27R^2T_c^2}{64p_c}\ (Pa \cdot m^6/kg^2)$
	$b = \dfrac{RT_c}{8p_c}\ (m^3/kg)$

The data in Table 2.3, along with the relations established in previous sections, enable the calculation of Γ over the complete $p-v$ plane outside the liquid phase dome. Based on the Van der Waals equation of state, the three significant regions of Γ are marked out in the $p-v$ plane by the $\Gamma = 0$ and $\Gamma = 1$ contour lines shown in Figure 2.3. There is a large area where $\Gamma < 1$, for which we know the sound speed of the gas decreases with pressure on an isentrope, contrary to the behavior of a regular gas. Furthermore, there is also a non-negligible region where the $\Gamma < 0$ for which many seemingly abnormal behaviors appear. We explore and present a systematic study of the various nonclassical behavior of this BZT gas in the following sections.

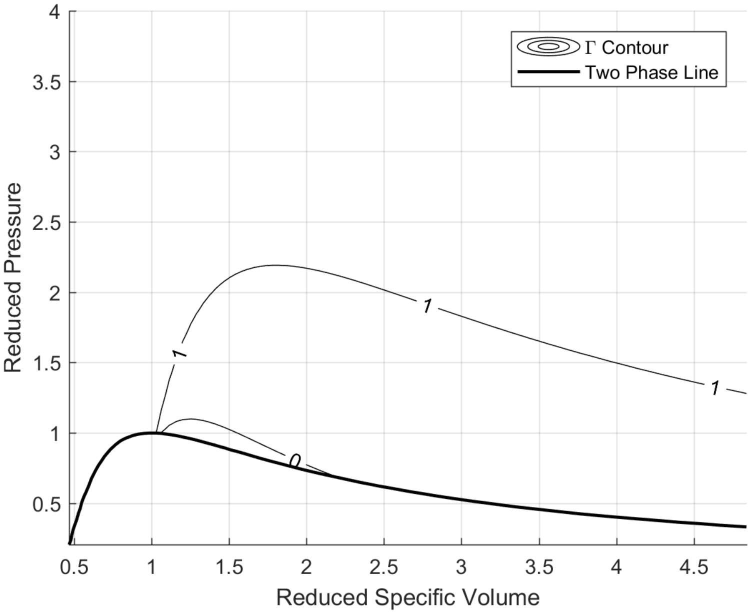

Figure 2.3: Contours of Γ in the p-v plane for MDM

2.2 General Isentropic Flow Relations for Non-ideal Gas

An ideal gas is a theoretical model that is widely used in physics and thermodynamics to describe the behavior of gases. It is an idealized concept that simplifies the properties and behavior of real gases under certain conditions. The main assumptions of an ideal gas are:

- The gas molecules are so small that their volume is negligible compared with the volume they occupy. Therefore, the molecule can be considered as a “point mass”.
- The average distance between molecules is much larger than the characteristic length of the molecules, and the gas molecules are constantly moving in random directions with a distribution of speeds.
- There is neither attractive nor repulsive energy included throughout the collision of molecules. All collisions between gas molecules or the surroundings are elastic and all motions are frictionless. No energy is lost in collisions or in motion, i.e., the kinetic energy will remain unchanged in gas molecules due to the lack of intramolecular energy.

The ideal-gas law is just an idealization or approximation of the behavior of gases. At room temperature and pressure, real gases tend to behave very much like ideal gases. However, when gas is near its critical point, forcing its molecules closer together as the space between the particles is diminished, the gas will behave less ideally. The unavailable volume for molecule motion, as well as the attraction and repulsion forces between the molecules, need to be taken into account, leading to the necessity of investigating the thermodynamics of real gases.

The study of the isentropic flow of gas in a quasi-1D channel is not only of practical importance but also forms the basis for the general field of gas dynamics, Naturally, our study of the gas dynamics of a BZT gas starts with the analysis of the quasi-1D isentropic channel flow. Quasi-one-dimensional flow means that there are no transverse variations in the flow properties. So, the properties are only changing in the direction of the flow. Although the analysis may be regarded as an approximation to the flow in a nozzle, the equations and thus the results are exact for an inviscid flow through a stream tube or streamline in a three-dimensional flow field.

2.2.1 Speed of Sound

Consider an inviscid isentropic flow through a channel of cross-sectional area $A(x)$, where x represents the flow direction. The conservation of momentum is given as

$$\rho u du + dp = 0 \tag{2.32}$$

Since the flow is isentropic, Equation (2.9) gives $v dp = \frac{c dc}{\Gamma - 1}$. Substituting the above into Equation (2.32) yields

$$u du + \frac{c dc}{\Gamma - 1} = 0 \tag{2.33}$$

In the ideal-gas situation, we are familiar with the result that as a flow accelerates its temperature and sound speed decrease monotonically. Equation (2.33) re-states this result for the ideal gas but reveals the opposite behavior for a real gas with $\Gamma < 1$, as shown in Table 2.4. For a real gas with $\Gamma < 1$, the sound speed increases as the flow accelerates downstream.

Table 2.4: Speed of sound - Velocity relation related to Γ

Γ	Gas Behavior
$\Gamma > 1$	speed of sound decreases with u
$\Gamma < 1$	speed of sound increases with u

2.2.2 Isentropic Exponents

Definition of Isentropic Exponents for Non-ideal Gases

One is familiar with the simple and elegant thermodynamic and isentropic flow relations based on the ideal-gas assumption. The familiar isentropic relations of an ideal gas are given below

$$pv^{\gamma} = constant \tag{2.34}$$

$$Tv^{\gamma-1} = constant \tag{2.35}$$

$$Tp^{\frac{1-\gamma}{\gamma}} = constant \tag{2.36}$$

where $\gamma = \dfrac{c_p}{c_v}$ is the ratio of specific heats.

The corresponding differential relations to Equations (2.34)-(2.36) are

$$\frac{dp}{p} = -\gamma \frac{dv}{v} \tag{2.37}$$

$$\frac{dT}{T} = -(\gamma - 1)\frac{dv}{v} \tag{2.38}$$

$$\frac{dp}{p} = \frac{\gamma}{\gamma - 1}\frac{dT}{T} \tag{2.39}$$

For a real gas, γ is no longer a constant and the above relations are in general invalid. In an attempt to retain the same simple exponential form, Kouremenos and Kakatsios[107] proposed the use of three different isentropic exponents corresponding to Equation (2.37) - (2.39) for each pair formed out of the variables p, v, T, expressed as γ_{pv}, γ_{Tv} and γ_{pT}, respectively. Notice these exponents are not constants. They vary with the thermodynamic state. Therefore, they should be regarded as local exponents. For example, in the (p, v)

plane the pressure-volume exponent γ_{pv} can be defined according to Equation (2.37) as

$$\left(\frac{dp}{dv}\right)_s = \gamma_{pv}\frac{p}{v} \tag{2.40}$$

Recall the expression of the entropy change in terms of pressure and specific volume

$$ds = \left(\frac{\partial s}{\partial p}\right)_v dp + \left(\frac{\partial s}{\partial v}\right)_p dv = 0 \tag{2.41}$$

Rearranging the partial derivatives yields

$$\left(\frac{dp}{dv}\right)_s = -\frac{\left(\frac{\partial s}{\partial v}\right)_p}{\left(\frac{\partial s}{\partial p}\right)_v} \tag{2.42}$$

The right-hand side of Equation (2.42) can be re-expressed using the Maxwell relations and the triple-product rule

$$-\frac{\left(\frac{\partial s}{\partial v}\right)_p}{\left(\frac{\partial s}{\partial p}\right)_v} = \frac{\left(\frac{\partial p}{\partial T}\right)_s}{\left(\frac{\partial v}{\partial T}\right)_s} = \frac{\left(\frac{\partial p}{\partial s}\right)_T\left(\frac{\partial s}{\partial T}\right)_p}{\left(\frac{\partial v}{\partial s}\right)_T\left(\frac{\partial s}{\partial T}\right)_v} = -\frac{c_p}{c_v}\left(\frac{\partial T}{\partial v}\right)_p\left(\frac{\partial p}{\partial T}\right)_v = \frac{c_p}{c_v}\left(\frac{\partial p}{\partial v}\right)_T \tag{2.43}$$

where $c_p/T = \left(\frac{\partial s}{\partial T}\right)_p$ and $c_v/T = \left(\frac{\partial s}{\partial T}\right)_v$.

Combining Equations (2.40), (2.42) and (2.43), we obtain the pressure-volume exponent in terms of the state variables

$$\gamma_{pv} = -\frac{v}{p}\frac{c_p}{c_v}\left(\frac{\partial p}{\partial v}\right)_T \tag{2.44}$$

Similarly, the temperature-volume exponent can be defined in accordance with Equation

(2.38), as derived from the temperature-volume relation along an isentrope, i.e,

$$\gamma_{Tv} = 1 - \frac{v}{T}\left(\frac{dT}{dv}\right)_s \tag{2.45}$$

Starting with defining the entropy as a function of temperature and specific volume $s = s(T, v)$, the derivatives are related as

$$\left(\frac{dT}{dv}\right)_s = -\frac{\left(\dfrac{\partial s}{\partial v}\right)_T}{\left(\dfrac{\partial s}{\partial T}\right)_v} \tag{2.46}$$

Following the same steps as previously for the pressure-volume exponent, we obtain the expression for the temperature-volume exponent

$$\gamma_{Tv} = 1 + \frac{v}{c_v}\left(\frac{\partial p}{\partial T}\right)_v \tag{2.47}$$

As in the cases of deriving the previous two isentropic exponents, the pressure-temperature exponent is defined from Equation (2.39) as

$$\frac{\gamma_{pT}}{\gamma_{pT} - 1} = \frac{T}{p}\left(\frac{dp}{dT}\right)_s \tag{2.48}$$

We again express it in terms of only the equation of state. Note

$$\left(\frac{dp}{dT}\right)_s = -\frac{\left(\dfrac{\partial s}{\partial T}\right)_p}{\left(\dfrac{\partial s}{\partial p}\right)_T} \tag{2.49}$$

The final expression of the pressure-temperature exponent is given as

$$\gamma_{pT} = \frac{1}{1 - \dfrac{p}{c_p}\left(\dfrac{\partial v}{\partial T}\right)_p} \tag{2.50}$$

Notice that the exponents as defined above are identical to γ for the ideal-gas case. For a general real gas, they are different and non-constant. However, only two of the three are independent. Eliminating the partial derivatives, the relation between the three real isentropic exponents is

$$\frac{\gamma_{pv}}{\gamma_{Tv} - 1} = \frac{\gamma_{pT}}{\gamma_{pT} - 1} \tag{2.51}$$

Other Variables in Terms of Isentropic Exponents

By defining the three isentropic exponents, other flow properties can be derived from them or be related to them, including entropy production, speed of sound and Mach number, etc.

Consider the entropy change as a function of temperature and specific volume

$$ds = \left(\frac{\partial s}{\partial T}\right)_v dT + \left(\frac{\partial s}{\partial v}\right)_T dv \tag{2.52}$$

Replacing the term $\left(\dfrac{\partial s}{\partial T}\right)_v$ by $\dfrac{c_v}{T}$ and substituting Equation (2.47) into the second term on the right hand side in Equation (2.52) yields

$$ds = c_v \frac{dT}{T} + c_v(\gamma_{Tv} - 1)\frac{dv}{v} \tag{2.53}$$

The speed of sound can be derived as

$$c^2 = \left(\frac{\partial p}{\partial \rho}\right)_s = -v^2 \left(\frac{\partial p}{\partial v}\right)_s = \gamma_{pv} p v \tag{2.54}$$

and thus the Mach number is

$$M = \frac{u}{c} = \frac{u}{\sqrt{\gamma_{pv} p v}} \tag{2.55}$$

2.2.3 Stagnation Properties

In fluid dynamics, the total or stagnation properties of the fluid provide a convenient reference state of a fluid in motion. Looking into the original definition of total properties, the total pressure and total density are the pressure and density at the stagnation point when the fluid is brought to rest isentropically, and the total temperature is the temperature at the stagnation point when the fluid is brought to rest adiabatically. At a stagnation point, the speed of the fluid is zero, and all of the kinetic energy has been converted to internal energy and is added to the local static enthalpy. Classical theory has already established the analytical expressions for the stagnation properties for a calorically perfect gas, which are

$$h_0 = c_p T_0 \tag{2.56}$$

$$p_0 = p \left[1 + \frac{\gamma - 1}{2} M^2\right]^{\frac{\gamma}{\gamma - 1}} \tag{2.57}$$

$$T_0 = T \left[1 + \frac{\gamma - 1}{2} M^2\right] \tag{2.58}$$

$$\rho_0 = \rho \left[1 + \frac{\gamma - 1}{2} M^2\right]^{\frac{1}{\gamma - 1}} \tag{2.59}$$

These familiar equations are no longer valid for real gases. To build up a theory of stagnation properties for real gases, the first step is to understand the change of isentropic exponents

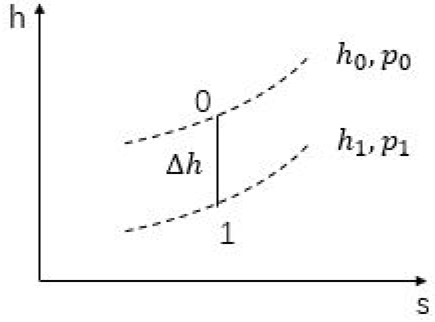

Figure 2.4: Sketch of total enthalpy definition

along the isentrope. Nederstigt [108] introduced the assumption of locally constant values for the isentropic exponents between isentropic states. For low subsonic flows, the kinetic energy contained in the flow is much smaller than the static enthalpy of the flow, leading to small changes in the isentropic state so that the isentropic exponents can be assumed to be constants along the stagnation process. However, this assumption leads to an inaccurate evaluation of the stagnation properties. The differences between applying this assumption and using the original definition will be shown in this section.

Unquestionably, the utilization of the original definition for performing exact integration to the stagnation point represents the most precise and reliable method for calculating stagnation properties. However, this approach is not feasible in practical applications due to its slow convergence, leading to prolonged computational time. Despite this limitation, the results by using the original definition can serve as a valuable reference point for the results obtained through other alternative techniques. For instance, let's consider a fluid situated at a specific location with a velocity $V \neq 0$. By initiating a minuscule thermodynamic state change during each iteration to ensure the process remains isentropic, the conservation equations can be integrated directly to get the thermodynamic properties for the next state. Then the thermodynamic properties at each new state are recorded and the process is iteratively repeated. This sequence of gradual, isentropic changes eventually brings the fluid to rest, i.e., $V = 0$. The thermodynamic properties recorded at this final state represent the accurate stagnation properties. This process is rigorous and detailed which underscores the complex relationship between velocity and thermodynamic properties in a fluid system. However, it can only be treated as a methodological foundation for understanding the stagnation properties of real gases. More efficient computational models need to be developed in practical applications.

To derive the total properties in terms of isentropic exponents, we used modified equations to replace the above relation for real gases by using the isentropic exponents discussed above. We show in this section that such treatment may lead to large errors.

Beginning with the principle of conservation of total enthalpy, we have

$$\begin{aligned} h_0 &= h + \frac{u^2}{2} = constant \\ \Delta h &= \frac{u^2}{2} \end{aligned} \tag{2.60}$$

where Δh is the enthalpy change from the current state to the stagnation state.

The expression of enthalpy change may also be calculated by the thermodynamic relation

$$dh = Tds + vdp \tag{2.61}$$

In an isentropic process, $ds = 0$. Thus, the enthalpy change from state 1 to state 2 is

$$\begin{aligned} h_2 - h_1 &= \int_1^2 vdp = \int_1^2 v_1 \left(\frac{p_1}{p}\right)^{\frac{1}{\gamma_{pv}}} dp = v_1 p_1 \left(\frac{\gamma_{pv}}{\gamma_{pv}-1}\right) \left[\left(\frac{p_2}{p_1}\right)^{\frac{\gamma_{pv}-1}{\gamma_{pv}}} - 1\right] \\ \Delta h &= vp \left(\frac{\gamma_{pv}}{\gamma_{pv}-1}\right) \left[\left(\frac{p_0}{p}\right)^{\frac{\gamma_{pv}-1}{\gamma_{pv}}} - 1\right] \end{aligned} \tag{2.62}$$

Here the assumption of a locally constant value of γ_{pv} is applied. In other words, Equation (2.62) is only valid for small thermodynamic state changes. Both Equations (2.60) and (2.62) describe the enthalpy change through an isentropic process. Equating Equations. (2.60) and (2.62) and making use of Equation. (2.54) lead to

$$\frac{p_0}{p} = \left[1 + \frac{\gamma_{pv} - 1}{2} M^2\right]^{\frac{\gamma_{pv}}{\gamma_{pv}-1}} \tag{2.63}$$

The total pressure for real-gas flow in terms of the isentropic exponent γ_{pv} is given as

$$p_0 = p\left[1 + \frac{\gamma_{pv} - 1}{2} M^2\right]^{\frac{\gamma_{pv}}{\gamma_{pv}-1}} \tag{2.64}$$

Derived by the same procedure, the total temperature and total density in terms of the isentropic exponents are

$$T_0 = T\left[1 + \frac{\gamma_{pv} - 1}{2} M^2\right]^{\frac{\gamma_{Tv}-1}{\gamma_{pv}-1}} \tag{2.65}$$

$$\rho_0 = \rho\left[1 + \frac{\gamma_{pv} - 1}{2} M^2\right]^{\frac{1}{\gamma_{pv}-1}} \tag{2.66}$$

The form of these expressions of total variables is similar to those that have been commonly used for ideal-gas computation. To compare them with the ideal-gas law, Figures 2.5, 2.6 and 2.7 plot the static-to-total pressure, temperature, and density ratios computed by the ideal-gas law and the above-modified equations for the given static condition $p = 1.1p_c$, $T = 1.025T_c$, $v = 1.0v_c$, with varying different flow Mach number. They are compared to the accurate solutions by applying the definitions of stagnation properties. The figures show that for a small Mach number ($M < 0.5$), the isentropic exponents are a good approximation for the exact solution, better than the use of the ideal-gas law. However, for a high Mach number, the differences are not negligible and can lead to completely wrong answers. The static-to-total pressure, temperature, and density ratios go to zero at point $M^2 = (\frac{2}{1 - \gamma_{pv}})$ (in this case $M \approx 1.615$). Notice that when applying Equations (2.64), (2.65), and (2.66) to calculate the total variables, γ_{pv}, γ_{Tv}, and γ_{pT} are constants obtained from the thermodynamic state of the initial point. The results again demonstrate that it is necessary to update the values of the isentropic exponents γ_{pv}, γ_{Tv}, and γ_{pT} at each point based on the local thermodynamic variables.

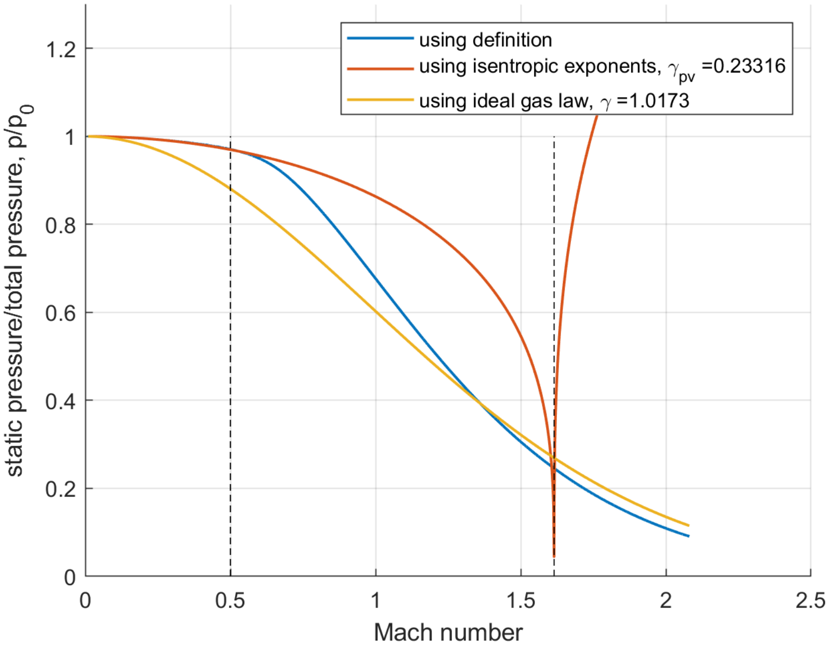

Figure 2.5: Comparison of static-to-total pressure ratio calculated by different methods (MDM gas)

As a second example, consider an isentropic expansion of a flow (say in a one-dimensional channel) starting from the stagnation pressure $p_{in} = 1.1p_c$ and the specific volume $v_{in} = 1.0v_c$ to a back pressure $p_b = 0.5p_c$. By integrating the exact isentropic relations, we can obtain the exact static properties, such as p and v as a function of Mach number M along the channel. However, if we were to calculate the p_0, T_0, and ρ_0 based on the local static properties and Mach number by using Equation (2.64), (2.65), and (2.66), we would obtain values of p_0, T_0, and ρ_0 as functions of M shown in Figures 2.8, 2.9, and 2.10 for the MDM gas. At relatively low Mach numbers, both the ideal-gas law and the relation based on the isentropic exponents agree with the exact solution well, but they both fail as M increases. The errors by using the ideal-gas law appear first around $M = 0.1$ and lead to inaccurate results for a

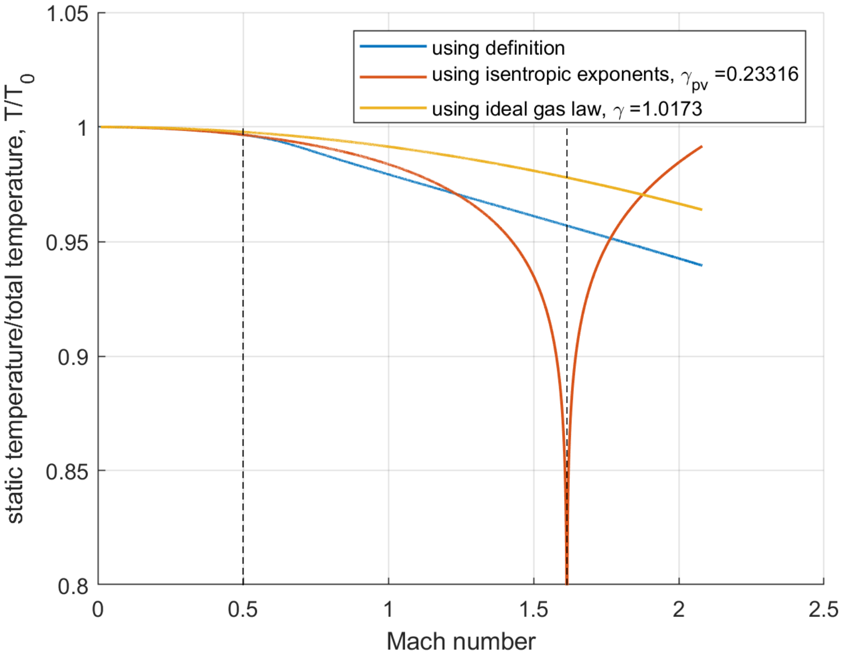

Figure 2.6: Comparison of static-to-total temperature ratio calculated by different methods (MDM gas)

high Mach number. The errors by using the isentropic exponents are smaller than the use of the ideal-gas law for small Mach numbers, but as M increases beyond 0.5, it grows rapidly to become unusable. The total pressure, total temperature, and total density are grossly under-predicted by using the isentropic exponents.

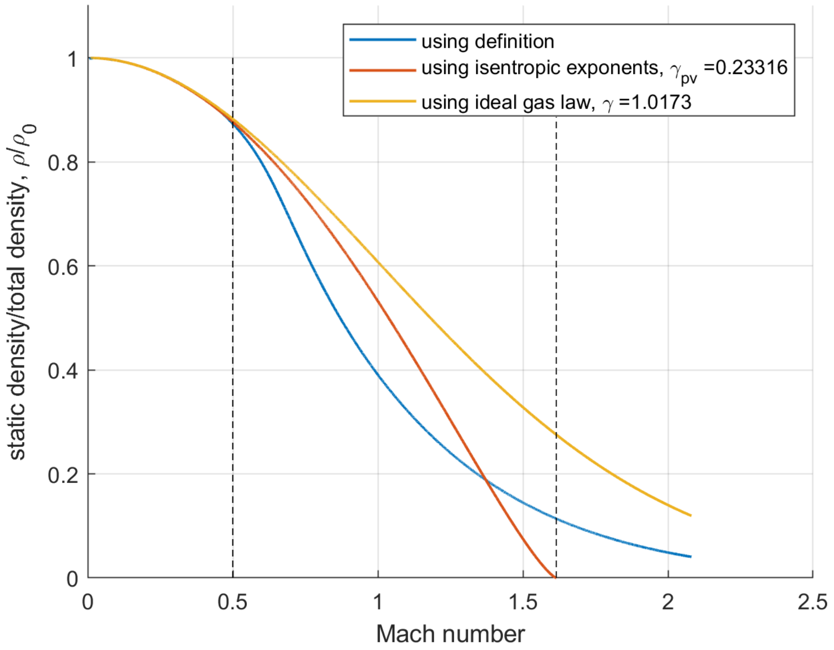

Figure 2.7: Comparison of static-to-total density ratio calculated by different methods (MDM gas)

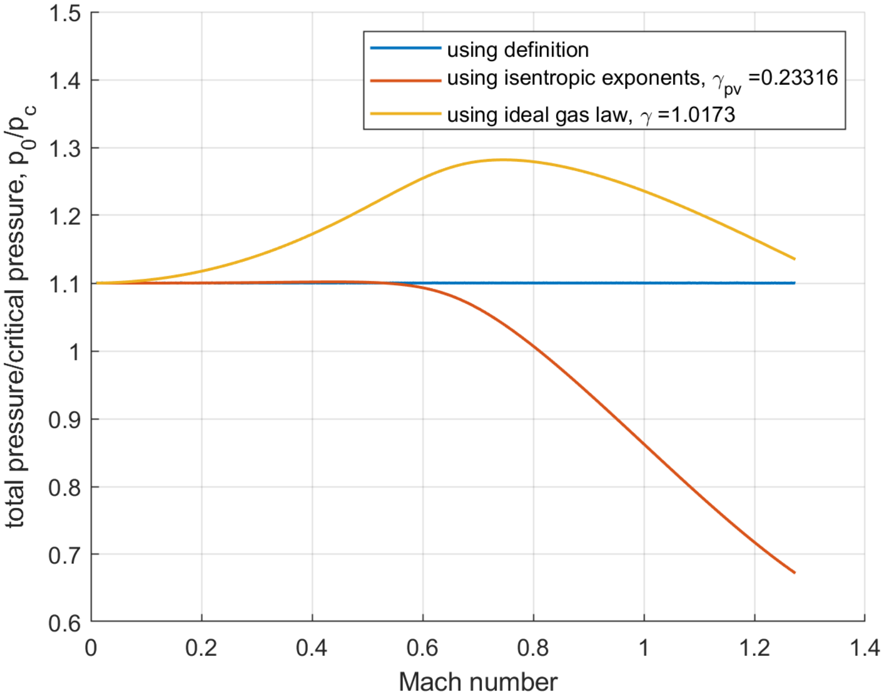

Figure 2.8: Comparison of total pressure calculated by different methods

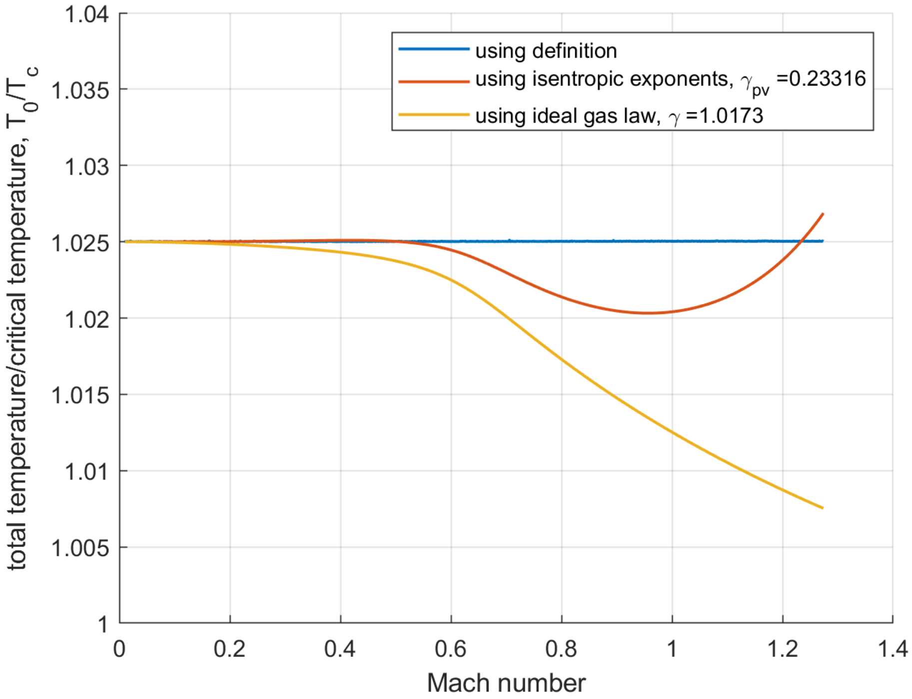

Figure 2.9: Comparison of total temperature change calculated by different methods

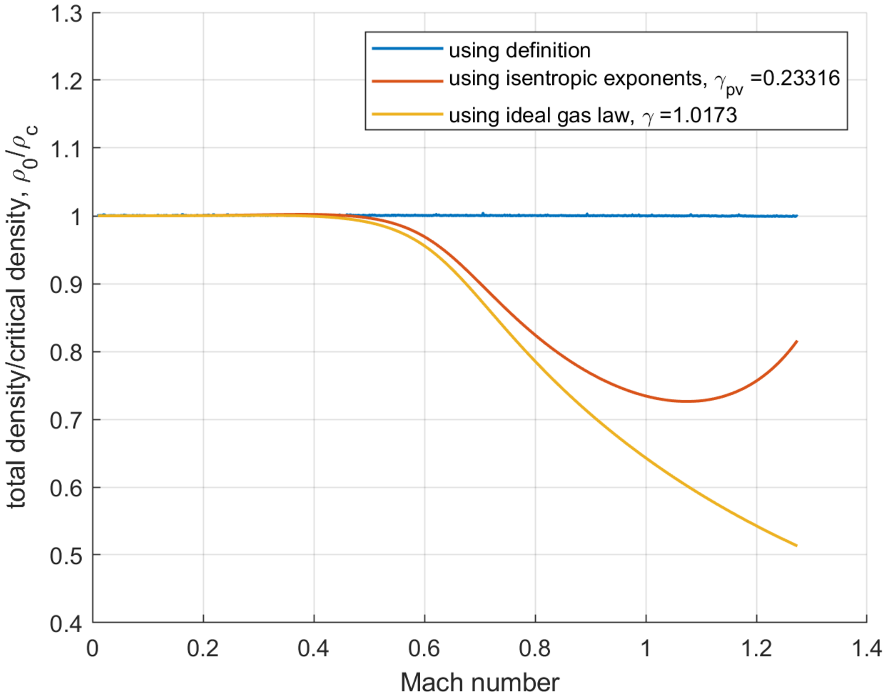

Figure 2.10: Comparison of total density change calculated by different methods

Figure 2.11 shows the variation of different exponents γ_{pv}, γ_{Tv} and γ_{pT} during the above isentropic expansion process, together with the value of c_p/c_v and $(c_v + R)/c_v$ (the γ defined in perfect gas law). The c_p here is calculated by using the Van der Waals equation of state. Usually, the values of these exponents are larger than 1. However, within the nonclassical region, the isentrope is a convex curve in the p-v diagram (Figure 2.1), leading to the value of γ_{pv} much smaller than 1. The large variations of the isentropic exponents during an isentropic flow explain the occurrence of huge errors by using the isentropic exponent's approach for high-speed flows. Figure 2.12 is the isentrope plotted on a logarithmic scale, compared with an isentrope passing through the same thermodynamic state but calculated with ideal-gas assumption. This deviation of the slope demonstrates the inaccuracies by using the ideal-gas law. Stagnation pressure and enthalpy (or stagnation temperature) are critical quantities used in assessing the power and efficiencies of a turbomachinery. Therefore, caution must be taken in obtaining such values in any engine cycle analysis or CFD computation of the flow in a compressor or turbine of engines that use a dense gas as the working fluid.

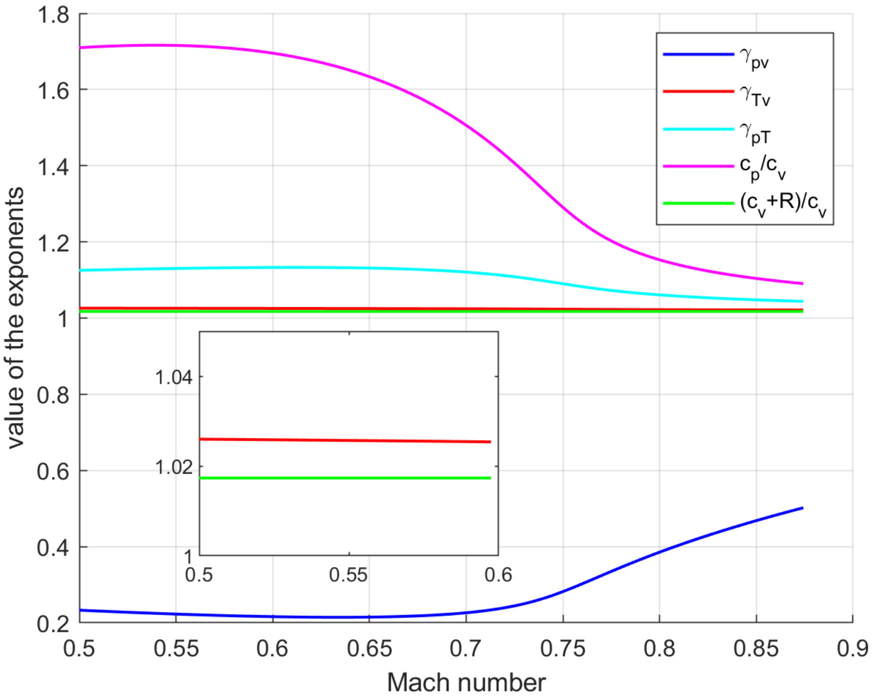

Figure 2.11: Comparison of the variation of different exponents

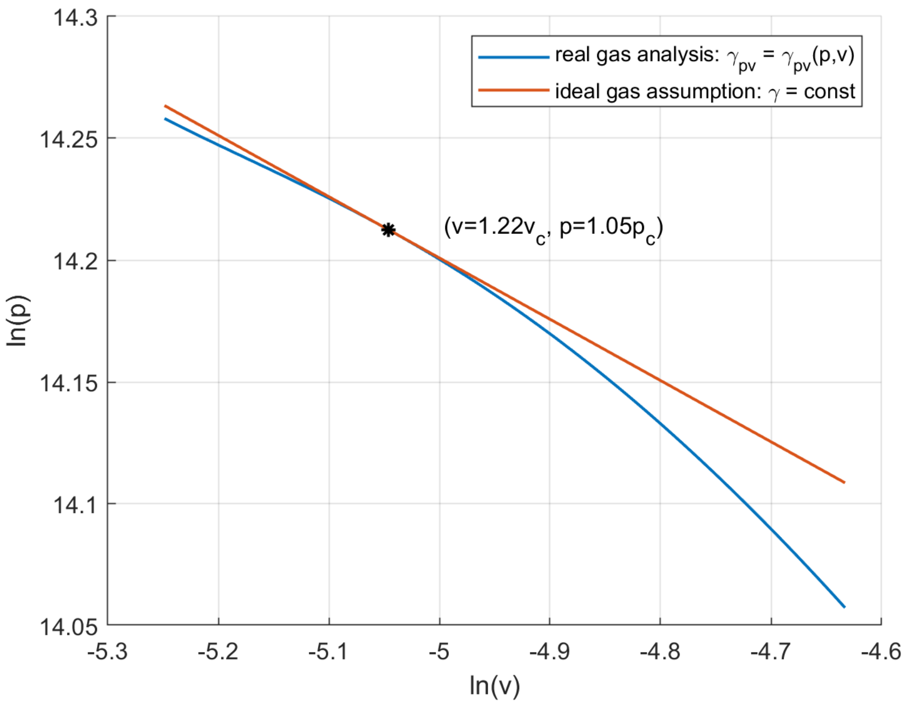

Figure 2.12: Comparison of the real isentropic exponent γ_{pv} with ideal gas γ

2.2.4 Mach - Velocity Relation

Recall Equation (2.33)

$$udu + \frac{cdc}{\Gamma - 1} = 0$$

Let $M = u/c$, substitute M into the equation above and simplify the result.

$$\begin{aligned} dM &= \frac{1}{c}du - \frac{u}{c^2}dc \\ \frac{dc}{c} &= \frac{du}{u} - \frac{dM}{M} \\ udu + \frac{c^2}{\Gamma - 1}\left(\frac{du}{u} - \frac{dM}{M}\right) &= 0 \end{aligned}$$

Then, the relation between velocity and Mach number is

$$\frac{du}{u} = \frac{1}{1+(\Gamma-1)M^2}\frac{dM}{M} \tag{2.67}$$

Equation (2.67) shows how the Mach number would be changed with velocity. For any classical gas with $\Gamma > 1$, the Mach number always increases with the velocity monotonically. However, for a nonclassical gas when Γ goes below 1, the change of Mach number would be depending on the sign of the term $1+(\Gamma-1)M^2$. When $M^2 < \dfrac{1}{1-\Gamma}$, the Mach number still increases with velocity like how it behaves in the classical gas case. Otherwise, if $M^2 > \dfrac{1}{1-\Gamma}$, the Mach number will decrease with increasing velocity, contrary to the classical knowledge for a regular gas. This is because the sound speed increases faster than the flow velocity as the pressure decrease due to the velocity increase.

Table 2.5: Mach - Velocity relation related to Γ

Γ	Gas Behavior
$\Gamma > 1$	M increases monotonically with u
$\Gamma < 1$	M increases with u only for $M^2 < \dfrac{1}{1-\Gamma}$

2.2.5 Mach - Area Relation

Consider a quasi-1D isentropic flow, the following velocity-area relation is obtained by combining the continuity and momentum equations and making one of the definition of sound speed

$$\frac{1}{u}\frac{du}{dx} = \frac{M^2-1}{A}\frac{dA}{dx} \tag{2.68}$$

Substituting Equation (2.68) into Equation (2.67), the relation between Mach number and area change is

$$\frac{1}{M}\frac{dM}{dx} = \frac{1+(\Gamma-1)M^2}{M^2-1}\frac{1}{A}\frac{dA}{dx} \tag{2.69}$$

Equation (2.69) states that the transition between subsonic and supersonic flow only occurs when $\dfrac{dA}{dx} = 0$, and how the Mach number changes regarding to area ratio is related to the sign of $(1+(\Gamma-1)M^2)/(M^2-1)$. For a conventional gas for which $\Gamma > 1$, the Mach number increases in supersonic flow and decreases in subsonic flow with the increasing cross-sectional area ratio. However, for nonclassical gas cases where $\Gamma < 1$, there are some different gas behaviors shown below.

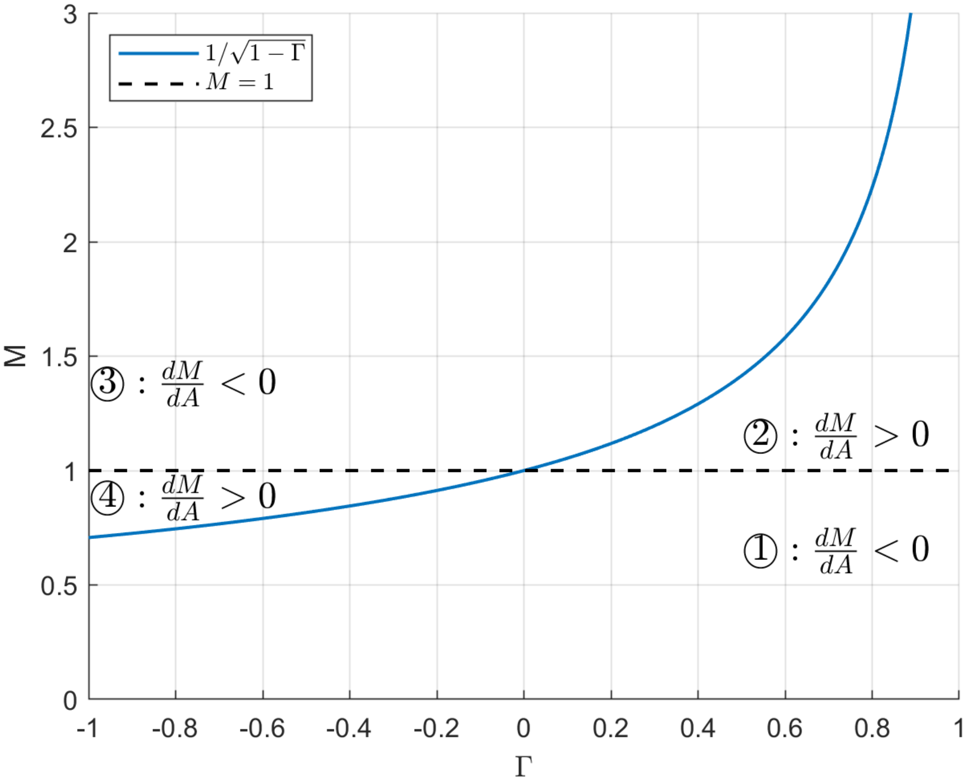

Figure 2.13: Mach number - Area relation related to Γ (for $\Gamma < 1$)

Figure 2.13 maps out four regions where $\dfrac{dM}{dA}$ changes sign in the (M, Γ) domain. In regions ① and ② where $M^2 < \dfrac{1}{1-\Gamma}$, the flow behaves the same way as the classical theory predicts. A converging channel accelerates a subsonic flow ($\dfrac{dM}{dA} < 0$) and decelerates a supersonic flow ($\dfrac{dM}{dA} > 0$). In regions ③ and ④ however, the flow behaves in completely opposite way to a conventional gas. A diverging channel accelerates a subsonic flow ($\dfrac{dM}{dA} > 0$) and decelerates a supersonic flow ($\dfrac{dM}{dA} < 0$). It is clear then that, in order to accelerate a subsonic flow from subsonic to supersonic flow or decelerate a supersonic flow to subsonic flow isentropically, one has to use a diverging-converging channel. To investigate the flow properties at the transonic point, the second-order derivative with respect to area ratio change needs to be derived from Equation (2.69). To avoid the singular value at the transonic point $M = 1$, apply $L'Hospital's$ rule to Equation (2.69)

$$\lim_{M\to 1}\frac{dM}{dx} = \lim_{M\to 1}\frac{\frac{d}{dx}\left[\left(1+(\Gamma-1)M^2\right)\frac{M}{A}\frac{dA}{dx}\right]}{\frac{d}{dx}\left[M^2-1\right]} \tag{2.70}$$

When $M \to 1, \dfrac{dA}{dx} \to 0$, so

$$\lim_{M\to 1}\frac{dM}{dx} = \lim_{M\to 1}\frac{1+(\Gamma-1)M^2}{2A\frac{dM}{dx}}\frac{d^2A}{dx^2} = \frac{\Gamma}{2A\frac{dM}{dx}}\frac{d^2A}{dx^2} \tag{2.71}$$

Rearrange the equation

$$\left(\frac{dM}{dx}\right)^2 = \frac{\Gamma}{2A}\frac{d^2A}{dx^2} \tag{2.72}$$

The LHS of Equation (2.72) is always non-negative. So, for gases with Γ greater than 0, the sonic point has the minimum cross-sectional area. However, when Γ goes smaller than 0, the cross-sectional area will have the maximum value at the sonic point. Instead of the classical convergent-divergent nozzle, here, a divergent-convergent nozzle will be needed for nonclassical gas transonic flow.

2.2.6 Differential Form of Conservation Laws

As discussed before, quasi-one-dimensional (Q1D) flow means that the flow properties change only in the direction of the flow and there are no transverse variations in the flow properties. In practical terms, a necessary (but not sufficient) condition for using the Q1D relations is that the channel cross-sectional area has gradual variations. This simplification is quite

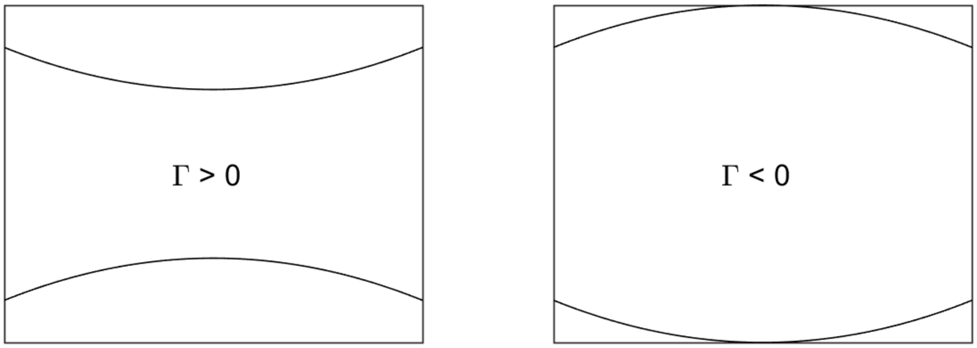

Figure 2.14: Transonic nozzle related to Γ

helpful and leads us to some interesting results.

Consider the flow through a channel with a cross-sectional area $A(x)$ along the flow direction x. A mono-component, single-phase fluid flows isentropically through this channel. The conservation equations of mass, momentum, and energy are:

$$\begin{cases} \dfrac{d\rho}{\rho} + \dfrac{du}{u} + \dfrac{dA}{A} = 0 \\ \rho u du + dp = 0 \\ dh + u du = 0 \end{cases} \tag{2.73}$$

Equation (2.73) is the general form of conservation laws for isentropic Q1D flow. All the analyses for unconventional gas behavior in the present work are based on these equations. Rewriting Equation (2.73) with expressions from previous sections gives the following:

Momentum conservation:

$$\rho u du + dp = 0 \tag{2.74}$$

$$\rho u du + \left(\frac{\partial p}{\partial \rho}\right)_T d\rho + \left(\frac{\partial p}{\partial T}\right)_\rho dT = 0 \tag{2.75}$$

Energy conservation:

$$dh + udu = 0 \tag{2.76}$$

$$c_p dT + \left[v - T\left(\frac{\partial v}{\partial T}\right)_p\right] dp + udu = 0 \tag{2.77}$$

In practical conditions, the upstream and the downstream pressure of the channel will be given in most cases. To keep consistency with that, here, the pressure is selected as the independent variable and all the other variables will be written in terms of p.

First of all, the velocity variation with p can be derived from Equation (2.74) directly

$$\frac{du}{dp} = -\frac{1}{\rho u} \tag{2.78}$$

The temperature difference regarding pressure is then given by Equation (2.77)

$$\frac{dT}{dp} = \frac{T}{c_p}\left(\frac{\partial v}{\partial T}\right)_p \tag{2.79}$$

Once the temperature equation is obtained, substitute it into the following expression of dp

$$dp = \left(\frac{\partial p}{\partial \rho}\right)_T d\rho + \left(\frac{\partial p}{\partial T}\right)_\rho dT \tag{2.80}$$

which leads to the expression of density change with pressure

$$\frac{d\rho}{dp} = \frac{1 - \frac{T}{c_p}\left(\frac{\partial p}{\partial T}\right)_\rho \left(\frac{\partial v}{\partial T}\right)_p}{\left(\frac{\partial p}{\partial \rho}\right)_T} \tag{2.81}$$

So far, the ordinary-differential-equation system for quasi-1D nozzle flow calculation is obtained:

$$\begin{cases} \dfrac{du}{dp} = -\dfrac{1}{\rho u} \\ \dfrac{dT}{dp} = \dfrac{T}{c_p}\left(\dfrac{\partial v}{\partial T}\right)_p \\ \dfrac{d\rho}{dp} = \dfrac{1 - \dfrac{T}{c_p}\left(\dfrac{\partial p}{\partial T}\right)_\rho \left(\dfrac{\partial v}{\partial T}\right)_p}{\left(\dfrac{\partial p}{\partial \rho}\right)_T} \end{cases} \tag{2.82}$$

To determine the local Mach number at each point, recall the Mach number-velocity relation, Equation (2.67)

$$\frac{du}{u} = \frac{1}{1 + (\Gamma - 1)M^2}\frac{dM}{M}$$

The Mach number variation versus pressure is obtained by combining Equation (2.67) with Equation (2.78), which gives

$$\frac{dM}{dp} = -M(1 + (\Gamma - 1)M^2)\frac{1}{\rho u^2} \tag{2.83}$$

2.3 Nonclassical Behavior of a BZT Gas in Q1D Flow

To show the differences between conventional and unconventional gas behavior more clearly, several channel cases are computed. The gas MDM introduced in section 2.1 is selected as the working fluid in the computation. By judicially choosing the initial conditions, there are some particular sections within the channel that the negative fundamental derivative condition could be achieved.

Section 2.3.1 summarizes the general differential equations for quasi-one-dimensional isentropic flow. Section 2.3.2 and section 2.3.3 examine two isentropic flow cases starting from the same thermodynamic state $p_{in} = 1.1p_c, v_{in} = 0.8v_c$, one with an initial subsonic speed

$M = 0.5$ and the other with supersonic speed $M = 3.0$. The inlet point is chosen to be as close to the critical point. In this way, the isentropic process we examine will have a segment that falls within the negative fundamental derivative region and then stay in the $\Gamma < 1$ region until the nozzle outlet. Both cases show interesting results which are opposite to the conventional behavior. For comparison with the flow of an ideal gas, results computed based on the ideal-gas law with properties specified at the same initial inlet conditions are also presented.

2.3.1 General Differential Equations for Quasi-One-Dimensional Isentropic Flow

Building on prior discussions, we have collated the essential differential equations required for numerical computations in Table 2.6. These relations are universally applicable and offer the flexibility of computation across various gas models. They are suitable for use with a variety of equations of state, including but not limited to, the Van der Waals (VdW), Soave-Redlich-Kwong (SRK), or Peng-Robinson (PR) models.

Table 2.6: Quasi-1D isentropic flow equations for non-conventional gas

Flow Variable	Calculation Formula
pressure	dp is taken as the independent variable
density	$\dfrac{d\rho}{dp} = \dfrac{1 - \dfrac{T}{c_p}\left(\dfrac{\partial p}{\partial T}\right)_{\rho}\left(\dfrac{\partial v}{\partial T}\right)_{p}}{\left(\dfrac{\partial p}{\partial \rho}\right)_{T}}$
temperature	$\dfrac{dT}{dp} = \dfrac{T}{c_p}\left(\dfrac{\partial v}{\partial T}\right)_{p}$
velocity	$\dfrac{du}{dp} = -\dfrac{1}{\rho u}$
cross-sectional area	$\dfrac{dA}{dp} = A\left(\dfrac{1}{\rho u^2} - \dfrac{\left[1 - \dfrac{T}{c_p}\left(\dfrac{\partial p}{\partial T}\right)_{\rho}\left(\dfrac{\partial v}{\partial T}\right)_{p}\right]}{\rho\left(\dfrac{\partial p}{\partial \rho}\right)_{T}}\right)$
Mach number	$\dfrac{dM}{dp} = -M(1 + (\Gamma - 1)M^2)\dfrac{1}{\rho u^2}$
Enthalpy	$dh = c_p dT + \left[v - T\left(\dfrac{\partial v}{\partial T}\right)_{p}\right] dp$
Specific Heat	$c_p - c_v = T\left(\dfrac{\partial v}{\partial T}\right)_{p}\left(\dfrac{\partial p}{\partial T}\right)_{v}$
Fundamental Derivative	$\Gamma(T, v) = \dfrac{v^3}{2c^2}\left[\dfrac{\partial^2 p}{\partial v^2} - \dfrac{3T}{c_v}\dfrac{\partial p}{\partial T}\dfrac{\partial^2 p}{\partial T \partial v} + \left(\dfrac{T}{c_v}\dfrac{\partial p}{\partial T}\right)^2\left[3\dfrac{\partial^2 p}{\partial T^2} + \dfrac{1}{T}\dfrac{\partial p}{\partial T}\left(1 - \dfrac{T}{c_v}\dfrac{\partial p}{\partial T}\right)\right]\right]$

This system of ODEs can be easily integrated numerically by a Runge-Kutta method with a uniform pressure increment of $dp = 10^{-4} p_c$ between each interval. Vieta's formulas[109] are used to solve the EoS defined in Equation (2.12).

2.3.2 Isentropic Flow with Subsonic Inlet Condition

Consider the flow in a nozzle with a specified continuously decreasing pressure profile. The needed cross-sectional area change is to be determined based on the pressure change. The flow starts at the initial static condition $p = 1.1p_c$ and $v = 0.8v_c$ and at a Mach number $M = 0.5$. The isentropic expansion process is plotted in the p-v diagram in Figure 2.15 together with the vapor dome and the $\Gamma = 0$ and 1 boundaries. The starting point is chosen to be slightly above the critical point and close to the vapor dome so that the isentrope goes through a longer segment in the negative fundamental derivative region.

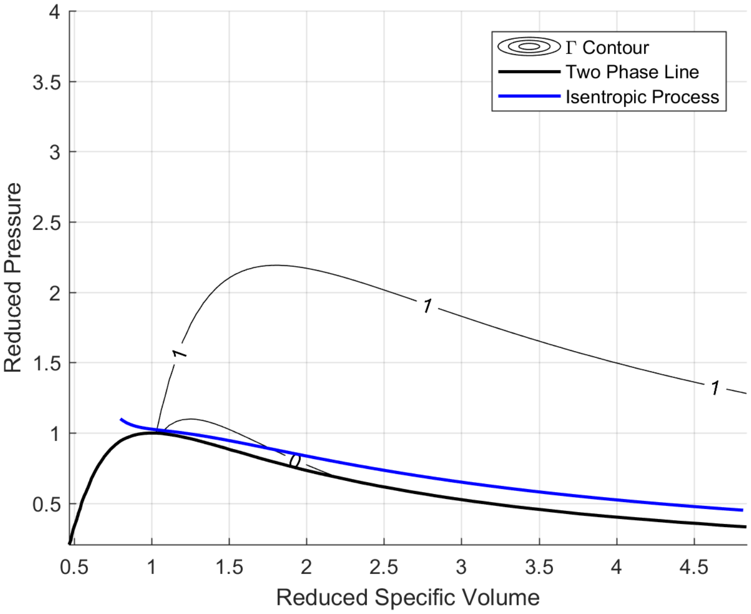

Figure 2.15: Case 1: $p_{in} = 1.1p_c, M_{in} = 0.5, v_{in} = 0.8v_c$

The fundamental derivative is a thermodynamic property of the gas along with temperature and sound speed. Therefore, they are uniquely determined as functions of pressure and specific volume only and can be calculated along the isentrope by using isentropic thermodynamic relations without integrating the ODEs for the flow. To facilitate the visualization of the flow behavior of the gas that accomplishes such an isentropic expansion process in a 1D channel, the pressure variation along the channel is specified as a parabolic function along the flow direction as shown in figure 2.16a. Figure 2.16b shows the change of the fundamental derivative with the static pressure. Γ is in the conventional regime at $p_r = 1.1$ and then drops rapidly when the pressure starts to decrease. This drop happens close to the critical point in the p-v diagram when the isentrope goes across multiple Γ contour lines so that Γ first drops below 1.0 and continues to drop below 0 until $\Gamma \approx -1$ before it recovers gradually back to Γ nearly but still below 1. It reaches its minimum when the pressure is equal to the critical pressure of the gas. It looks like that Γ stays in the $\Gamma < 1$ region forever until the nozzle outlet. One may ask if the isentrope can cross the $\Gamma = 1$ boundary. The answer is 'Yes'. Γ will eventually go greater than 1 if the gas is going to be expanded to a super low pressure at the nozzle outlet. Based on our computations, it requires the outlet pressure to be hundreds of times smaller than the inlet pressure.

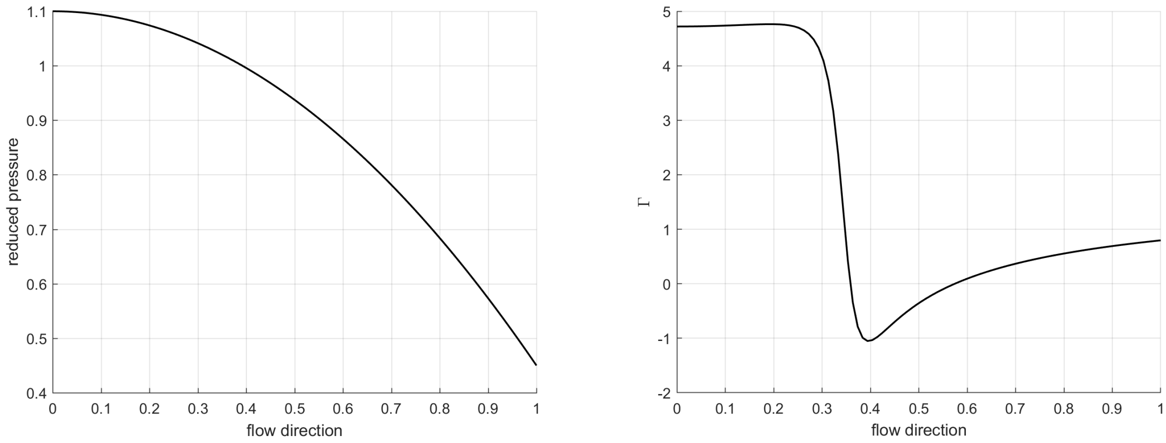

(a) Pressure Profile

(b) Fundamental Derivative

Figure 2.16: Variation of pressure and fundamental derivative along the channel for Case 1

Figure 2.17 shows how temperature changes along the isentrope. The initial temperature by using the ideal-gas law is very different from that of the Van der Waals model. Both the Van der Waals model and the ideal-gas law present a monotonic decrease in temperature as the pressure drops in the isentropic expansion. However, the temperature ratio relative to the initial temperature drops more for the Van der Waals gas than for the ideal gas. This is plotted in figure 2.18. Figure 2.19 shows the density variations along the channel. The density drops also monotonically, but the density by the real-gas model drops more than that by the ideal-gas law because of the increased sensitivity of pressure on density to account for the finite size of the molecules and the inter-molecular interactions for the real gas at high-pressure levels. In terms of the specific volume, the real gas expands more in volume for the same pressure drop. This means more internal energy is converted to the kinetic energy of the fluid, resulting in the higher relative temperature drop for the real gas shown in figure 2.18.

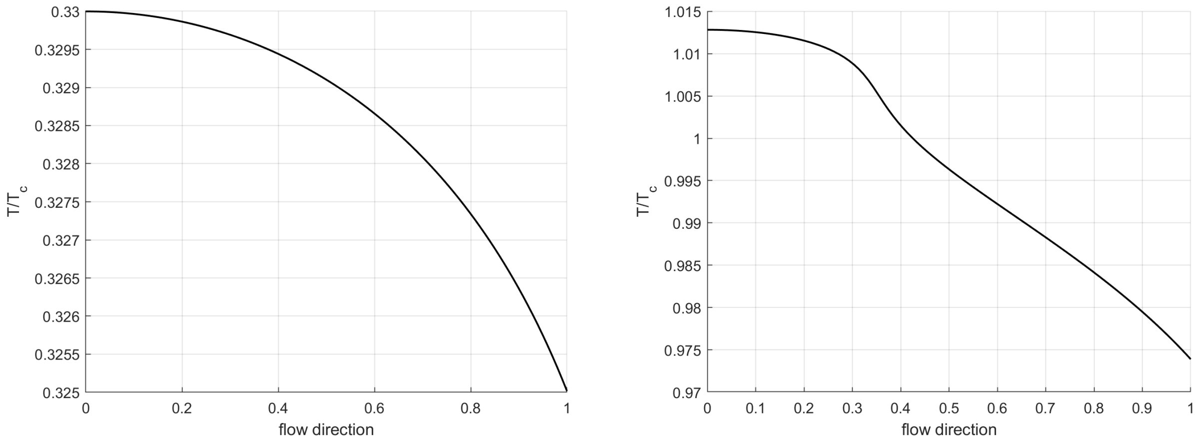

(a) Ideal Gas Model (b) Van der Waals Gas Model

Figure 2.17: Variation of temperature along the channel for Case 1

Regarding the curvature change of density in the Van der Waals model results, recall Equation (2.1) for the definition of Γ

$$\Gamma = \frac{c^4}{2v^3}\left(\frac{\partial^2 v}{\partial p^2}\right)_s$$

It states that the curvature of the density function is related to the sign of Γ. For an ideal gas, Γ is always a positive number which leads to positive $\left(\frac{\partial^2 v}{\partial p^2}\right)_s$. However, for a non-conventional gas, it will cause the density function to turn from concave to convex at the $\Gamma = 0$ point.

Figures 2.20a and 2.20b show how the speed of sound changes in the ideal gas and the BZT gas cases, respectively. In the ideal-gas case, the speed of sound is a function of temperature

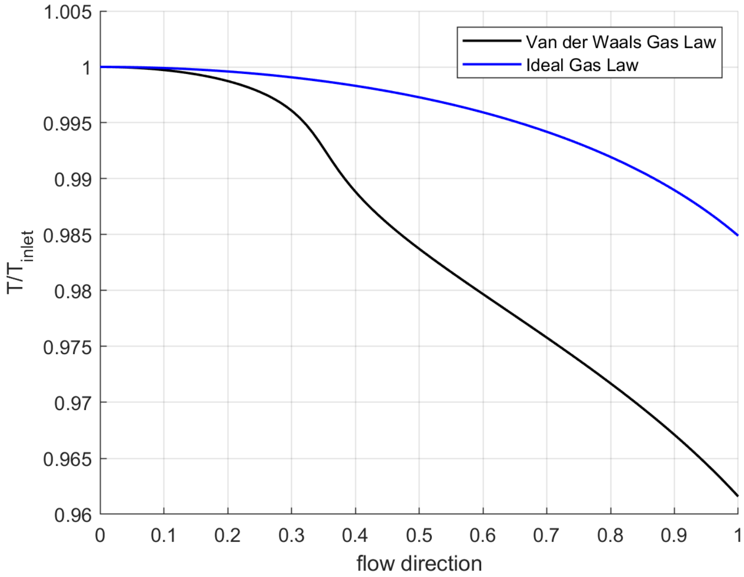

Figure 2.18: Variation of temperature ratio along the channel for Case 1

only and thus decreases with decreasing pressure monotonically as shown in figure 2.20a. Equation (2.9) gives the dependence of sound speed on the pressure in an isentropic process as

$$\left(\frac{\partial c}{\partial p}\right)_s = \frac{v}{c}(\Gamma - 1)$$

which shows that the sound speed decrease as pressure decreases for $\Gamma > 1$. For a non-conventional gas flow when Γ goes below 1, the speed of sound decreases with increasing pressure, which is opposite to the classical theory. Such is the situation demonstrated in figure 2.20b.

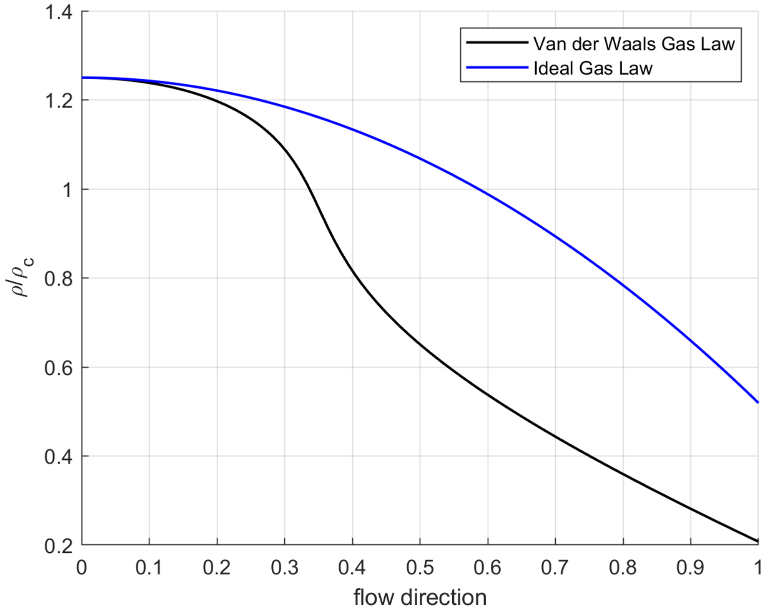

Figure 2.19: Variation of density along the channel for Case 1

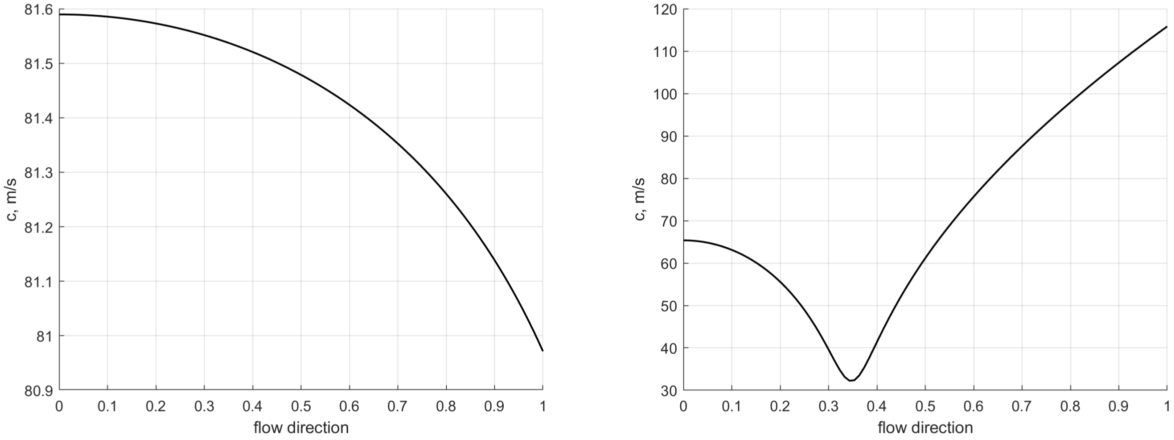

(a) Ideal Gas Model

(b) Van der Waals Gas Model

Figure 2.20: Variation of sound speed along the channel for Case 1

Figure 2.21 shows the velocity distribution in the nozzle. The velocity increases monotonically along the channel for both the Van der Waals gas and the ideal gas, but the net velocity increase is higher for the real gas than for the ideal gas consistent with the analysis on the higher temperature drop presented earlier. Essentially, the real gas incurs a higher pressure rise as the gas is compressed due to the increased inter-molecular repulsion force, resulting in extra external work needed to compress the gas. In the expansion process, this extra energy stored as internal energy is then released and converted to the additional kinetic energy of the flow.

Also to be noticed is that, although the flow Mach number may decrease in part of the expansion process when Γ becomes less than 1.0 as shown in figure 2.23b, the flow velocity and thus the kinetic energy monotonically increase with decreasing pressure as shown in figure 2.21b. The temperature of the gas decreases in the expansion process (see figure 2.17b) as the fluid converts part of its internal energy into its kinetic energy.

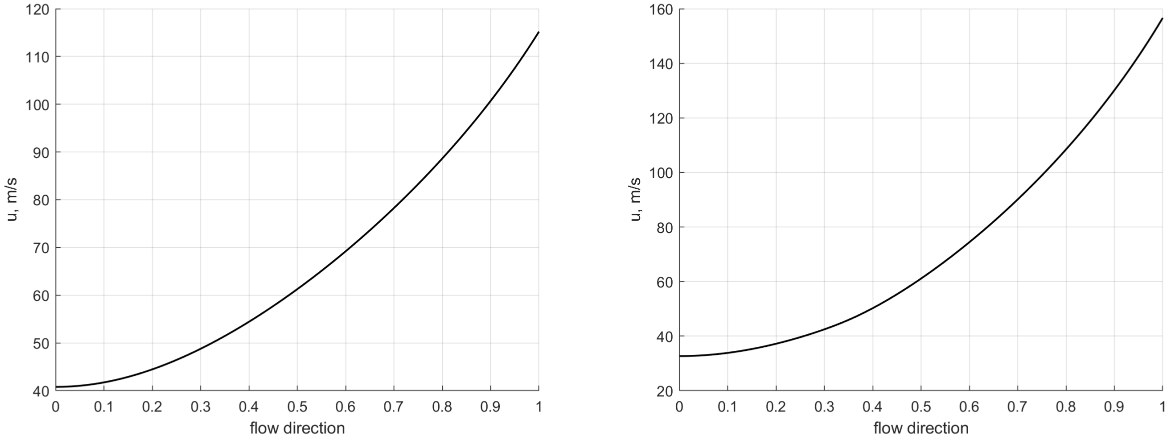

(a) Ideal Gas Model

(b) Van der Waals Gas Model

Figure 2.21: Variation of velocity along the channel for Case 1

Figures 2.22a and 2.22b present the difference between the cross-sectional area ratio by using the ideal-gas law and the Van der Waals model, while Figures 2.23a and 2.23b give the Mach number comparison. Figures 2.22a and 2.23a show that a convergent-divergent nozzle is needed for transonic flow for an ideal gas: in other words, the nozzle needs a 'throat' to achieve the sonic condition. Mach number is a monotonic function of velocity only. On the contrary, the story for a BZT gas is very different. The Mach number may no longer be a monotonic function of velocity in the supersonic regime. Recall Equation (2.67)

$$\frac{du}{u} = \frac{1}{1 + (\Gamma - 1)M^2} \frac{dM}{M}$$

This equation states that the Mach number increases monotonically with u when $\Gamma > 1$ and increases with u only for $M^2 < \dfrac{1}{1 - \Gamma}$ when $\Gamma < 1$. Figure 2.23b clearly shows that there is an area where the Mach number is decreasing with increasing velocity, around $p_r = 0.9$ to $p_r = 1.02$. Within this range, the fundamental derivative is decreasing rapidly while the Mach number doesn't change too much, so M^2 is larger than $\dfrac{1}{1 - \Gamma}$.

Recall Equation (2.72) below

$$\left(\frac{dM}{dx}\right)^2 = \frac{\Gamma}{2A} \frac{d^2 A}{dx^2}$$

which relates the curvature of the cross-sectional area change to $\dfrac{dM}{dx}$ for different Γ at $M = 1$. For a conventional gas where $\Gamma > 0$, a converging-diverging throat is needed for the flow to either accelerate from subsonic to supersonic or decelerate from the supersonic to subsonic flow. This is shown in Figures 2.22a and 2.22b. For the real-gas case, Γ varies and may go into regions where $\Gamma < 0$. Three sonic points are identified in Figures 2.22b and 2.23b. The first and third happen in regions $\Gamma > 0$ which leads to the classical convergent-divergent requirement for the nozzle shape. The second sonic point in the middle is the interesting one. At this point, Γ is smaller than 0. According to Equation (2.72), a divergent-convergent part will be needed. In Figure 2.22b at around $p_r = 0.95$, it is clearly shown that the second sonic point is at a local maximum point of the nozzle cross-sectional area.

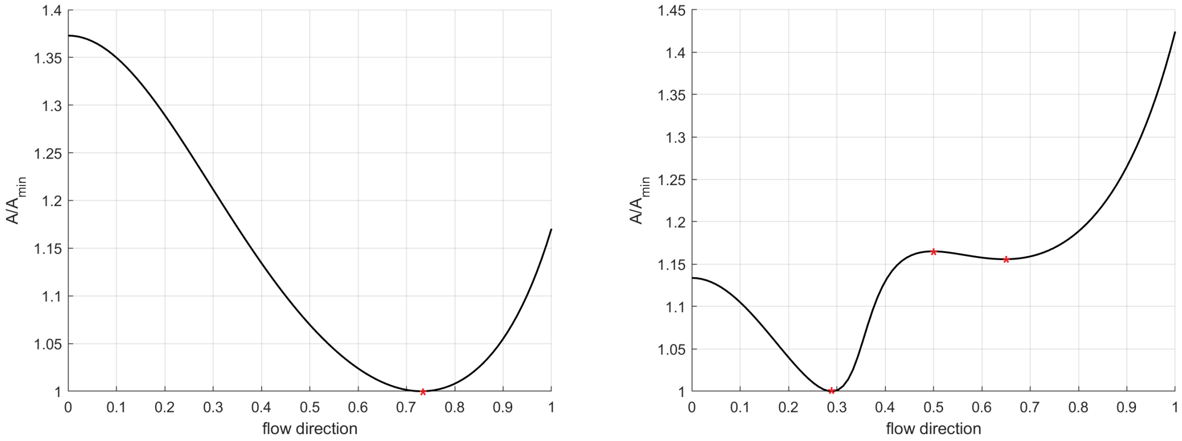

(a) Ideal Gas Model

(b) Van der Waals Gas Model

Figure 2.22: Variation of cross-sectional area ratio along the channel for Case 1

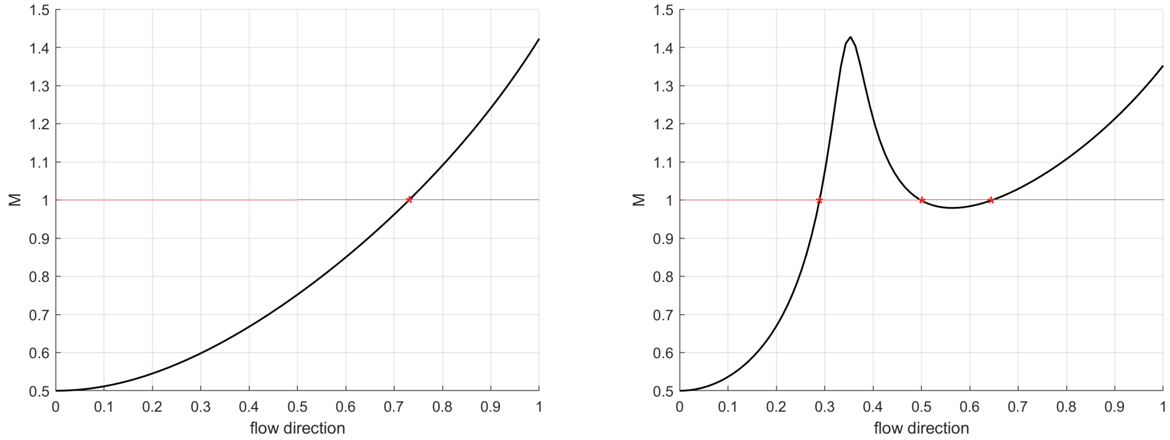

(a) Ideal Gas Model

(b) Van der Waals Gas Model

Figure 2.23: Variation of Mach number along the channel for Case 1

2.3.3 Isentropic Flow with Supersonic Inlet Condition

We consider in this section the same upstream thermal conditions and pressure drop profile as in the previous case but a supersonic inlet Mach number of 3. The gas is expanded more than the subsonic case until $p = 0.1p_c$. The variables along the channel of the static thermodynamic properties such as Γ, temperature, density, and sound speed are the same as in the previous case for the same specified pressure drop profile in an isentropic expansion. The flow properties such as Mach number (Figure 2.24a), cross-sectional area (Figure 2.24b), flow velocity (Figure 2.24c), and speed of sound (Figure 2.24d) behave very differently compared to the subsonic inlet flow case.

Compared with the subsonic inlet flow case, there is no transonic flow in the supersonic case. Although the Mach number is not a monotonic function of velocity in the unconventional regime and the Mach number at some location in the channel is smaller than the inlet Mach number, the computations show that the supersonic flow with this high inlet Mach number remains supersonic throughout of the expansion process. As stated above, when $\Gamma < 1$, the Mach number decreases with velocity for $M^2 > \dfrac{1}{1-\Gamma}$. Initially, as the flow starts in the normal $\Gamma > 1$ region, the Mach number increases as is the same behavior for the ideal gas albeit it seems to increase even faster than the ideal gas. However, very soon after it enters into the $\Gamma < 1$ range, the Mach number starts to decrease because of the "abnormal" increase of sound speed with decreasing pressure for the BZT gas. This decreasing trend is eventually reversed at very low pressure because of the increased rate of rising for velocity.

In the supersonic inlet flow case, the main differences between the Van der Waals model results and the ideal-gas results are given below.

- The Mach number is no longer a monotonic function and it changes a lot along the nozzle. When the isentrope is still in the conventional regime, the Mach number increases faster than the ideal-gas case and becomes larger than 6 due to the rapid decrease in the sound speed. Once the isentrope enters the negative fundamental derivative area, the Mach number decreases rapidly and later turns to increase again but keeps smaller than the Mach number from the ideal-gas law.

- Much larger cross-sectional area ratio is needed to achieve the same pressure drop in quasi-1D flow. Here at the outlet of the nozzle, the area ratio is about two times the ideal-gas result.

- During the expanding process (pressure decreasing), the variation of sound speed is non-monotonic. It may increase as the fluid enters into the non-conventional $\Gamma < 1$ regime. On the other hand, flow velocity continues monotonically increasing as pressure decreases and at a faster rate than for an ideal gas.

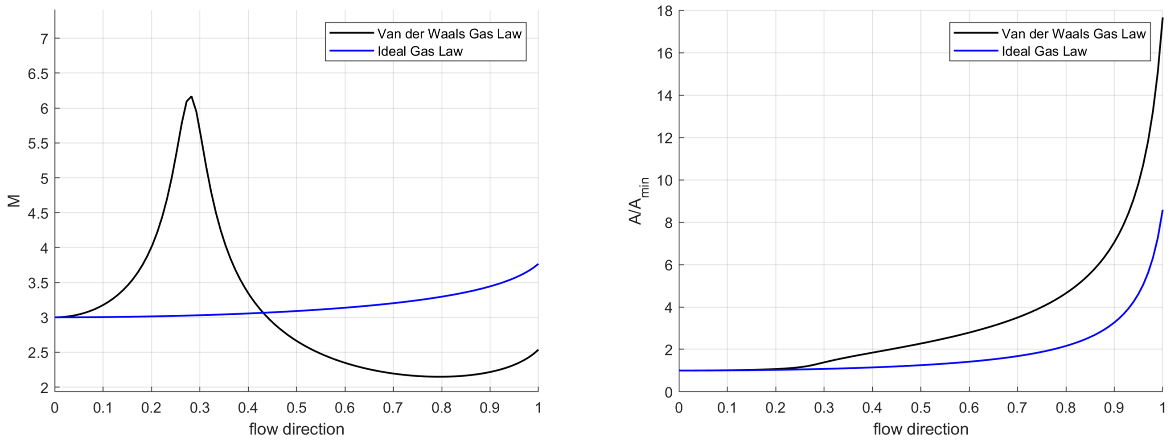

(a) Mach number (b) Cross-sectional area ratio

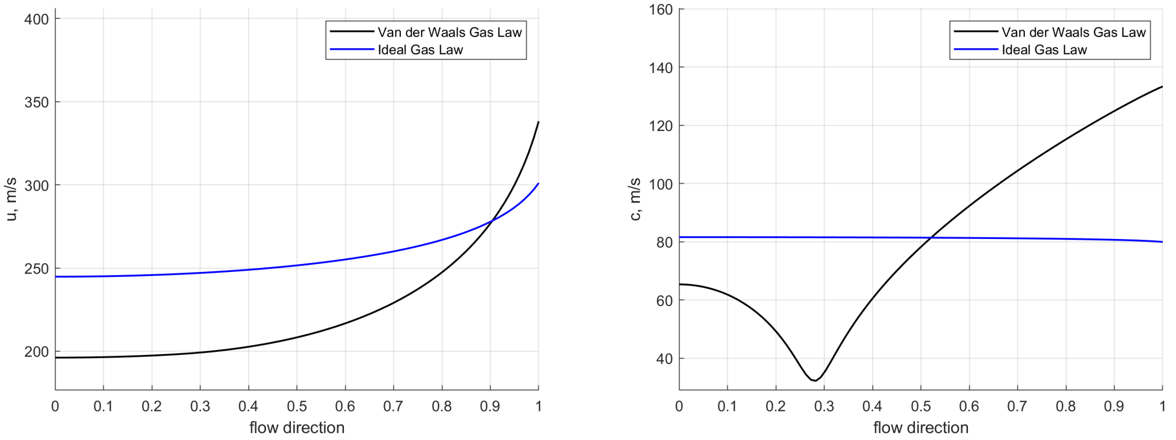

(c) Velocity (d) Sound Speed

Figure 2.24: Variation of flow variables along the channel for Case 2

Chapter 3

Unconventional Wave Phenomena

In the last several decades, many efforts have been made to demonstrate the presence of BZT gas and to theorize the nonclassical wave phenomena in this area [14][22][45][110]. In most flows, shock waves and expansion fans are typical wave phenomena. Using the Van der Waals model for MDM fluid (octamethyltrisiloxane, $C_8H_{24}O_2Si_3$), this chapter investigates the generation of expansion shock waves and the Prandtl-Meyer relation for nonclassical gases. Results indicate that, with an incoming flow in the nonclassical area, there exists a critical Mach number beyond which an expansion shock cannot occur, and there is a correlation between the critical Mach number and the size of the nonclassical area. Through a single expansion shock, a fluid may transition from a nonclassical region to a classical region. In an attempt to experimentally demonstrate the presence of expansion shocks, such data may help to determine flow conditions for experimental set-up.

3.1 Expansion Shock Wave

Shock waves are usually treated as discontinuities which will cause sudden changes in the flow variables. Figure 3.1 depicts the formation of a shock wave in an ideal gas. Consider the initial wave of a pressure pulse traveling in the positive x direction into a stationary gas with properties c_0, p_0, as shown in Figure 3.1a. Along the left-running characteristic C^- from the stationary uniform region ahead of the wave, the Riemann invariant J^- remains constant

$$u - \frac{2}{\gamma - 1}c = -\frac{2}{\gamma - 1}c_0 \tag{3.1}$$

which gives

$$u = \frac{2}{\gamma - 1}(c - c_0) \tag{3.2}$$

Any point on the wave advances with constant wave speed represented by the right-running characteristic C^+

$$u + c = \frac{\gamma + 1}{\gamma - 1}c - \frac{2}{\gamma - 1}c_0 \tag{3.3}$$

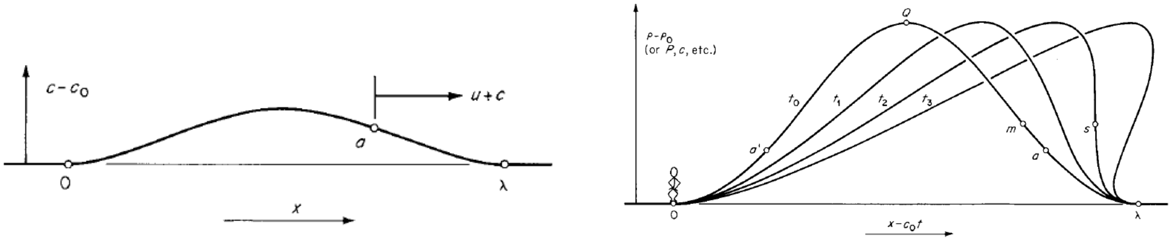

(a) Initial wave shape

(b) Wave distortion at different time instance

Figure 3.1: Shock wave formation for ideal gas[2]

The monotonic increase of wave speed with the pressure increase for an ideal gas will start to distort the wave shape. Within time Δt, the distance change between any point on the wave and the head of the wave, which travels at constant speed c_0, is

$$(u + c - c_0)\Delta t = \frac{\gamma + 1}{\gamma - 1}(c - c_0)\Delta t \tag{3.4}$$

As depicted in Figure 3.1b, the wave starts to distort at time $t = t_1$, manifesting as a steepening of the compressive portion and spreading of the expansive portion. Eventually at $t = t_2$ (the instant of shock formation), a portion s of the leading edge of the wavefront becomes vertical. The point behind overtakes the point ahead.

The C^+ characteristics will not be parallel on a pressure disturbance. They will either converge or diverge, generating a shock or a continuous rarefaction fan. The differential form of the Riemann invariant on C^- is given as

$$du - \frac{dp}{\rho c} = 0 \tag{3.5}$$

The change of $u + c$ can be expressed as

$$d(u + c) = du + dc = \frac{dp}{\rho c} + dc \tag{3.6}$$

For isentropic flow, we have from Equation 2.9

$$\frac{dp}{\rho c} = c\frac{d\rho}{\rho} = \frac{dc}{\Gamma - 1} \tag{3.7}$$

Substituting the above into Equation 3.6 yields

$$d(u + c) = \Gamma \frac{dp}{\rho c} \tag{3.8}$$

Evidently, when $\Gamma > 0$, the sign of $d(u + c)$ is the same as the sign of pressure difference, referring to the conventional compression shock. When $\Gamma = 0$, $d(u + c) = 0$ and the wave will stay undistorted. When $\Gamma < 1$ the pressure increase in the pressure pulse in Figure 3.1a causes a decrease in sound speed. When Γ reaches 0, the reduction in sound speed due to

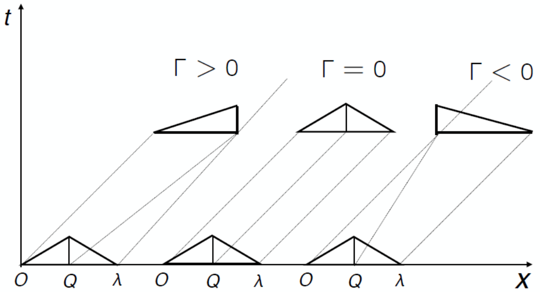

Figure 3.2: Behavior of the wave for various values of the fundamental derivatives Γ

pressure rises exactly cancels the flow velocity increases across the right-running wave. As the gas enters into the $\Gamma < 0$ regime, this reduction in sound speed over-powers the increase of u, resulting in the peculiar nonclassical behavior of compressive isentropic waves instead of the conventional compression shock. On the contrary, if the flow is subject to a negative pressure pulse in the $\Gamma < 0$ regime, the wave speed will increase with pressure decrease, resulting in a steepening of the expansive portion of the wave to generate an expansion shock. Rarefaction shocks are inadmissible in conventional gas dynamics owing to the violation of the second law of thermodynamics. Thompson[2] converted the Rankine-Hugoniot equation into a relation between Δs and Δp by expanding $h(s,p)$ and $v(s,p)$ in Taylor series and retaining terms up to the third order, which results in

$$\Delta s = \frac{1}{12T_1}\left(\frac{\partial^2 v}{\partial p^2}\right)_s (\Delta p)^3 + O(\Delta p)^4 \tag{3.9}$$

which could be expressed in terms of Γ:

$$\Delta s = \frac{v_1^3\Gamma}{6T_1c_1^4}(\Delta p)^3 + O(\Delta p)^4 \tag{3.10}$$

It shows that with $\Gamma < 0$, the second law of thermodynamics can be satisfied with a decrease of pressure across an expansion shock wave. This conclusion pertains only to weak shock scenarios due to the exclusion of higher-order terms in the derivation. As the value of pressure difference Δp increases, the validity of this assertion may come into question, potentially leading to a contravention of the second law of thermodynamics. A compilation of case studied, each either adhering to or contravening the entropy condition, will be provided in Table 3.1. Computation results underline the fact that as Δp increases, the admissibility of expansion shock waves diminishes commensurately.

3.1.1 Conservation Equations for Normal Shock Wave

The above analysis demonstrates the presence of expansion shock waves for gases with $\Gamma < 0$. A set of example cases for the Van der Waals model of fluid MDM is examined. Recall the integral conservation equations of one-dimensional, frictionless, adiabatic flow for continuity,

$$\rho_1 u_1 = \rho_2 u_2 \tag{3.11}$$

momentum

$$p_1 + \rho_1 u_1 = p_2 + \rho_2 u_2 \tag{3.12}$$

and energy

$$h_1 + \frac{1}{2}u_1^2 = h_2 + \frac{1}{2}u_2^2 \tag{3.13}$$

Unlike the ideal-gas analysis, here the relations between upstream (pre-shock) and downstream (post-shock) variables are highly nonlinear and therefore it is difficult to derive an analytical solution. Iterative methods are used to determine the flow variables after shock waves.

3.1.2 Normal Shock Relations of a BZT Gas

Same to the conventional theories for an ideal gas, the conservation laws are applied to evaluate the normal shock wave relation. Here, a pre-shock point located within the $\Gamma < 0$ area has been chosen, as marked by the $*$ in Figure 3.3. The pre-shock condition is given as $\frac{p}{p_c} = 1, \frac{v}{v_c} = 1.1$ and Mach number varies from 1 to 3. Both the compression shock family and the expansion shock family are calculated and the results that violate the second law of thermodynamics are eliminated. Figure 3.3 shows that there are two branches starting from this pre-shock condition; one is the compression shock family and the other one is the expansion shock family. The branch on the right-hand side is the interesting one to us.

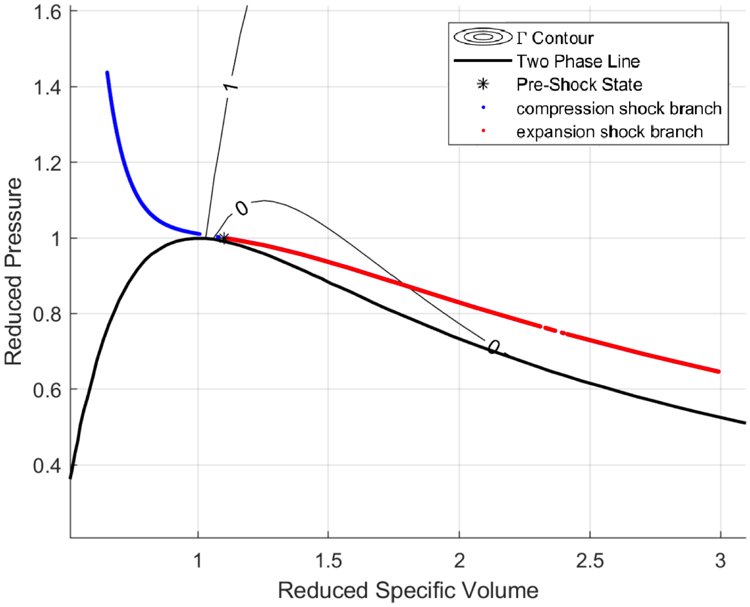

Figure 3.3: Normal shock relation: p-v diagram

Figure 3.4 presents the corresponding post-shock Mach number and the fundamental derivative Γ at each point. A reference case of ideal-gas flow ($\gamma = c_p/c_v = 1.0173$) is plotted on the same figure for comparison. The Mach number ratio of the compression shock family (lower branch) is similar to the conventional theory, whereas the expansion shock family (upper branch) has cases with post-shock Mach numbers greater than 1. In other words, for those shock waves, both the pre-shock and the post-shock flow are supersonic.

The post-shock fundamental derivatives of the compression shock family (blue line in Figures 3.3 and 3.4) jump into the $\Gamma > 1$ classical gas area, while those of the expansion shock family (red line) stay in the $\Gamma < 1$ nonclassical area. Notice that the pre-shock Γ is smaller than zero. It means that the expansion shock waves can only be captured in the nonclassical range because both pre-shock and post-shock flow of these expansion shock waves need to follow the nonclassical gas theories derived in previous studies[111][112].

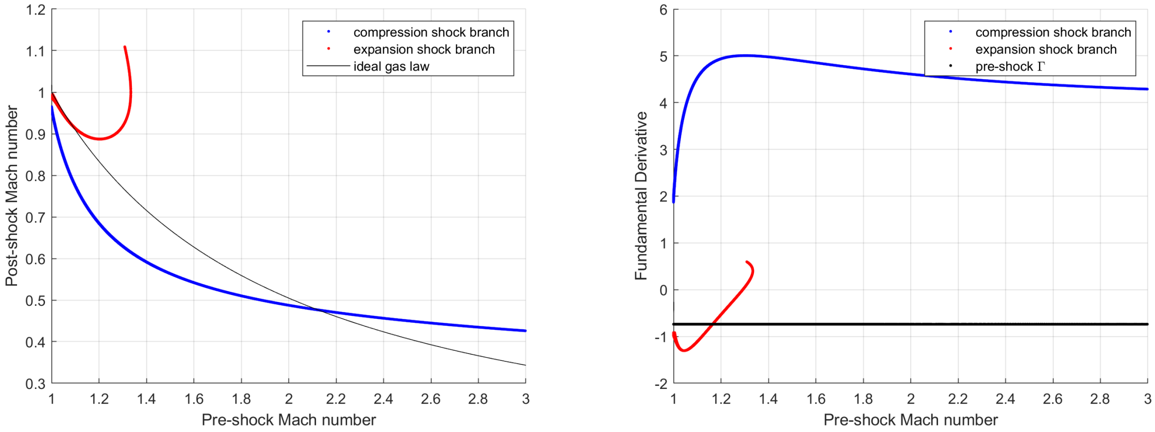

(a) M_1 vs M_2

(b) Fundamental derivative

Figure 3.4: Normal shock relation: Post-shock variables

Figure 3.5 plots the ratios of static and total flow properties across the shock waves as functions of pre-shock Mach number. In contrast with the normal shock wave relations from conventional gas, some conclusions are given below.

- The static pressure ratio and static density ratio are significantly smaller than the ideal-gas case, for both the compression shock family and expansion shock family.
- The static temperature ratio is smaller but not that much, compared with the static pressure ratio and static density ratio.
- The expansion shock family shows completely opposite behavior to the classical theory. All the static variables are decreasing after the shock wave.

- The total pressure drop is much smaller than conventional theory results, which means less kinetic energy is lost for nonclassical gas cases.

- Different from the classical theory, total temperature becomes a function of the thermodynamic states of the gas instead of a constant. The total temperature here is decreasing after the shock wave, not too much but it still cannot be neglected. Notice that the total enthalpy is not changing across the shock wave because this process is adiabatic.

- For certain pre-shock Mach numbers M_1, multiple post-shock Mach number values can be derived. While one solution for the compressible shock leaps into the region where $\Gamma > 1$, two solutions persist for the expansion shock branch - one is subsonic, and the other is supersonic. Both solutions are permissible. The resulting output, whether it's the subsonic or supersonic solution, depends on the specific downstream conditions.

3.1.3 Sample Cases with Normal Shock

In addition to the general perspective of the normal shock wave relation of nonclassical gas flow, some representative cases are selected to illustrate the specific features of expansion shock waves. All of the pre-shock conditions are in the $\Gamma < 0$ dome, while the post-shock solutions either remain within the nonclassical area or jump to the classical region. As was previously stated, there exists a critical Mach number above which the expansion shock waves are inadmissible. Despite the absence of an analytical expression for the critical Mach number, it is evident from the results that there is an association between the critical Mach number and the pre-shock conditions. All the outcomes that comply with conservation laws are recorded in Table 3.1 and plotted in Figure 3.6. Some of the results may be in violation of the second law of thermodynamics (entropy change $ds < 0$) and are thus eliminated from further analysis.

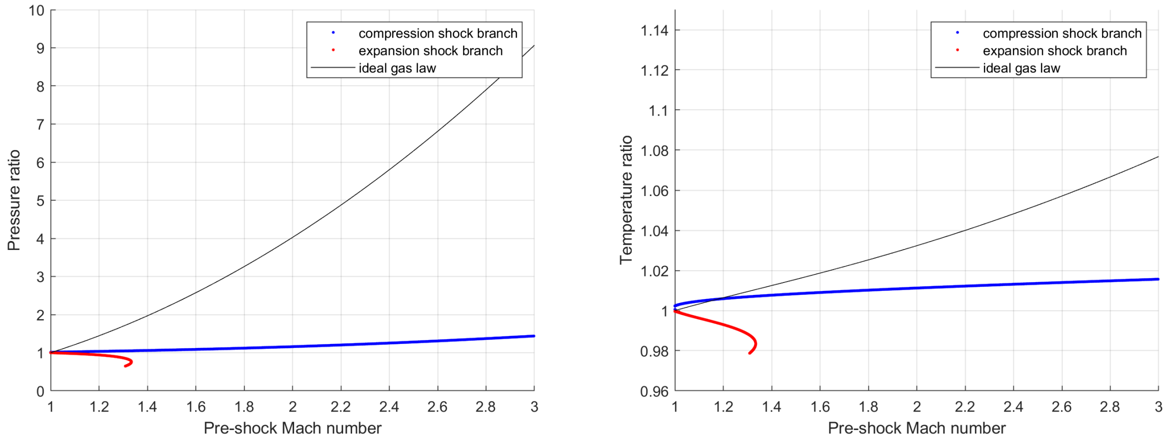

(a) Pressure (b) Temperature

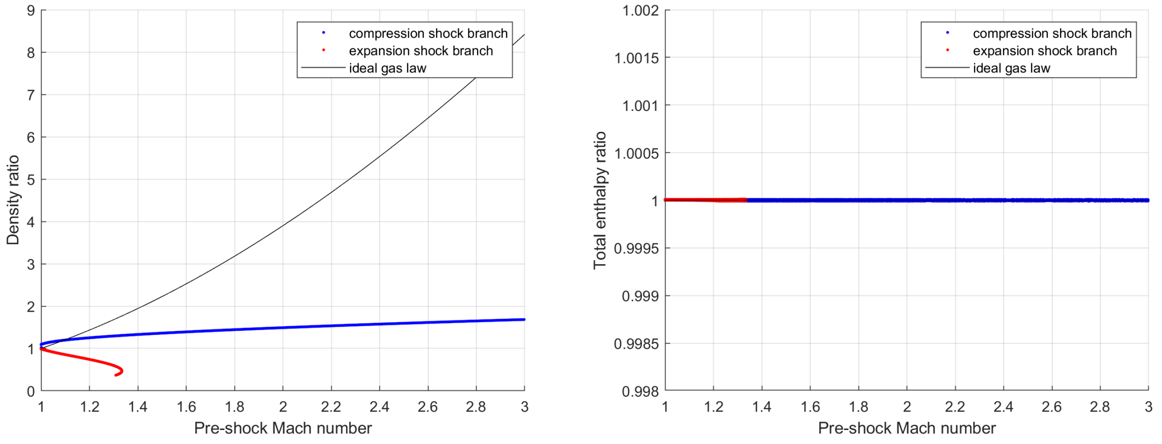

(c) Density (d) Total enthalpy

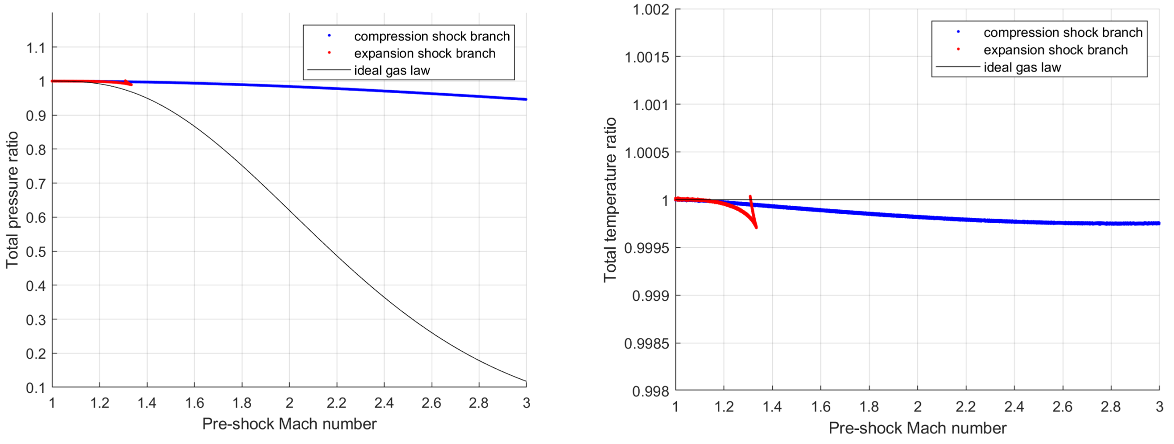

(e) Total pressure (f) Total temperature

Figure 3.5: Normal shock relation: Post-shock variables

Figure 3.6a and Figure 3.6b illustrate the solutions of pre-shock condition $p = p_c, v = 1.1v_c$, for $M = 1.35$ and $M = 1.47$, respectively. There are three potential solutions with a pre-shock Mach number of 1.35, but one of them violates the entropy criterion. The two admissible post-shock solutions are not far from the pre-shock point position. One of them remains inside the $\Gamma < 0$ dome and the other one falls into the $\Gamma > 1$ region. With a pre-shock Mach number of 1.47, there is only one solution that leads to a compression shock wave, indicating that the critical Mach number for this pre-shock condition is some value between these two cases.

Figure 3.6c to Figure 3.6f illustrate the solutions for two more pre-shock conditions: $p = p_c, v = 1.2v_c$, and $p = p_c, v = 1.3v_c$. Results reveal that when the pre-shock point shifts away from the critical point, the critical Mach number for developing an expansion shock wave decreases; therefore, there is less possibility for those pre-shock points to get an expansion solution. Another observation is that the expansion shock solution may cross the $\Gamma = 0$ boundary, as illustrated in Figure 3.6c. If the pre-shock Mach number stays unchanged and the pre-shock point moves away from the critical point, the admissible post-shock solutions will also move further from the pre-shock point, indicating an increase in shock strength.

Table 3.1: Normal shock solution of different pre-shock condition

Pre-shock			Post-shock			ds
M_1	p_{r1}	v_{r1}	M_2	p_{r2}	v_{r2}	
1.3500	1.0000	1.1000	0.5837	1.0423	0.8373	> 0
1.3500	1.0000	1.1000	0.8753	0.9159	1.6224	> 0
1.3500	1.0000	1.1000	1.2793	0.5121	4.1313	< 0
1.4700	1.0000	1.1000	0.5514	1.0543	0.8153	> 0
1.2200	1.0000	1.2000	0.5272	1.0757	0.8113	> 0
1.2200	1.0000	1.2000	0.9394	0.8774	1.8292	> 0
1.2200	1.0000	1.2000	1.0985	0.6759	2.8636	< 0
1.2500	1.0000	1.2000	0.5168	1.0810	0.8042	> 0
1.0900	1.0000	1.3000	0.5423	1.1013	0.8172	> 0
1.0900	1.0000	1.3000	0.9611	0.9152	1.7043	> 0
1.0900	1.0000	1.3000	1.0778	0.7239	2.6166	< 0
1.1100	1.0000	1.3000	0.5298	1.1065	0.8101	> 0

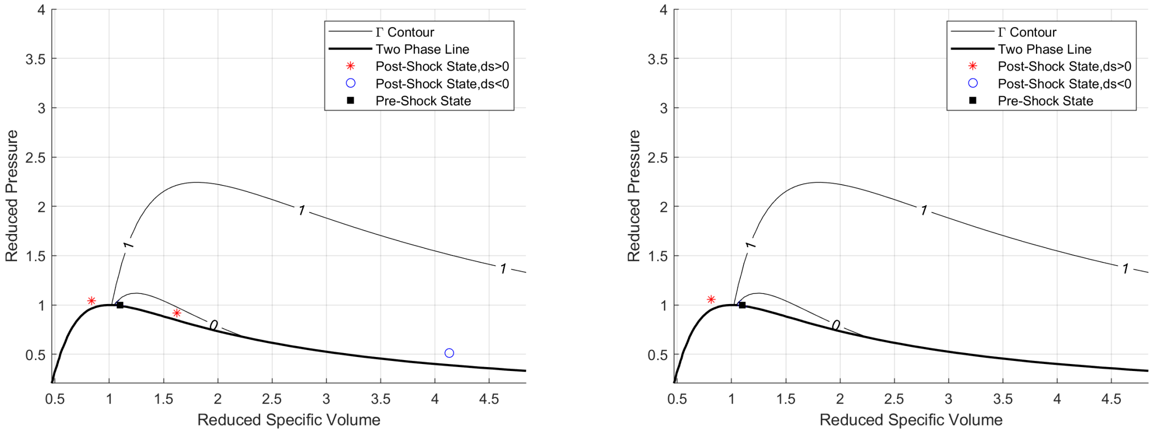

(a) Pre-shock: $p_r = 1, v_r = 1.1, M_1 = 1.35$ (b) Pre-shock: $p_r = 1, v_r = 1.1, M_1 = 1.47$

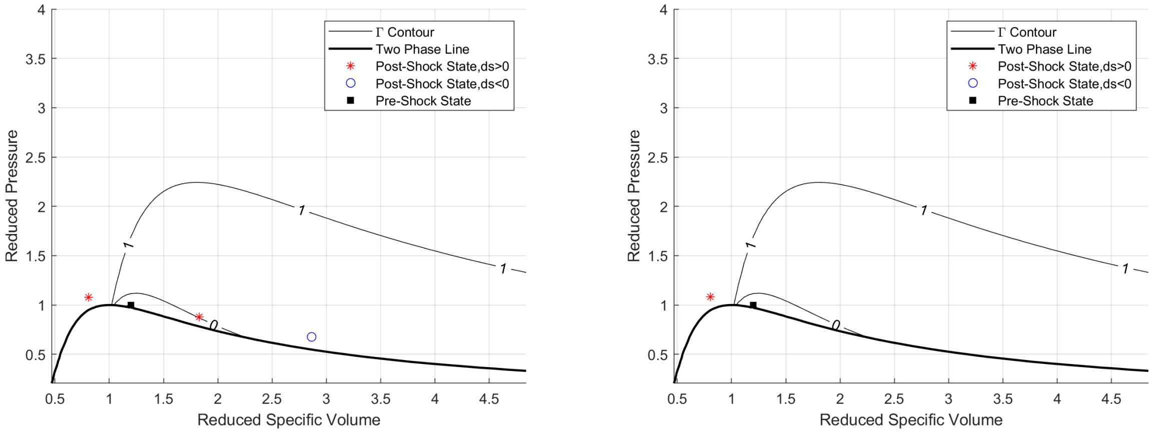

(c) Pre-shock: $p_r = 1, v_r = 1.2, M_1 = 1.22$ (d) Pre-shock: $p_r = 1, v_r = 1.2, M_1 = 1.25$

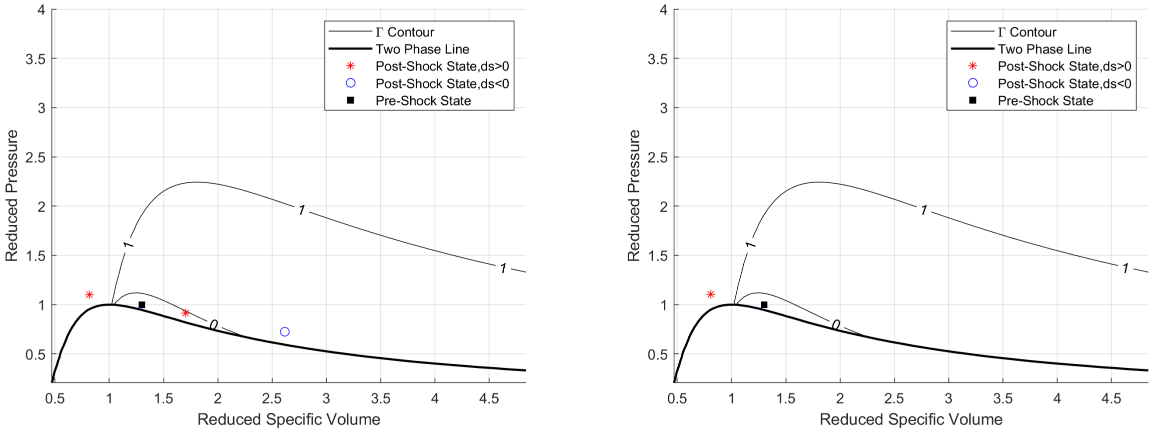

(e) Pre-shock: $p_r = 1, v_r = 1.3, M_1 = 1.09$ (f) Pre-shock: $p_r = 1, v_r = 1.3, M_1 = 1.11$

Figure 3.6: Normal shock solution of different pre-shock conditions

3.2 Compression Fan

In classical gas dynamics, when a supersonic flow goes around a convex corner or a piston abruptly withdraws in the opposite direction, an expansion fan consisting of an unlimited number of expansion waves will be generated. It is referred to as the Prandtl-Meyer expansion fan. The Prandtl-Meyer function is essential for the comprehension of many steady isentropic flows. In the case of a perfect gas, the Prandtl-Meyer function can be expressed using a simple and explicit formula. However, for real-gas cases, specifically in Organic Rankine Cycles, nonclassical gas effects must be taken into consideration and the fluid is operated in a region where expansion shock and compression fan may occur. Let us first recall the Riemann invariants and consider the flow undergoing a small deflection angle $d\theta$ which changes the velocity by dV

$$d\theta = \pm\sqrt{M^2 - 1}\frac{dV}{V} \tag{3.14}$$

where M is Mach number and V is the fluid velocity. This equation is applicable to any gas model. For an ideal gas, it can be directly integrated into

$$\theta_2 - \theta_1 = \nu(M_1) - \nu_(M_2) \tag{3.15}$$

where ν is the Prandtl-Meyer function

$$\nu(M) = \sqrt{\frac{\gamma+1}{\gamma-1}}tan^{-1}\sqrt{\frac{\gamma-1}{\gamma+1}(M^2-1)} - tan^{-1}\sqrt{M^2-1} \tag{3.16}$$

For the Van der Waals equation of state, we have

$$\begin{aligned} p_2 &= \frac{RT_2}{v_2 - b} - \frac{a}{v_2^2} \\ s_2 - s_1 &= c_v ln\left(\frac{T_2}{T_1}\right) + Rln\left(\frac{v_2 - b}{v_1 - b}\right) \\ H_2 &= c_v T_2 - \frac{a}{v_2} + p_2 v_2 = H_0 - \frac{1}{2}V_2^2 \end{aligned} \tag{3.17}$$

Differentiate equation 3.17 to get

$$ds = \frac{c_v}{T}dT + \frac{R}{v - b}dv \tag{3.18}$$

$$dH_0 = \left(c_v + \frac{Rv}{v - b}\right)dT + \left[\frac{2a}{v^2} - \frac{RTb}{(v - b)^2}\right]dv + VdV \tag{3.19}$$

Entropy and total enthalpy change are both zero for an isentropic process. Given a change in velocity, Equations (3.18) and (3.19) can be used to determine the change in temperature and specific volume. Thus, the Prandtl-Meyer relation can be obtained by numerical integration.

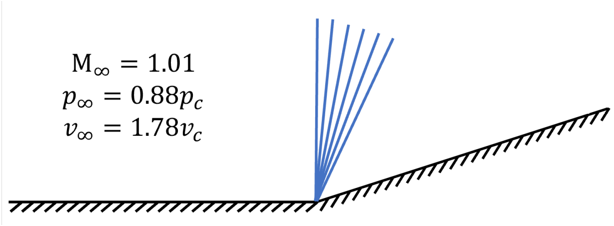

Figure 3.7: Sketch of compression fan

Consider an example of a compression fan in the nonclassical $\Gamma < 0$ region, as shown in Figure 3.7. The wedge has a compressive angle of 10.7 degrees. The upstream flow has a Mach number of 1.01 and is located in the $\Gamma < 0$ region with pressure $p_\infty = 0.88p_c$, specific volume $v_\infty = 1.78v_c$ and flow angle $\theta = 0^o$. The flow is going through a compressive process and ends at $p_\infty = 1.01p_c$ and turning angle $\theta = -10.7^o$ ($d\theta > 0$ for expansion waves and $d\theta < 0$ for compression waves). As the incoming flow is in the nonclassical region where compression fans are admissible, a Prandtl-Meyer compression fan is centered at the corner. The compression process is isentropic. Figure 3.8 depicts the isentrope on the p-v diagram, the variation of flow turning angle and the fundamental derivative with regard to Mach number, and the variation of sound speed and velocity with regard to pressure. In contrast to the classical gas dynamics phenomenon, this example exhibits the exact opposite behavior. The sound speed decreases as pressure increases, resulting in an increase in Mach number when the sound speed decreases faster than the decreasing rate of flow velocity. Therefore, the Mach number increases along the compression process. Despite the increase in Mach number, the flow velocity decreases and the pressure rises across the compression fan.

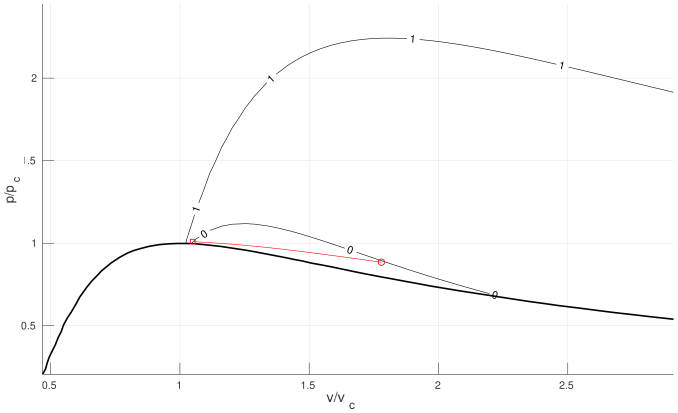

(a) p-v diagram

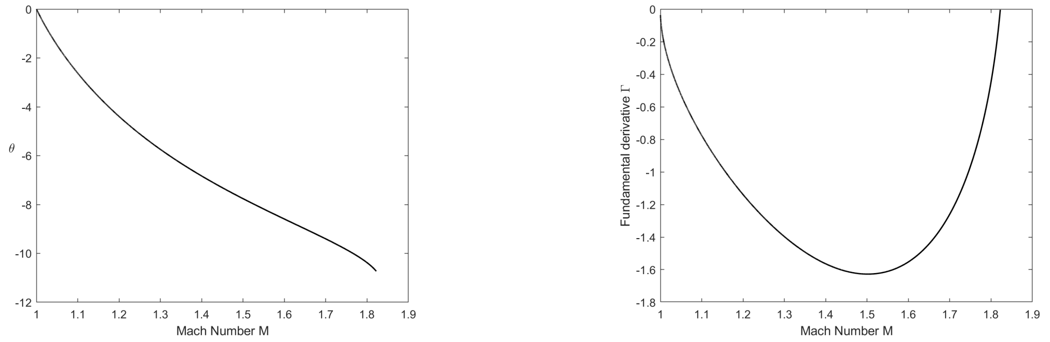

(b) Turning angle vs. Mach number

(c) Fundamental derivative vs. Mach number

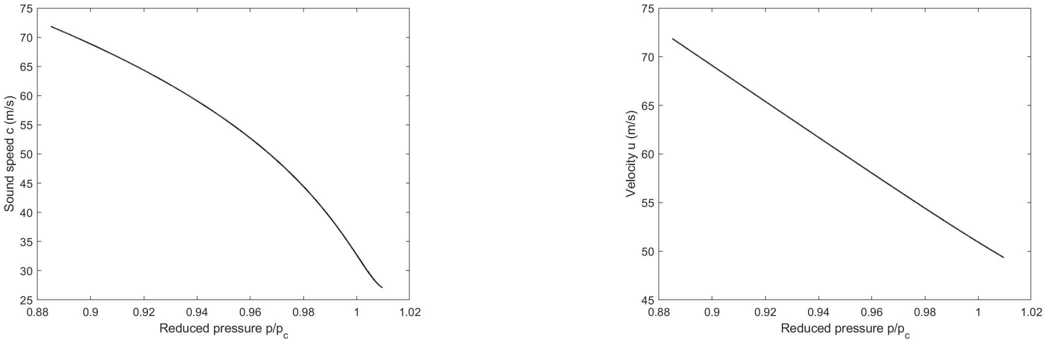

(d) Speed of sound vs. Pressure

(e) Velocity vs. Pressure

Figure 3.8: Compression fan

Chapter 4

Machine Learning Algorithm for Predicting Thermodynamic Properties of Dense Gases

The precise prediction of thermodynamic properties in dense gases constitutes a formidable task, one that holds crucial implications for numerous domains, including but not limited to material science, chemical engineering, and astrophysics. Owing to the complexity of the underlying molecular interactions and configurations, the development of a reliable equation of state for largely non-ideal or multi-component fluid systems is a challenging endeavor. In this context, the application of machine learning techniques presents a viable solution for advancing the prediction of thermodynamic properties. Specifically, these techniques offer the potential to directly learn the underlying thermodynamic mappings from existing data, thereby circumventing the need for conventional equations of state. Consequently, this innovative approach holds significant promise for improving the precision and accuracy of thermodynamic property predictions in a diverse range of complex systems.

4.1 Introduction

The utilization of machine learning techniques has exhibited a swift expansion in both academic investigation and practical implementation across various engineering domains. Machine learning has emerged as a powerful tool for predicting the behavior of complex systems, and has been applied to the prediction of the physical properties of substances with promising results. Recent examples of successful applications of machine learning in materials research include accurate and rapid predictions of phase diagrams[113], crystal structures[114][115], and material properties (using historical data)[116][117]. Despite the promise of machine learning methods in generating mappings among the thermodynamic parameters of materials, little attention has been paid to exploring the thermodynamic properties of pure fluids and their mixtures over a broad range of temperatures using machine learning-based approaches. Nevertheless, the fact that machine learning-based methods are data-driven and can potentially generate mappings without relying on any specific physical expressions or underlying physical insights is an attractive prospect. Achieving this goal would provide a novel means of swiftly investigating the thermodynamic properties of new or complex compounds.

In thermodynamic analysis and applications, the ability to develop predictive models and identify patterns in physical property data has the potential to accelerate the generation and development of tables of the thermodynamic properties of certain fluids. The thermodynamic properties of gases, such as enthalpy, entropy, and specific heat, are essential for comprehending the behavior of gases under different conditions. Understanding the different types of machine learning algorithms and their applications can help researchers and engineers in the physical sciences and engineering fields identify appropriate methods and tools for their specific needs. Machine learning algorithms can be classified into two main categories: supervised and unsupervised. Both types of algorithms employ a set of observations referred to as training data, but they differ in terms of the nature of the training data and the objectives of the algorithm. Supervised learning algorithms can be trained on a dataset of input-output pairs consisting of gas compositions and their corresponding thermodynamic properties. The input can include parameters such as temperature, pressure, and mole fractions of the constituents, while the output can include properties such as enthalpy, entropy, and specific heat. The trained algorithm can then be used to predict the thermodynamic properties of gases for new compositions and conditions. The accuracy of the predictions depends on the quality and size of the training dataset, as well as the choice of algorithm and model architecture. Various types of supervised learning algorithms, such as neural networks, decision trees, and support vector machines, have been applied to predict the thermodynamic properties of materials with varying degrees of success. In addition to supervised learning, unsupervised learning algorithms can also be used to identify patterns and correlations in the thermodynamic data of gases. Clustering algorithms, for example, can be used to group gases based on their thermodynamic properties and similarities, which can provide valuable insights into the underlying physics and chemistry of gas mixtures. Overall, the use of machine learning algorithms in the prediction of the thermodynamic properties of gases offers a powerful and efficient tool for modeling and predicting the behavior of gases in a wide range of industrial and scientific applications.

4.2 Artificial Neural Network (ANN)

The utilization of machine learning as a correlation tool in the field of thermodynamics has been a topic of discussion for some time. However, with the recent advancements in hardware and software, this field is undergoing a significant revival[118]. Among the various machine learning techniques, artificial neural networks have garnered significant attention due to their relative ease of deployment and their capacity to recognize complex patterns and relationships in data[119]. Artificial neural networks (ANNs) are computational models that draw inspiration from the structure and function of biological neural networks[120]. ANNs consist of interconnected nodes that are organized into layers, with each node performing a simple mathematical operation on its inputs and transmitting the result to nodes in the next layer[121]. Through training on large datasets, ANNs can learn to identify complex patterns and relationships in data and make accurate predictions or classifications. ANNs have found applications in a wide range of fields, including computer vision, speech recognition, natural language processing, robotics, and finance[122]. In recent years, the development of deep learning techniques, which use ANNs with many layers, has led to breakthroughs in image and speech recognition, natural language processing, and other areas[123]. Despite their success, ANNs also have some limitations, including a lack of interpretability, sensitivity to noisy or biased data, and the need for large datasets and computational resources for training. Nonetheless, ANNs continue to be a subject of active research and development, with ongoing efforts to improve their performance, robustness, and interpretability. As such, ANNs are expected to play an increasingly important role in solving complex problems in science and engineering.

4.2.1 General Structure

Throughout history, scientists have sought to simulate the human brain and create machines capable of thought. The key to human thinking lies in the complex neural network present in the human body [124]. The human brain processes information and makes decisions through a series of intricate processes that involve millions of interconnected neurons. Neurons are specialized cells that transmit and process information. They receive signals from other neurons through synapses, and when the incoming signals are strong enough, they generate electrical impulses or action potentials, which are then transmitted to other neurons through their axons. The process of information transmission in the human brain is highly complex, involving the interaction of multiple neurons, each of which can receive and transmit signals from many other neurons. Artificial neural networks attempt to mimic the structure and function of the neural network in the human brain. ANNs are composed of artificial neurons that receive input signals, process them, and generate output signals. These artificial neurons are organized into layers, with each layer performing a specific function in the neural network.

The first artificial neuron model called the Perceptron, was proposed in the 1960s by Frank Rosenblatt [125]. The Perceptron was a simple model that consisted of a single artificial neuron that could process binary inputs and generate a binary output. However, it was limited in its ability to model complex patterns and was soon replaced by more sophisticated models. Modern ANNs are much more complex and can learn to recognize complex patterns and relationships in data through training on large datasets. ANNs consist of multiple layers of artificial neurons, with each layer performing a different function. The input layer receives the input data, and the output layer generates the output. The hidden layers, which are located between the input and output layers, perform intermediate processing tasks. The weights of the connections between the artificial neurons in an ANN are adjusted during the training process to minimize the error between the predicted output and the actual output. This process of adjusting the weights is known as backpropagation and is a fundamental component of training ANNs.

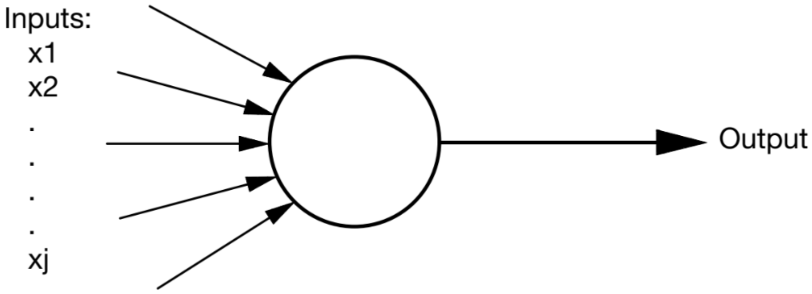

Figure 4.1: A basic type of perceptron

In Figure 4.1, an artificial neuron, known as a perceptron, is represented by a circle. The perceptron receives multiple inputs (x_1, x_2, x_3, etc.) and produces an output, similar to the way nerve endings sense changes in the external environment and transmit electrical signals.

For simplicity, we assume each input has only two possibilities: 1 or 0. If all inputs are 1, all conditions hold, and the output is 1. If all inputs are 0, none of the conditions hold, and the output is 0. In reality, different factors may have varying levels of importance, and thus, it is possible to assign weights to these factors to reflect their relative significance. Higher weights indicate more important factors, while lower weights represent less important ones.

To determine the output, a threshold value is also specified. If the sum of the products of factors and weights is greater than the threshold, the perceptron outputs 1; otherwise, it outputs 0. The threshold level represents the intensity of willingness, with a lower threshold indicating a result closer to “yes”, and a higher threshold tending to be closer to “no”. This can be expressed in the following equation:

$$Output = \begin{cases} 0, & \sum_j w_j x_j \leq threshold, \\ 1, & \sum_j w_j x_j > threshold. \end{cases} \tag{4.1}$$

In Equation (4.1), x represents all the different kinds of factors, and w denotes the corresponding weight. While a single perceptron can serve as a simple decision model, more complex decision models can be constructed by combining multiple perceptrons and creating multiple layers of networks. These networks can be trained on large datasets to learn complex patterns and relationships in the data and make accurate predictions or classifications.

In the Perceptron model, external factors x_1, x_2 ... x_j can be represented as a vector $\tilde{\mathbf{x}}$, and the weights w_1, w_2... w_j can be represented as a vector $\tilde{\mathbf{w}}$. The dot product of $\tilde{\mathbf{w}}$ and $\tilde{\mathbf{x}}$ can be defined as $\tilde{\mathbf{w}} \cdot \tilde{\mathbf{x}} = \sum_{i=1}^{j} w_i x_i$, which yields the sum of the products of the factors and weights.

Figure 4.2 depicts a schematic representation of a generalized multi-layer neural network with example neurons in each layer. The flow of data starts from the input layer, where

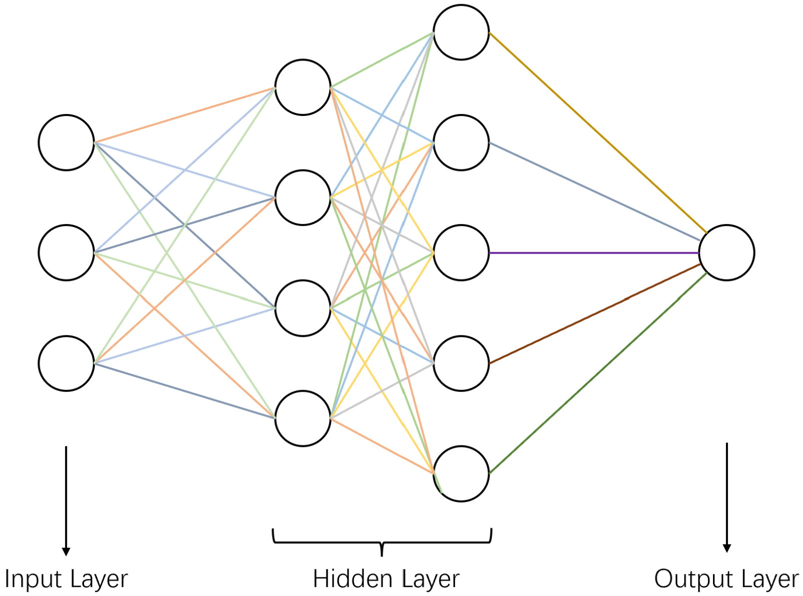

Figure 4.2: A sketch of general ANN network

the data is inputted, and propagates through the hidden layers until it reaches the output layer, which is responsible for generating the final predictions. Each node in the input layer represents a distinct feature or an input variable. Moreover, every node within the network functions by accepting inputs from the preceding layer, subsequently calculating an output based on a combination of its inputs, weights, and activation function. The number of hidden layers and the number of nodes in each layer can vary depending on the architecture of the neural network.

The Perceptron model can be rewritten as a function that takes into account a threshold b, defined as $b = -\text{threshold}$. The output of the model can then be written as:

$$Output = \begin{cases} 0, & x \cdot w + b \leq 0, \\ 1, & x \cdot w + b > 0. \end{cases} \tag{4.2}$$

To convert the output into a continuous function, we can introduce the variable z and define it as $z = \tilde{\mathbf{w}} \cdot \tilde{\mathbf{x}} + b$. The sigmoid function, which is defined as $\sigma(z) = \frac{1}{1+e^{-z}}$, can then be used to obtain a continuous output. As z approaches infinity, $\sigma(z)$ approaches 1, and as z approaches negative infinity, $\sigma(z)$ approaches 0. This relationship is illustrated by the sigmoid function graph shown in Figure 4.3.

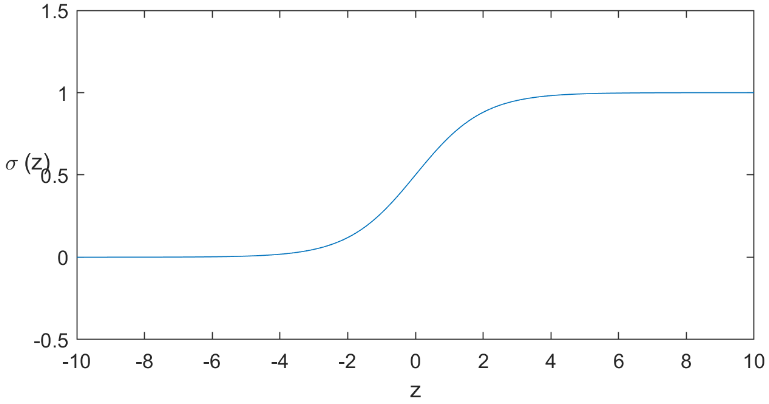

Figure 4.3: Sigmoid function

We can also calculate the change in the output Δoutput by considering the changes in weights Δw_j and bias Δb. This can be done by using the partial derivatives of the output with respect to w_j and b, as follows:

$$\Delta\text{output} \approx \sum_j \frac{\partial\text{output}}{\partial w_j}\Delta w_j + \sum_j \frac{\partial\text{output}}{\partial b}\Delta b, \tag{4.3}$$

where the summation is taken over all the weights and biases.

4.2.2 Important Features of the Network Structure

ANNs are highly flexible models, and their structure can vary widely depending on the task and the data at hand. However, there are certain important features of the ANN structure that can impact the performance of the model.

Number of Neurons

Neurons are the fundamental building blocks of an ANN model. They are responsible for processing and transmitting information throughout the network. Each neuron receives input signals from other neurons or external sources, which are then processed through a mathematical operation that involves multiplying the input signals by weights, adding a bias term, and passing the result through an activation function. The output signal generated by the neuron is then transmitted to other neurons in the network.

The design and configuration of neurons in an ANN model can have a significant impact on its performance. The number of neurons in a network can affect its capacity to learn complex patterns in the data. Increasing the number of neurons in an ANN can improve its ability to capture complex relationships and patterns in the data. This is because more neurons increase the model's capacity to represent more complex functions. However, this increase in capacity comes at the cost of increased computational requirements and training time. Furthermore, excessively large networks can lead to overfitting, a phenomenon in which the model becomes too specialized to the training data and fails to generalize to unseen data. This is because a large network has a greater capacity to memorize the training data, which can lead to reduced performance on new data.

Therefore, selecting the optimal number of neurons is crucial for achieving good performance in an ANN. This requires a balance between model capacity and generalization ability. The optimal number of neurons depends on various factors, such as the complexity of the problem, the amount of available data, and the architecture of the network. It is often necessary to experiment with different numbers of neurons and other hyperparameters to identify the optimal configuration.

Overall, the number of neurons is a critical hyperparameter in the design of ANNs, and choosing the optimal number requires careful consideration of the trade-offs between model capacity and generalization ability.

Number of Hidden Layers

The number of hidden layers in an Artificial Neural Network (ANN) is another important hyperparameter that can significantly impact the model's performance. Adding more hidden layers to an ANN can increase its ability to learn complex representations of the data, but it can also lead to issues such as vanishing or exploding gradients, which can hinder the model's training and affect its performance.

Increasing the number of hidden layers in an ANN allows the model to learn increasingly complex features and representations of the input data. This is because each hidden layer can learn a different set of features or representations, which are then combined in the final output layer. As a result, deeper networks can learn more abstract and hierarchical representations of the data, which can be beneficial for complex tasks. For example, consider a multi-layer ANN network that predicts real gas thermodynamic properties—such as enthalpy, entropy, or internal energy—based on features like pressure, density, and temperature. The network utilizes its hidden layers to learn progressively complex representations. The initial hidden layer primarily comprehends basic relationships between the features, like the direct correlation between pressure and density at a constant temperature. Subsequent layers extrapolate these rudimentary principles, identifying more nuanced dependencies among the features. This includes discerning how changes in pressure and temperature collectively impact the density of a real gas and eventually learning advanced physical effects. The final layer, synthesizing these multifaceted feature interactions, generates a prediction for the gas's thermodynamic properties, illustrating how each layer in the ANN contributes to understanding different aspects of complexity within the data.

However, deeper networks can also suffer from vanishing or exploding gradients, which are issues that arise during the backpropagation algorithm used for training ANNs. Vanishing gradients occur when the gradients of the loss function with respect to the parameters of the lower layers become very small, making it difficult for the model to update these parameters effectively. Conversely, exploding gradients occur when the gradients become very large, leading to instability and slower convergence during training. To address these issues, various techniques have been proposed, such as using different activation functions, regularization methods, and normalization techniques. Moreover, the optimal number of hidden layers in an ANN depends on various factors, such as the complexity of the problem, the size and structure of the input data, and the available computing resources.

In summary, increasing the number of hidden layers in an ANN can increase its ability to learn complex representations of the data, but it can also lead to issues such as vanishing or exploding gradients. Therefore, selecting the optimal number of hidden layers requires careful consideration of the trade-offs between model complexity and training stability, and often requires experimentation and hyperparameter tuning.

Activation Functions

The activation function is an essential component of an ANN that introduces nonlinearity and allows the network to model complex nonlinear relationships in the data. The number of activation functions used in an ANN depends on the number of layers and the type of architecture used, and it can have a significant impact on the performance of the model. Each layer in an ANN typically uses a separate activation function to introduce nonlinearity into the model. Commonly used activation functions include the sigmoid function, the hyperbolic tangent function, the Rectified Linear Unit (ReLU), and its variants, such as Leaky ReLU and Exponential Linear Units (ELUs).

Using different activation functions can affect the model's performance in various ways. For example, sigmoid and hyperbolic tangent functions are suitable for binary classification problems and can help prevent overfitting. On the other hand, ReLU-based activation functions are widely used in deep neural networks due to their ability to handle vanishing gradients and improve training speed. Moreover, the choice of activation function can impact the model's ability to learn and generalize to new data. Some activation functions, such as the sigmoid and hyperbolic tangent functions, can saturate and become ineffective when the input values are too large or too small. Other activation functions, such as the ReLU function, can suffer from the "dying ReLU" problem, where the output of the neuron becomes zero for negative input values, leading to the inability to learn.

Therefore, selecting the optimal activation function(s) for an ANN is crucial for achieving good performance. This requires careful consideration of the problem's characteristics, the architecture of the network, and the available data. It is often necessary to experiment with different activation functions and other hyperparameters to find the best combination for a given task. By using the appropriate activation functions, the ANN can learn complex relationships and generalize well to new data.

Learning Rate

The learning rate is a critical hyperparameter in an ANN that controls the magnitude of the updates made to the network's weights during training. The learning rate determines how quickly the model adapts to the training data and can have a significant impact on the model's performance. Imagine the previously mentioned ANN network to predict real gas thermodynamic properties (for example, enthalpy) based on pressure and temperature. We start with random weights and then iteratively update these weights based on the error (difference between the predicted and actual enthalpy). If we set a high learning rate (for example, 0.1), our weight updates will be large, and the algorithm might converge quickly. However, this also risks overshooting the minimum point of the loss function and results in an unstable learning process, where the error might oscillate without ever minimizing. On the contrary, if we set a small learning rate (for example, 0.001), our weight updates will be minor, leading to a more stable learning process. The algorithm will take smaller, more precise steps toward the minimum of the loss function. However, this might also make the learning process slow and the algorithm could get stuck in a local minimum rather than finding the global minimum. Therefore, the learning rate needs to be chosen carefully. It should be high enough to allow fast convergence, but not so high that it causes instability or prevents the model from finding the optimal solution.

The optimal learning rate depends on various factors, such as the complexity of the problem, the size of the data set, and the architecture of the network. In general, it is recommended to start with a small learning rate and increase it gradually until convergence is achieved. However, if the learning rate is too small, the model may get stuck in a local minimum, leading to poor performance. Therefore, it is often necessary to experiment with different learning rates and adjust them based on the model's performance during training. Moreover, it is common to use adaptive learning rates methods, such as the Adam optimizer, which adjust the learning rate based on the gradients and the history of the weight updates. These methods can improve the efficiency and stability of the training process and often lead to better performance than fixed learning rates.

Number of Epochs

The number of epochs is a hyperparameter in an Artificial Neural Network (ANN) that determines the number of times the entire dataset is passed through the network during training. It is one of the critical hyperparameters that can significantly impact the performance of the ANN. For instance, imagine we are training an ANN network on a dataset of 1,000 data points for a gas model prediction task. During training, the network will learn by adjusting its weights based on the error it made in its predictions. If we set the number of epochs to 10, this means that the entire dataset of 1,000 data points will be passed through the network 10 times. Each pass involves presenting all data points to the network, updating the network weights based on the error it made in its predictions, and then starting again with the first data point. The optimal number of epochs depends on various factors, including the intricacy of the issue at hand, the dataset's magnitude, the network's architecture, and the learning rate. In general, if the number of epochs is too low, the model may not have enough time to learn the patterns in the data and may underfit the training data. Conversely, if the number of epochs is too high, the model may memorize the training data and overfit, leading to a poor generalization of new data.

To determine the optimal number of epochs, it is common to use techniques such as cross-validation or monitoring the loss and accuracy on a validation dataset during training. These techniques can help identify the point where the model starts to overfit and the performance on the validation dataset starts to degrade. The number of epochs at this point can be used as a stopping criterion to avoid overfitting and achieve good generalization performance. Moreover, it is common to use early stopping techniques, where training is stopped before the model starts to overfit. Early stopping can be based on various criteria, such as the validation loss or the validation accuracy, and can help avoid overfitting and improve generalization performance.

4.2.3 Training Functions

Training functions for ANNs are algorithms that are used to optimize the network's performance during the training process. They work by adjusting the weights and biases of the network to minimize the error between the predicted output and the actual output. There are various types of training functions available, including gradient descent, backpropagation, Levenberg-Marquardt, Bayesian regularization, conjugate gradient, etc. Each of these algorithms has its own strengths and weaknesses, and the choice of training function depends on the specific application and the type of data being used. Proper training of an ANN is crucial for its accurate and efficient performance. A well-trained network can accurately predict outputs for new inputs, while an improperly trained network may produce inaccurate or inconsistent results. Therefore, selecting an appropriate training function and optimizing its parameters is an essential task in the development of a successful ANN.

Gradient Descent

Gradient Descent is an iterative optimization algorithm that is used to minimize an error function by adjusting the parameters of a model in the direction of the negative gradient of the function. In the context of ANNs, Gradient Descent is used to adjust the weights and biases of the network to minimize the difference between the predicted outputs and the actual outputs. The basic idea behind Gradient Descent is to start with an initial set of parameters for the model and then iteratively update those parameters in the direction of the negative gradient of the error function. The negative gradient points in the direction of the steepest descent, which is the direction that will result in the greatest reduction in the error function.

More formally, let us consider a cost function $J(w)$ that depends on the weights w of an ANN. The goal of Gradient Descent is to find the values of w that minimize $J(w)$. We start with an initial guess w_0 and update it at each iteration using the following rule:

$$w_{i+1} = w_i - \alpha \nabla J(w_i), \tag{4.4}$$

where α is the learning rate, and $\nabla J(w_i)$ is the gradient of the cost function evaluated at w_i. The learning rate is a hyperparameter that determines the step size taken in the direction of the negative gradient. A smaller learning rate will result in smaller steps and a more cautious approach, while a larger learning rate will result in larger steps and a more aggressive approach.

The gradient of the cost function is a vector that points in the direction of the steepest ascent of the function. To move in the direction of the steepest descent, we take the negative of the gradient, as shown in the update rule above.

The gradient can be computed using the chain rule of differentiation:

$$\nabla J(w_i) = \frac{\partial J(w_i)}{\partial w_i} = \sum_{n=1}^{N} \frac{\partial J_n(w_i)}{\partial w_i}, \tag{4.5}$$

where $J_n(w_i)$ is the cost function for a single training example n. The sum over N training examples are used to compute the average gradient over the entire training set.

There are different variants of Gradient Descent, including batch Gradient Descent, stochastic Gradient Descent, and mini-batch Gradient Descent. Batch Gradient Descent computes the gradient over the entire training set, while stochastic Gradient Descent computes the gradient for a single training example. Mini-batch Gradient Descent computes the gradient for a small subset of the training set. Gradient Descent also has some limitations, including the possibility of getting stuck in a local minimum of the error function or oscillating around the minimum. There are several extensions to Gradient Descent, such as momentum-based methods, adaptive learning rates, and second-order methods, that address these issues.

Levenberg-Marquardt

Levenberg-Marquardt is a popular training function used in ANNs for non-linear regression problems. The basic idea behind Levenberg-Marquardt[126] is to minimize the sum of squares of the differences between the predicted outputs and the actual outputs by adjusting the weights and biases of the network. The algorithm starts with an initial guess for the weights and biases and iteratively updates them until the error function is minimized. It is a combination of two other training functions: the steepest descent algorithm and the Gauss-Newton algorithm, and it can be used to train ANNs with non-linear activation functions. The steepest descent algorithm is used to update the weights and biases of the ANN in the direction of the steepest descent of the error function. The Gauss-Newton algorithm[127], on the other hand, is used to update the weights and biases of the ANN based on the curvature of the error function.

More formally, let us consider a non-linear regression problem that can be formulated as follows:

$$y_i = f(x_i; w) + \epsilon_i, \tag{4.6}$$

where y_i is the observed output for the i-th input x_i, $f(x_i; w)$ is the predicted output of the ANN with weights w, and ϵ_i is the error term. The goal of Levenberg-Marquardt is to find the values of w that minimize the sum of squares of the errors:

$$J(w) = \frac{1}{2}\sum_{i=1}^{n} \epsilon_i^2. \tag{4.7}$$

The Levenberg-Marquardt algorithm starts with an initial guess for the weights, denoted as w_0. At each iteration, it computes the gradient and the Hessian of the error function with respect to the weights:

$$\nabla J(w_i) = \sum_{i=1}^{n} \frac{\partial \epsilon_i}{\partial w_i} \epsilon_i, \tag{4.8}$$

$$\mathbf{H}(w_i) = \sum_{i=1}^{n} \frac{\partial \epsilon_i}{\partial w_i} \frac{\partial \epsilon_i}{\partial w_i}^{\top} + \lambda_i \mathbf{I}, \tag{4.9}$$

where $\mathbf{I}$ is the identity matrix, and λ_i is a damping parameter that controls the trade-off between the steepest descent and Gauss-Newton methods.

The Levenberg-Marquardt algorithm then computes the updated weights using the following rule:

$$w_{i+1} = w_i - \mathbf{H}(w_i)^{-1}\nabla J(w_i). \tag{4.10}$$

When λ_i is large, the algorithm behaves more like the steepest descent, while when λ_i is small, it behaves more like Gauss-Newton. If the error function decreases, the damping parameter is reduced, and the algorithm moves closer to Gauss-Newton. If the error function increases, the damping parameter is increased, and the algorithm moves closer to the steepest descent.

The Levenberg-Marquardt algorithm has several advantages over other optimization algorithms. It is computationally efficient and can handle non-linear activation functions. It also has the ability to adjust the damping parameter automatically, making it more robust to noisy data.

Bayesian Regularization

Bayesian regularization is a statistical method for regularizing machine learning models that are based on Bayesian statistics, which is used in ANNs to reduce overfitting. Overfitting occurs when an ANN is trained too well on the training data and becomes too specific to that data, resulting in poor performance on new, unseen data. Bayesian regularization works by adding a penalty term to the error function that encourages the ANN to have smaller weights and biases. This helps to reduce the complexity of the ANN and prevent overfitting.

In Bayesian regularization, a prior distribution is placed on the model parameters, which represents our prior beliefs about the distribution of parameter values. The prior distribution is typically chosen to be a normal distribution, with a mean of zero and a variance that reflects our uncertainty about the parameter values. By placing a prior distribution on the model parameters, Bayesian regularization encourages the model to have parameter values that are close to zero, unless there is strong evidence from the data that a particular parameter should have a non-zero value. Subsequently, the posterior distribution, delineating our posteriori beliefs about the plausible range of the parameters, is deduced by amalgamating the a priori distribution and the data likelihood given the model parameters. This amalgamation is executed according to the precepts of Bayes' theorem. The posterior distribution is used to make predictions about new data, by computing the expected value of the model output given the posterior distribution over the parameters. The expected value is a weighted average of the model outputs for each possible parameter value, where the weights are given by the posterior probability of each parameter value. The strength of the regularization can be controlled by adjusting the variance of the prior distribution. A larger variance will result in weaker regularization, allowing the model to fit the training data more closely, while a smaller variance will result in stronger regularization, leading to a simpler model with fewer non-zero parameter values.

Bayesian regularization has several advantages over other forms of regularization, such as L1 and L2 regularization. Firstly, it can handle correlated features more effectively, since the prior distribution is placed on the parameters themselves rather than on the feature values. Secondly, it provides a probabilistic framework for modeling uncertainty in the model parameters, which can be useful for decision-making and for incorporating domain knowledge into the model.

There are numerous training functions available for ANN, each with unique advantages and disadvantages. Each of these training functions has its own set of parameters and learning rules that can influence the performance of the ANN. The choice of training function can significantly impact the performance and accuracy of the network. However, for the sake of simplicity, we shall refrain from elaborating on all the details of the available training functions. Instead, our primary attention in this study will be directed toward the aforementioned training functions. Our goal is to explore the effectiveness and limitations of these functions in training an ANN, and how they can impact the network's performance in different applications.

4.3 Prediction of Thermodynamics Properties of Dense Gas

Machine learning (ML) algorithms have revolutionized the field of thermodynamics, enabling the identification and prediction of thermodynamic properties of pure fluids and their mixtures with remarkable accuracy. This is particularly valuable in cases where theoretical models may not provide reliable results. However, to realize the full potential of ML in this field, it is crucial to construct comprehensive datasets that encompass a diverse range of thermodynamic parameters. These datasets serve as a foundation for training and validating ML models, ensuring that they accurately reflect the underlying physical behavior of the systems under investigation.

The process of selecting the most suitable ML algorithms and model architectures is another critical aspect of achieving high prediction accuracy. A wide range of ML algorithms exists, each with unique strengths and weaknesses. Artificial neural networks (ANNs) are commonly used in thermodynamic modeling due to their ability to learn complex relationships between variables. The selection of a suitable training function for an ANN is a crucial step in achieving optimal performance. By examining and comparing the performance of different training functions, we can gain valuable insights into the mechanisms underlying the learning process of an ANN and identify ways to improve its efficiency and accuracy.

Furthermore, selecting an appropriate model architecture is equally important. The architecture determines the number and type of layers in the neural network, as well as the activation functions used in each layer. An optimized architecture can significantly enhance the accuracy of predictions and reduce computation time, leading to more efficient modeling. To put it succinctly, there exists a complementary relationship between the model architecture and the training function within the realm of machine learning. The model architecture fundamentally demarcates the upper boundaries of potential accuracy and efficiency. Subsequently, the training function's role is pivotal in optimizing the model parameters in order to attain this potential.

4.3.1 Generation of the Training Data Set

Generating a representative training data set is a crucial step in developing an accurate and effective ANN model for predicting the thermodynamic properties of dense gases. Our study uses the Van der Waals equation of state to calculate the thermodynamic properties of the gas at different densities and temperatures to generate such a data set.

The Van der Waals equation of state is a widely-used equation that describes the behavior of real gases in terms of their pressure, volume, and temperature. To generate a training data set using the Van der Waals equation, we must first set up the equation with appropriate input parameters. The input parameters should be varied over a range of values to cover the expected range of densities and temperatures for the gas. Once the input parameters are set, the Van der Waals equation can be used to calculate the thermodynamic properties of the gas, such as its compressibility factor, enthalpy, pressure, and speed of sound, which can serve as the target outputs for the ANN model. It is important to ensure that the data is diverse and representative of the full range of possible inputs and that the training data set is large enough to adequately represent the range of densities and temperatures the model will be required to predict.

Our research study is primarily focused on exploring the region that lies above and in close proximity to the liquid-vapor saturation line, which is a critical area for understanding the complex and nonconventional behavior of dense gases. To achieve these objectives, the training data is generated and plotted on the pressure-specific volume plane, which is depicted in Figure 4.4. We aim to leverage the training data set and apply ANN models to gain insights into the thermodynamic properties of dense gases in this region. By analyzing the performance of the ANN model, we hope to develop new theoretical models that accurately describe the behavior of these gases.

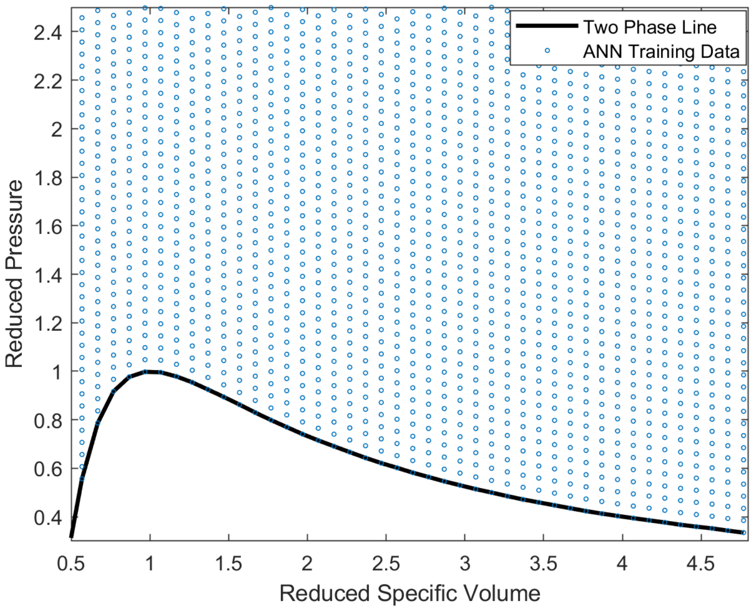

Figure 4.4: Training data set for ANN model

While the VdW equation can provide a useful starting point for generating training data, it is important to validate the accuracy and effectiveness of the ANN model using experimental or simulation data in addition to the VdW-generated data. This will help ensure that the model is able to accurately predict the thermodynamic properties of dense gas under a range of conditions, even if they deviate from the assumptions of the VdW equation. Moreover, one must also bear in mind that the model's accuracy is only as good as the quality of the training data set, and thus care must be taken to ensure that the data is representative, accurate, and free from biases.

4.3.2 Accuracy and Performance of Different Models

To determine the optimal model for integration into our CFD code, a rigorous evaluation and comparison of models trained with various training functions and network architectures are required. This critical process necessitates a comprehensive assessment of the accuracy of each model. By conducting such an evaluation, we can ensure that the model we ultimately choose is capable of providing reliable and precise results, which are crucial for accurate simulations in later CFD simulations.

To begin the evaluation process, the data should be split into training, validation, and test sets. The training set is used to train the model, the validation set is used to evaluate the performance of the model during training and to tune hyperparameters, and the test set is used to evaluate the final performance of the model. Once the data is split, the architecture of the ANN model should be defined. This includes the number of layers, neurons per layer, and any other relevant hyperparameters. The model can then be trained using each of the different training functions that are to be compared. The validation accuracy or other relevant performance metrics should be tracked for each training function. The training function that performs the best on the validation set should be chosen. It is important to select the training function that performs well on the validation set, as this indicates that it is likely to perform well on new, unseen data.

In addition to the commonly used performance metrics such as mean absolute error(MAE), mean squared error(MSE), etc, the CPU time required for training an ANN model can also be considered as an important metric to evaluate the model's performance, especially when working with large datasets or complex models. Longer training times can result in increased computational costs, which can be impractical for real-world applications. Additionally, training time can also be an indication of the model's efficiency and scalability. Several factors can influence the CPU time required for training an ANN model. The size and

Training Function	Network Structure	CPU Time for Training (s)
Levenberg-Marquardt	2-33-1	3.703125
Bayesian Regularization	2-50-1	4.906250
Scaled Conjugate Gradient	2-30-15-1	0.859375
BFGS Quasi-Newton	2-65-7-1	4.921875
Resilient Backpropagation	2-20-3-1	0.765625
Variable Learning Rate Gradient Descent	2-22-8-1	0.781250

Table 4.1: Comparison of Different ANN Models

complexity of the dataset, the number of layers and neurons in the model, the optimization algorithm used for training, and the hardware used for training are all factors that can impact training time. Therefore, it is important to report the CPU time required for training alongside other performance metrics to provide a comprehensive evaluation of the model's performance.

Table 4.1 presents six representative models from our training results. The table displays information about the training function, network structure, and CPU time for each model. In the table, "2-33-1" denotes that the network comprises one input layer with two neurons, one hidden layer with thirty-three neurons, and one output layer with one neuron. Different training functions and network structures have a significant impact on the CPU time required for training artificial neural network (ANN) models. The table shows that the Scaled Conjugate Gradient model with a 2-30-15-1 network structure requires the least amount of CPU time for training, whereas the Bayesian Regularization model with a 2-50-1 network structure requires the most amount of CPU time. However, we cannot conclude that the best-performing ANN model is the one with the lowest CPU time for training. Further evaluation and comparison of the performance of these models on test data is necessary to determine the most suitable ANN model for our problem.

Figure 4.5 illustrates an isentrope passing through the BZT region, serving as the test dataset for the trained models discussed earlier. In Figure 4.6, a detailed comparison between the predicted and original values for each model is presented, alongside the corresponding absolute percentage error.

The results reveal that the Bayesian Regularization model exhibits the highest accuracy among the tested models, with a maximum error of less than 0.5%. This model uses a regularization technique that adds a penalty term to the error function to minimize the risk of overfitting the training data. For example, consider the error function for a learning model with a parameter vector $\overrightarrow{w}$ defined as:

$$E(\overrightarrow{w}) = \frac{1}{2}\sum_{i=1}^{n}(y_i - f(\overrightarrow{x}_i, \overrightarrow{w}))^2$$

where y_i and $f(\overrightarrow{x}_i, \overrightarrow{w})$ are the true input and predicted output of the model for the i-th input, respectively.

In Bayesian regularization, a penalty term is added to the error function leading to the regularized error function:

$$E_{\text{reg}}(\overrightarrow{w}) = \frac{1}{2}\sum_{i=1}^{n}(y_i - f(\overrightarrow{x}_i, \overrightarrow{w}))^2 + \frac{\lambda}{2}||\overrightarrow{w}||^2$$

Here, the term $\frac{\lambda}{2}||\overrightarrow{w}||^2$ penalizes large weights in the model. This penalty term is equivalent to placing a Gaussian prior on the weights $\overrightarrow{w}$ with zero mean and variance $\frac{1}{\lambda}$. In terms of its role in reducing overfitting, the regularizer works by imposing a cost on the complexity of the model. This cost discourages the learning of overly complex models that fit the noise in the training data, promoting instead the learning of simpler models that are likely to generalize better to unseen data.

The Levenberg-Marquardt model also shows good agreement with the given test data, with a maximum error of approximately 2%. On the other hand, the Variable Learning Rate Gradient Descent model exhibits the highest error rate (defined as "(Targets-Outputs)/Targets") among the tested models. At certain locations, the error rate is almost 50%, rendering it unsuitable as a thermodynamic model for dense gases.

The comparison of the predicted and actual values, alongside the absolute percentage errors, provides valuable insights into the predictive power of each model, highlighting their strengths and weaknesses. Based on the current results, the Bayesian Regularization model is selected as the training function in our ANN model. Although the CPU time for training is slightly longer, this model exhibits the best match to the test data, demonstrating very good accuracy.

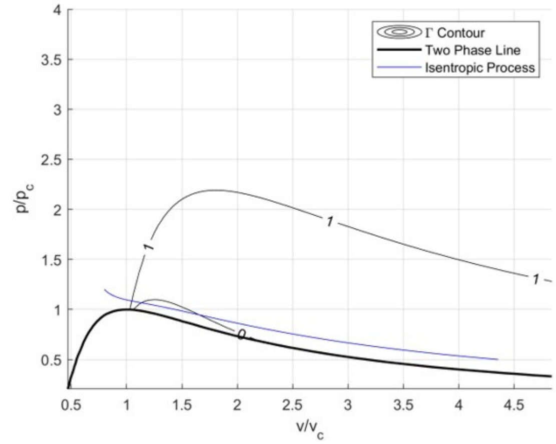

Figure 4.5: Sample isentrope to test the trained ANN model

4.4 Result Analysis and Discussion

In light of the preceding analysis, Bayesian Regularization was selected as the training function for the ANN model. Utilizing the provided training dataset, the ANN model was trained and subsequently integrated into our in-house CFD code. The traditional equation of state was supplanted by the newly implemented ANN model, which was employed to compute all thermodynamic properties of real gas.

The Sajben nozzle, a complex and versatile geometry commonly used in transonic flow studies, served as the basis for this investigation. This nozzle configuration allows for the

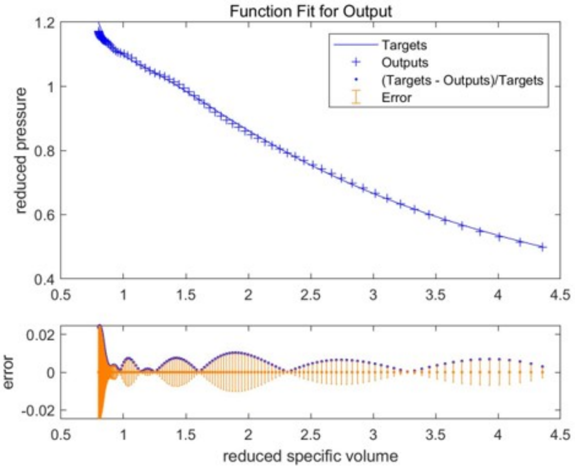

(a) Levenberg-Marquardt (b) Bayesian Regularization

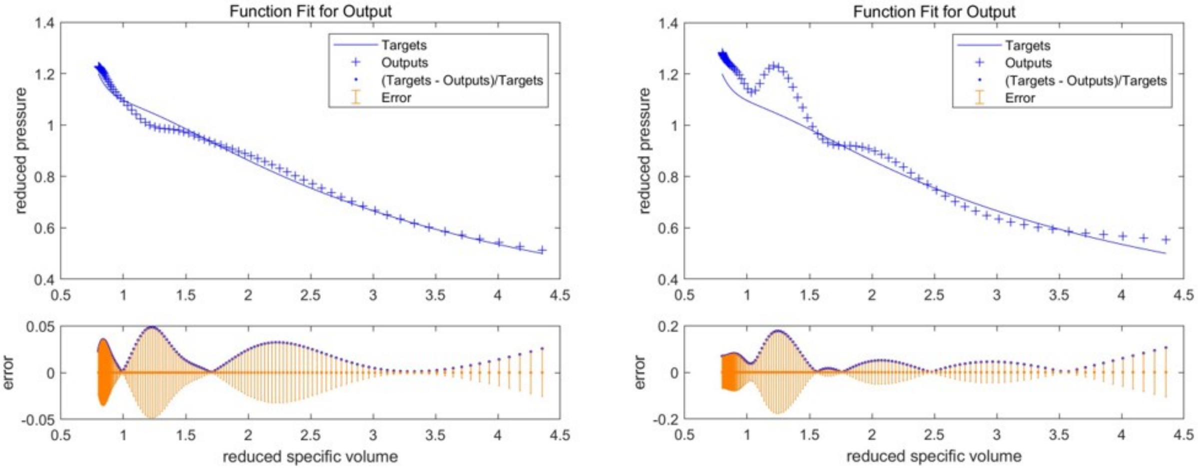

(c) Scaled Conjugate Gradient (d) BFGS Quasi-Newton

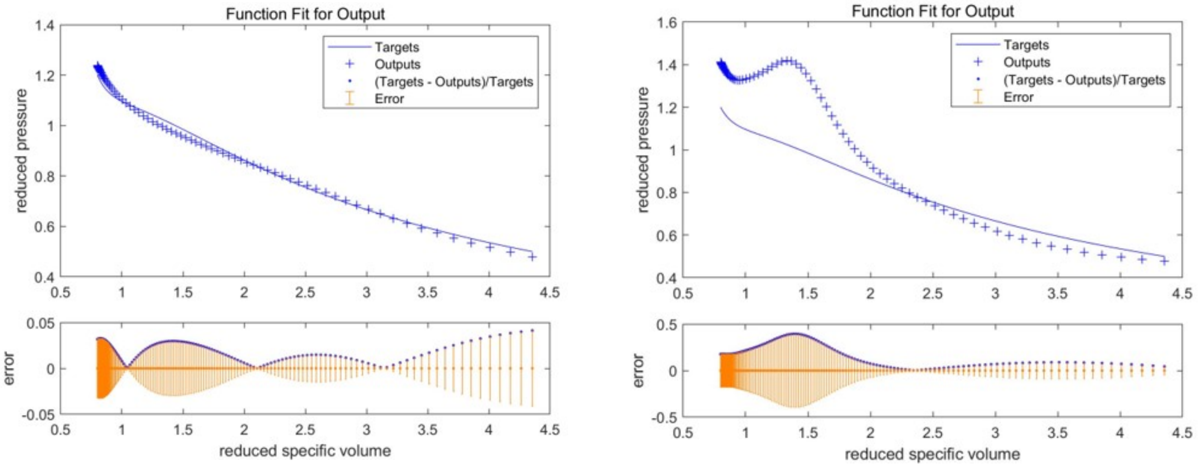

(e) Resilient Backpropagation (f) Variable Learning Rate Gradient Descent

Figure 4.6: Comparison of ANN model performance of different training functions

examination of flow behavior under various conditions, making it a suitable choice for evaluating the performance of the ANN model in calculating thermodynamic properties. Three distinct test cases featuring varying back pressure conditions were calculated and plotted. The simulation results that utilized the ANN model to determine thermodynamic properties were contrasted with those obtained using the conventional equation of state, as depicted in Figures 4.7 - 4.10. The three test cases encompassed a nozzle with subsonic back pressure, one containing a shock wave, and another with supersonic back pressure. Moreover, Figures 4.11, 4.12, and 4.13 illustrate the distribution of flow variables along the centerline for each of the cases.

As evidenced in Figure 4.11, for the case with subsonic back pressure, the neural network results closely align with the original results computed via the Van der Waals equation of state. The distribution of pressure, temperature, density, fundamental derivative, speed of sound, and Mach number along the centerline all demonstrate exceptional agreement. In the case with a shock wave inside the nozzle, as displayed in Figure 4.12, the flow variables similarly exhibit a high degree of congruence, barring the temperature distribution at the shock location. The temperature calculated with the neural network model is not as sharply defined as that of the conventional equation of state, although the error remains below 0.5%. The simulation for the case with supersonic back pressure, as illustrated in Figure 4.13, encounters a similar issue, with the sole discrepancy residing in the temperature distribution, and the maximum error approximating 0.2%. This level of error is considered acceptable.

In conclusion, ML algorithms hold immense promise in predicting the thermodynamic properties of pure fluids and their mixtures with remarkable precision. The implementation of ML models in thermodynamic property calculations liberate researchers from the dependence on conventional equations of state and the reliance on extensive experimental datasets. In the future, scientists may be able to develop accurate thermodynamic models from limited experimental data, thanks to the data-driven nature of ML-based techniques. By assembling diverse datasets and selecting the most suitable algorithms and architectures, we can harness the full potential of ML in this domain, enhance our comprehension of intricate thermodynamic systems, and ultimately drive advancements in scientific and industrial applications.

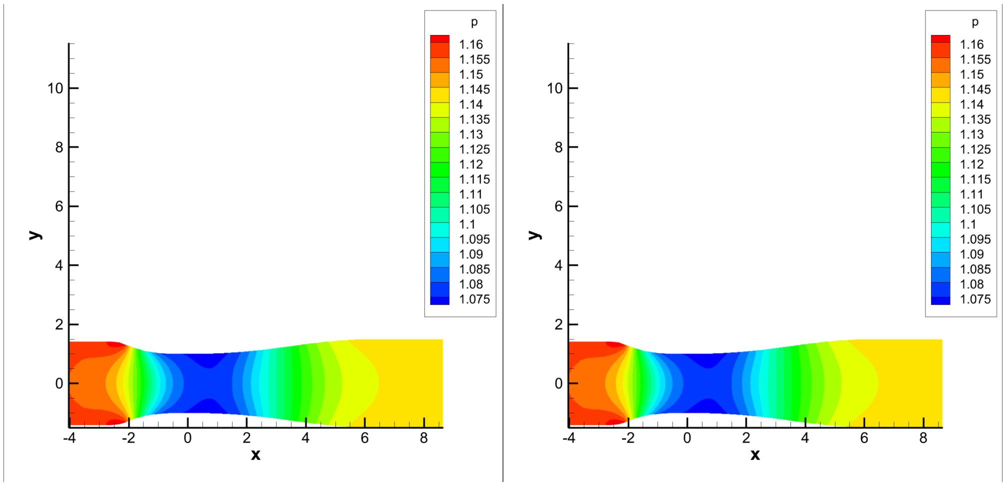

(a) Subsonic case - Equation of State (b) Subsonic case - Neural network

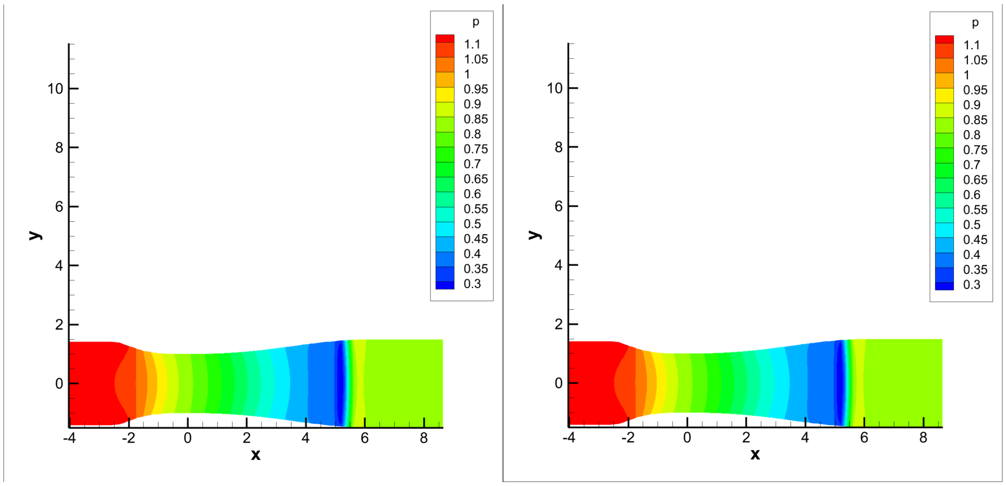

(c) Shock wave case - Equation of State (d) Shock wave case - Neural network

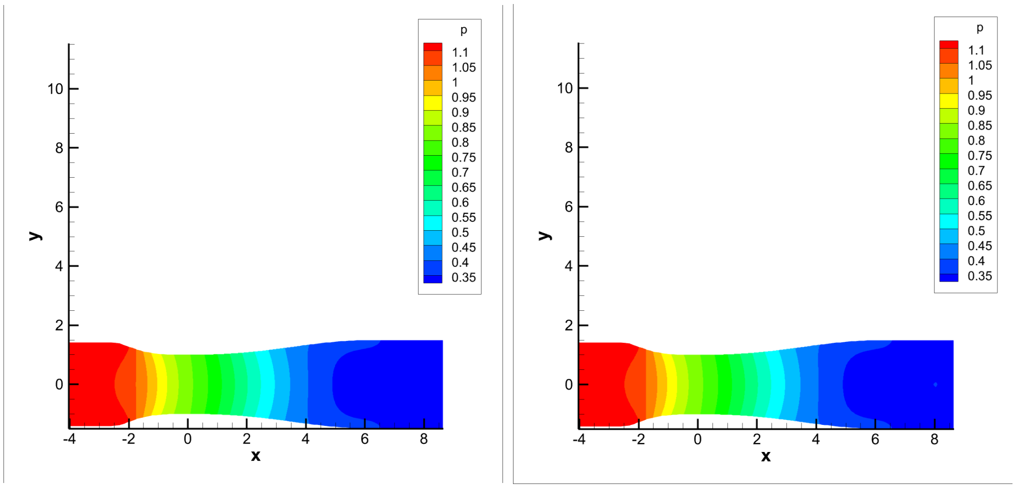

(e) Supersonic case - Equation of State (f) Supersonic case - Neural network

Figure 4.7: Pressure contour of simulation results by using Equation of State/Neural network

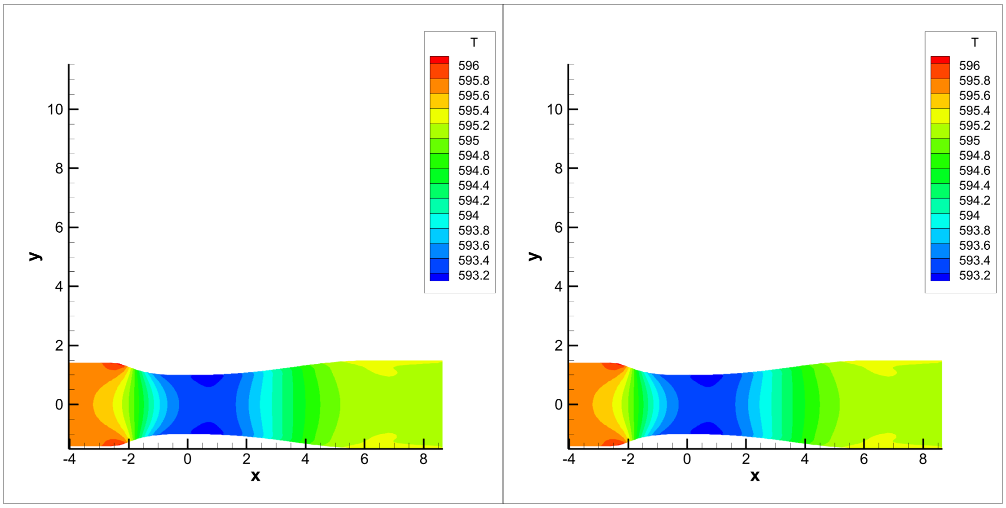

(a) Subsonic case - Equation of State (b) Subsonic case - Neural network

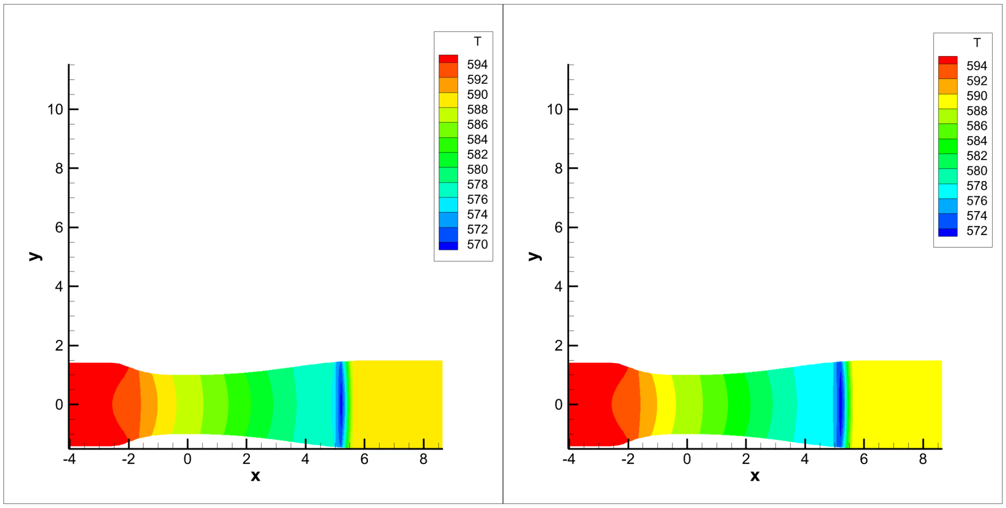

(c) Shock wave case - Equation of State (d) Shock wave case - Neural network

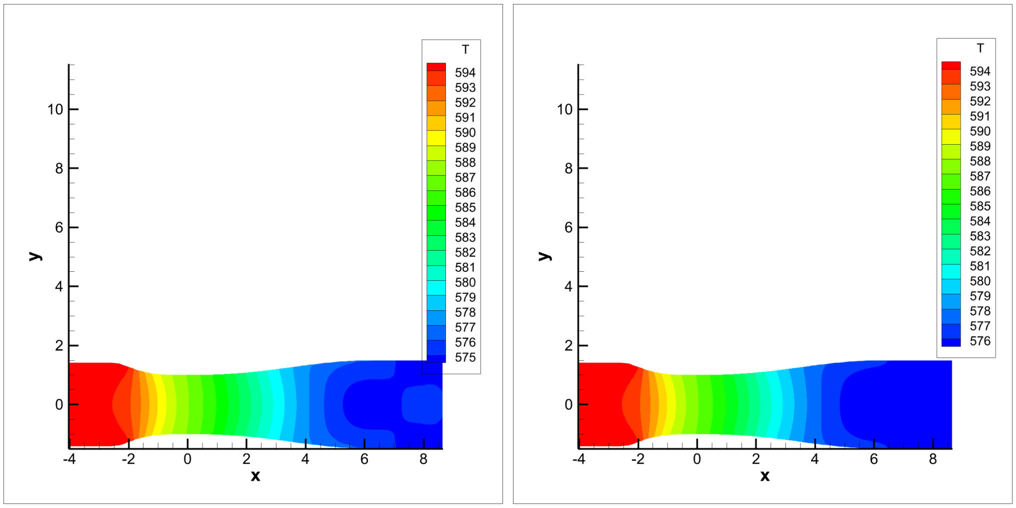

(e) Supersonic case - Equation of State (f) Supersonic case - Neural network

Figure 4.8: Temperature contour of simulation results by using Equation of State/Neural network

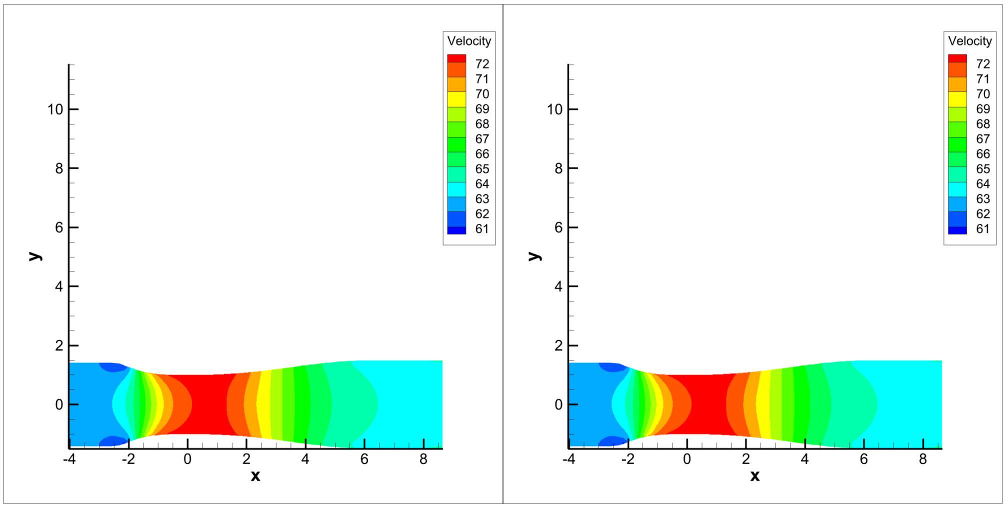

(a) Subsonic case - Equation of State (b) Subsonic case - Neural network

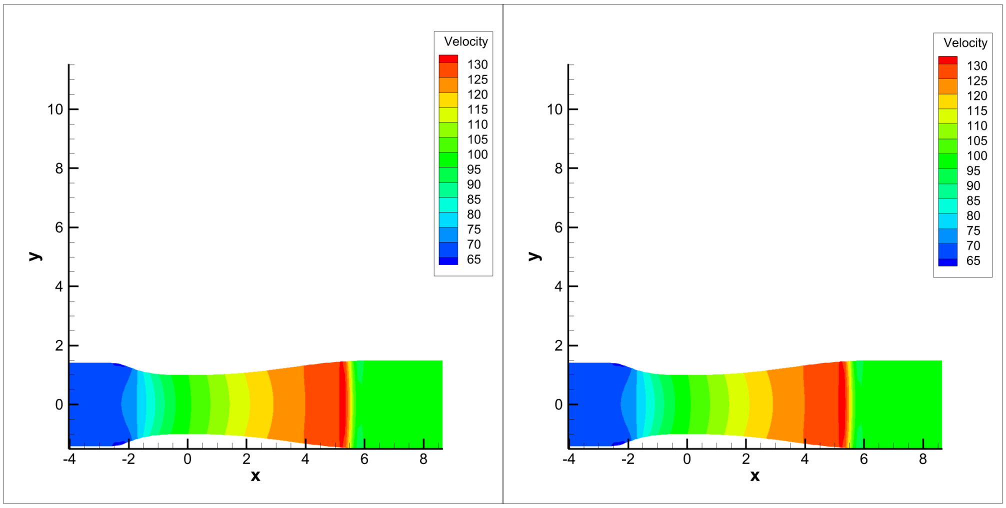

(c) Shock wave case - Equation of State (d) Shock wave case - Neural network

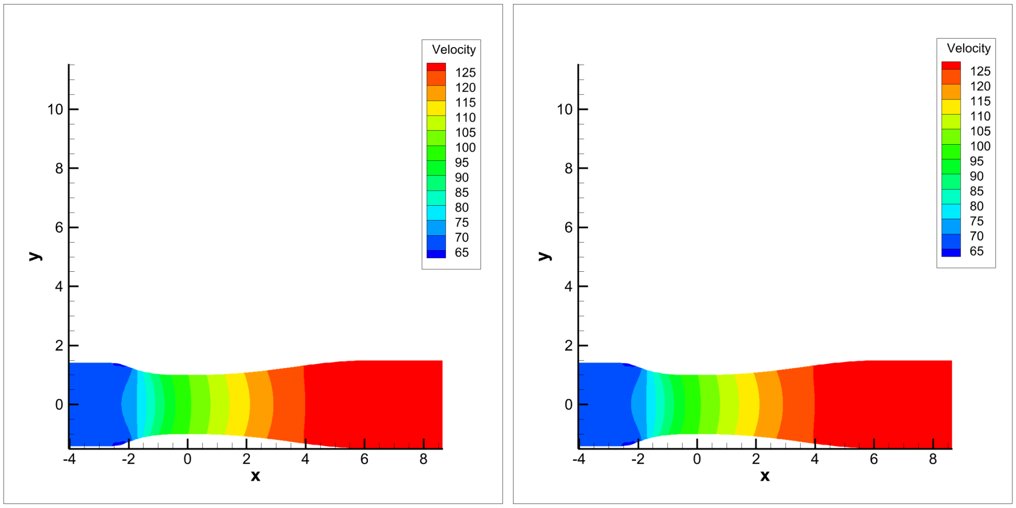

(e) Supersonic case - Equation of State (f) Supersonic case - Neural network

Figure 4.9: Velocity contour of simulation results by using Equation of State/Neural network

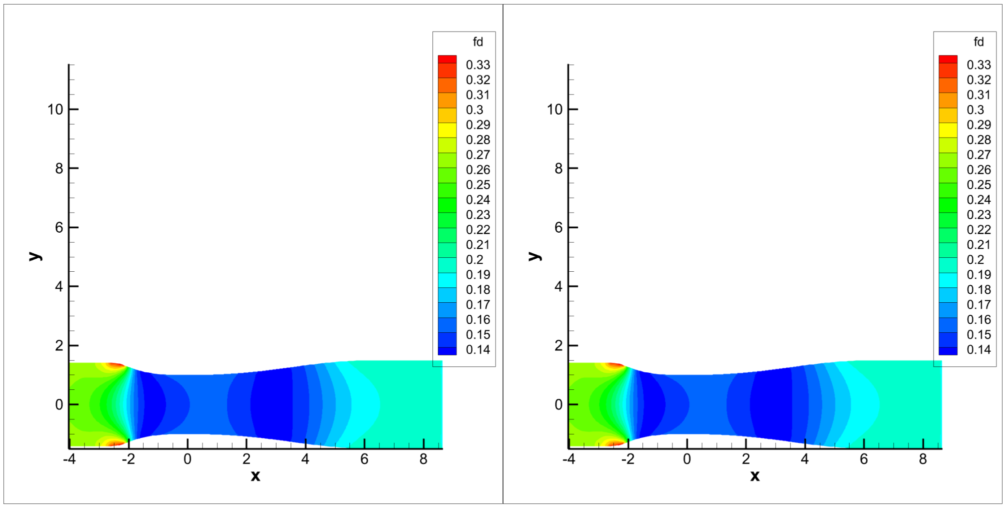

(a) Subsonic case - Equation of State (b) Subsonic case - Neural network

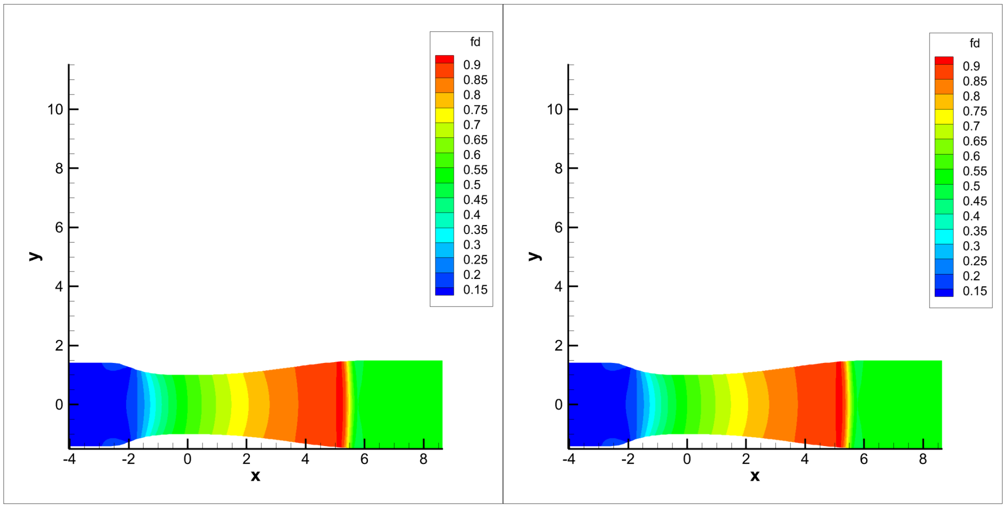

(c) Shock wave case - Equation of State (d) Shock wave case - Neural network

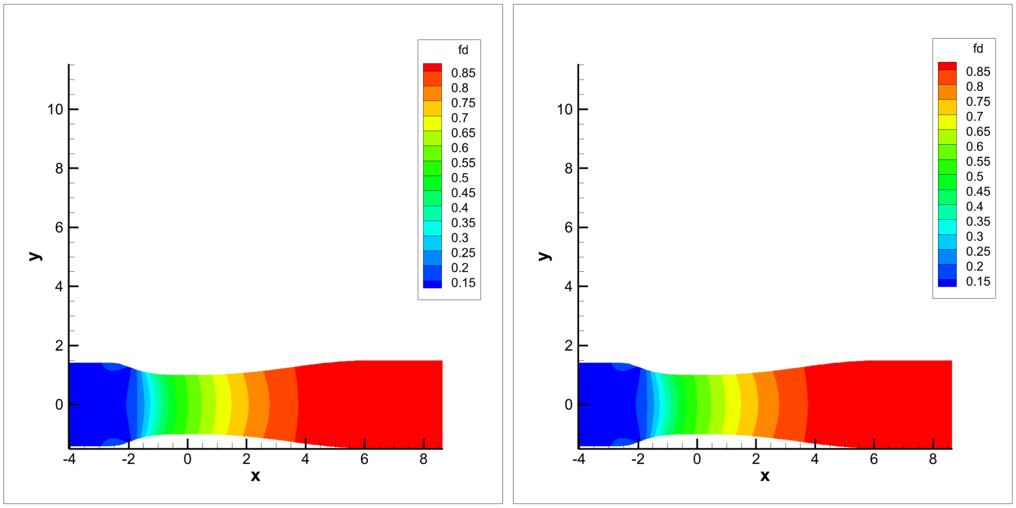

(e) Supersonic case - Equation of State (f) Supersonic case - Neural network

Figure 4.10: Fundamental derivative contour of simulation results by using Equation of State/Neural network

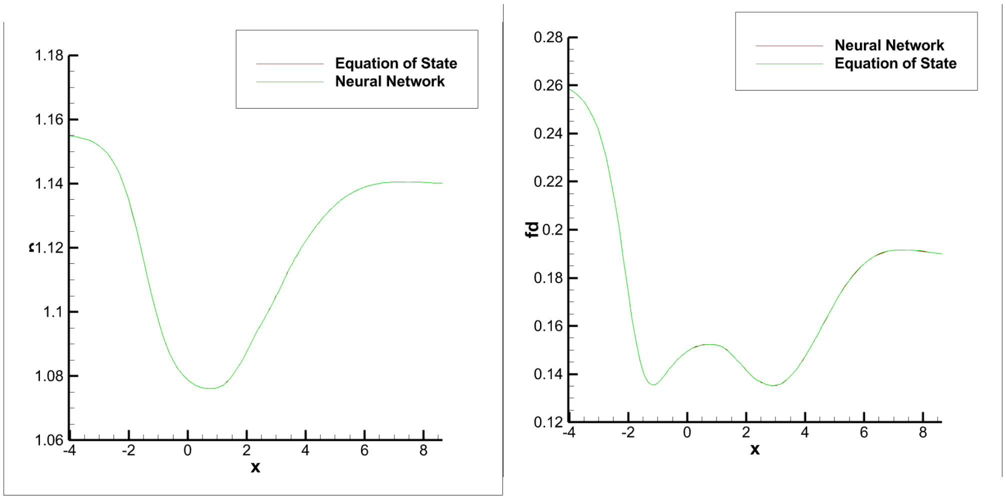

(a) Subsonic case - Pressure

(b) Subsonic case - Fundamental derivative

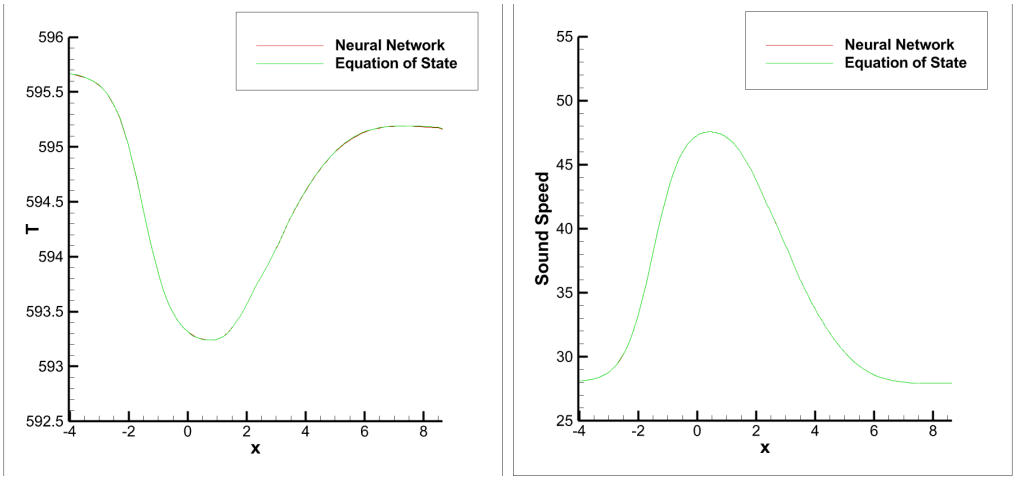

(c) Subsonic case - Temperature

(d) Subsonic case - Speed of sound

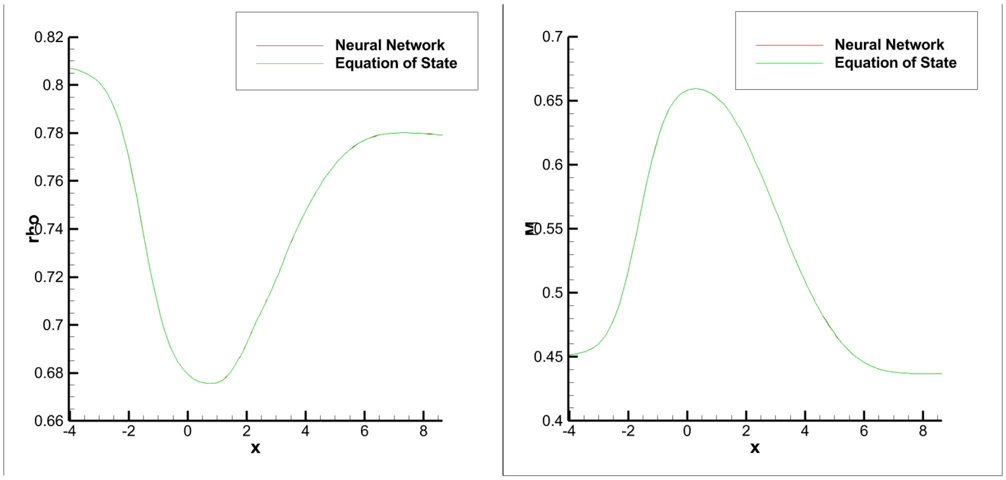

(e) Subsonic case - Density

(f) Subsonic case - Mach number

Figure 4.11: Subsonic case: Flow variable distribution along the nozzle centerline

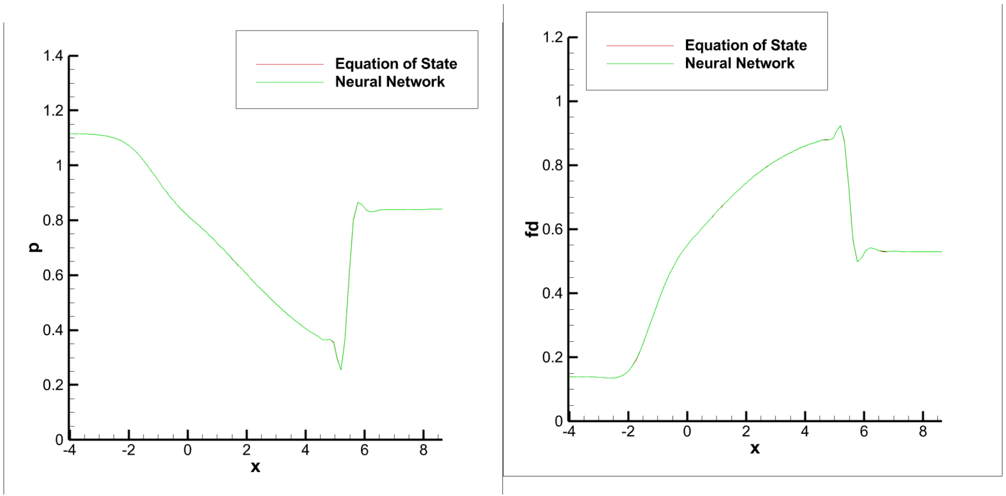

(a) Shock wave case - Pressure

(b) Shock wave case - Fundamental derivative

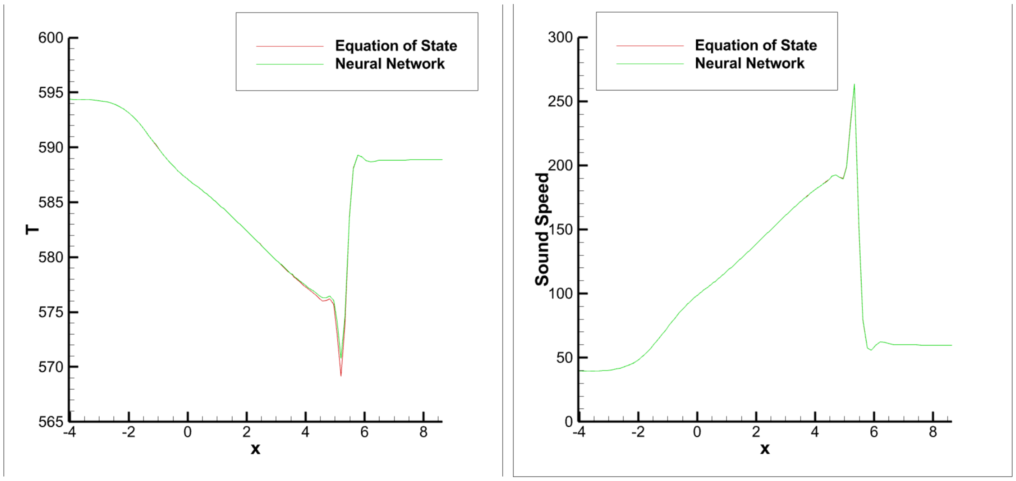

(c) Shock wave case - Temperature

(d) Shock wave case - Speed of sound

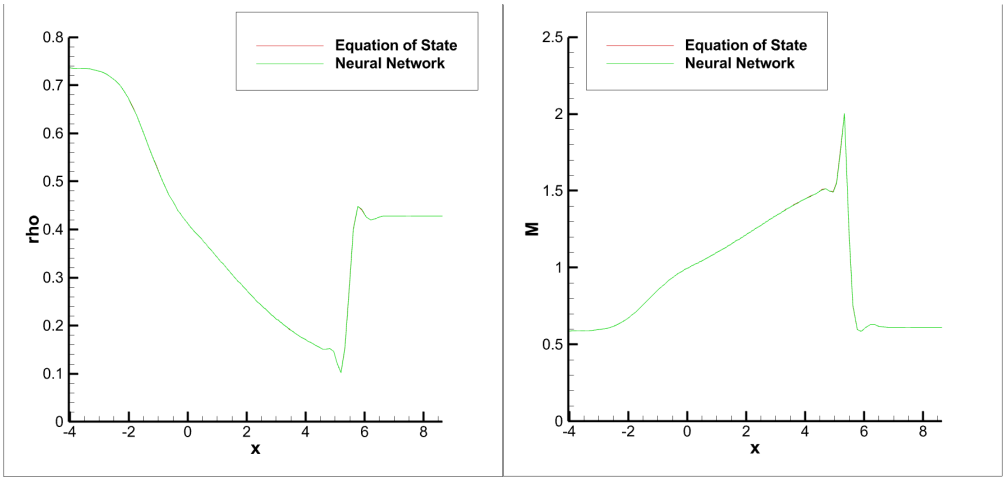

(e) Shock wave case - Density

(f) Shock wave case - Mach number

Figure 4.12: Shock wave case: Flow variable distribution along the nozzle centerline

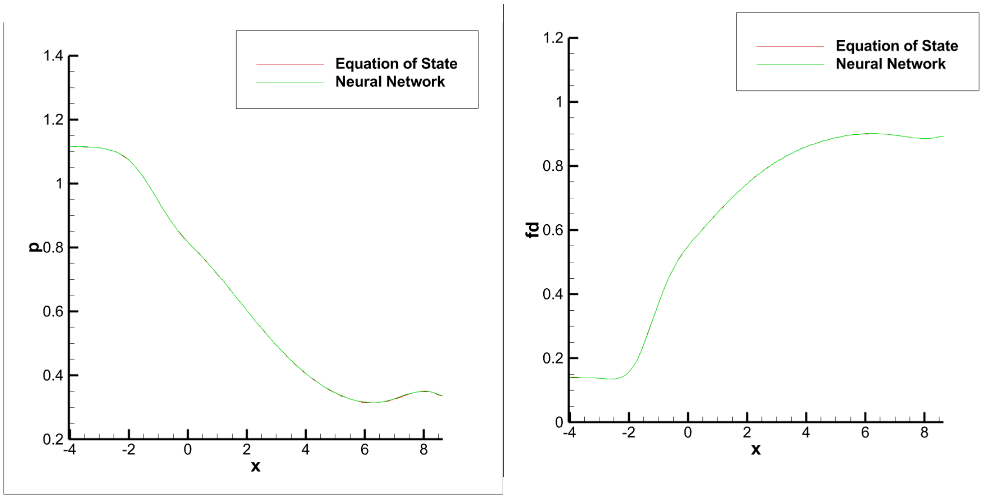

(a) Supersonic case - Pressure

(b) Supersonic case - Fundamental derivative

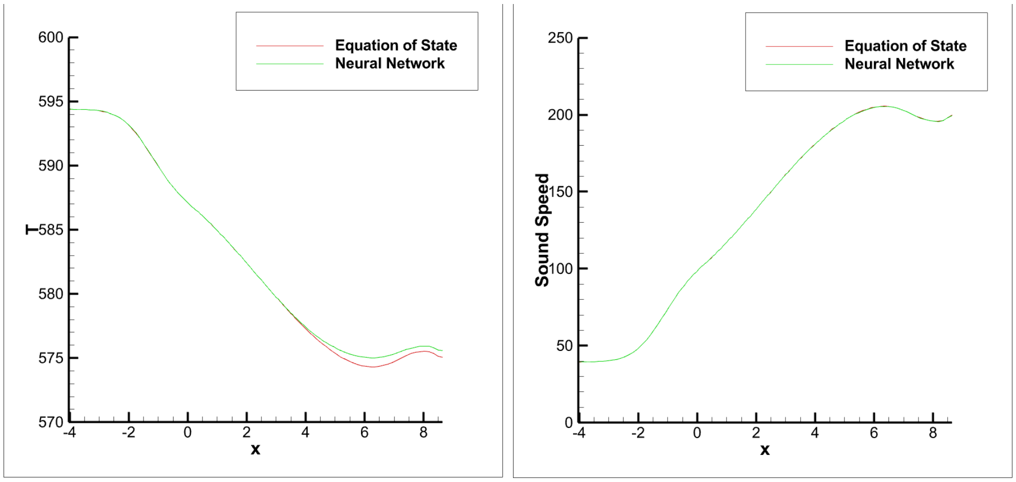

(c) Supersonic case - Temperature

(d) Supersonic case - Speed of sound

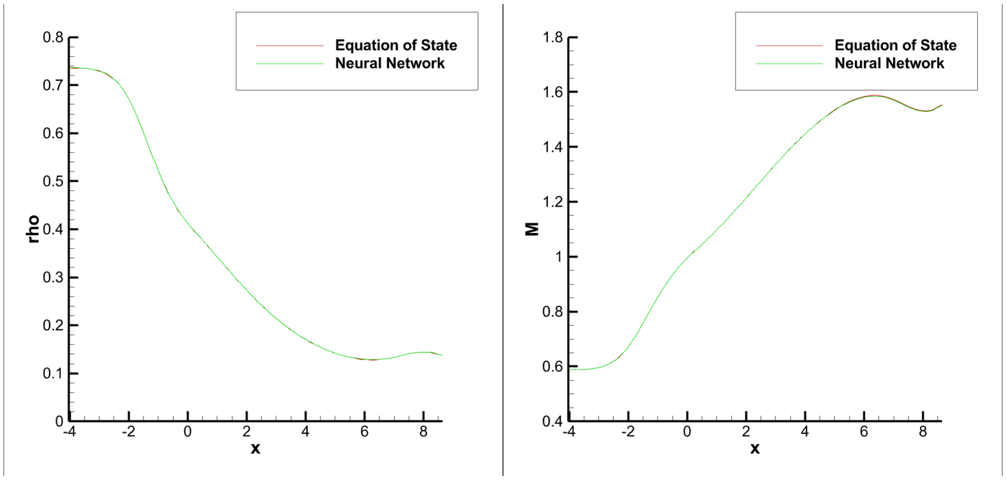

(e) Supersonic case - Density

(f) Supersonic case - Mach number

Figure 4.13: Supersonic case: Flow variable distribution along the nozzle centerline

Chapter 5

Numerical Method for the Navier-Stokes Equations with Non-ideal Dense Gas

The work presented above deals with quasi-one-dimensional flows. To solve more complicated problems, a numerical algorithm to compute the transonic flow of dense gases with the nonclassical BZT gas behavior in two and three dimensions needs to be developed. The plan here is to solve the Navier-Stokes equations using a finite-volume method based on JST or Roe's flux difference splitting scheme. In addition to developing an efficient and robust method to implement the non-ideal-gas Equations of State on an existing Navier-Stokes code, special care must be taken in developing shock-capturing schemes that can accurately capture both the discontinuous compression and expansion shocks that might appear in the same flow field due to the rapid change of Γ of the gas near its critical pressure. A matrice dissipation method incorporating the real-gas effects is proposed in this work to meet this new challenge.

5.1 The Navier-Stokes Equations

The general form of the three-dimensional unsteady compressible Navier-Stokes equations can be expressed as

$$\begin{aligned}\frac{\partial \rho}{\partial t} + \nabla \cdot (\mathbf{V}\rho) &= 0 \\ \frac{\partial (\rho \mathbf{V})}{\partial t} + \nabla \cdot (\mathbf{V}\rho\mathbf{V}) &= -\nabla p + \nabla \cdot \mathbf{S} \\ \frac{\partial (\rho E)}{\partial t} + \nabla \cdot (\mathbf{V}\rho H) &= \nabla \cdot (\mathbf{V} \cdot \mathbf{S}) - \nabla \cdot \mathbf{q}\end{aligned} \tag{5.1}$$

where

$$\mathbf{S} = \mu[\nabla\mathbf{V} + (\nabla\mathbf{V})^T] - \frac{2}{3}\mu(\nabla \cdot \mathbf{V})\mathbf{I} \tag{5.2}$$

$$\mathbf{q} = -\kappa\nabla T \tag{5.3}$$

$$\begin{cases} E = e + \frac{1}{2}\mathbf{V} \cdot \mathbf{V} \\ H = h + \frac{1}{2}\mathbf{V} \cdot \mathbf{V} \end{cases} \tag{5.4}$$

$$h = e + \frac{p}{\rho} \tag{5.5}$$

$$p = p(\rho, T) \tag{5.6}$$

where t is the time, $\mathbf{V}$ is the velocity vector, ρ is the density, p is the pressure, T is the temperature, e is the internal energy, h is the enthalpy, E is the total energy, H is the total enthalpy, $\mathbf{S}$ is the stress tensor, $\mathbf{q}$ is the heat flow vector, μ is the coefficient of dynamic viscosity, and κ is the coefficient of thermal conductivity.

Equation (5.2) comes from the constitutive relationship of Newtonian fluids. Equation (5.3) is Fourier's law. Equation (5.5) is based on the definition of enthalpy and Equation (5.6) depends on the equation of state of the gas.

The Stokes' hypothesis, a critical postulate in fluid mechanics, posits the neglect of bulk viscosity in favor of simplifying mathematical models, as shown in Equation (5.2). This hypothesis stems from the observation that bulk viscosity, which quantifies a fluid's resistance to uniform compression and correlates with energy dissipation due to volumetric change in the fluid, is substantially smaller than shear viscosity for many gases under typical conditions. However, it is important to note that this assumption may not hold in the case of dense gases. Here, the closely spaced molecular arrangement facilitates significant intermolecular interactions, leading to a potential increase in bulk viscosity relative to what would be anticipated in an ideal gas scenario. It is worth emphasizing that the determination of bulk viscosity, in contrast to shear viscosity, necessitates more sophisticated techniques or detailed simulations, rendering the process considerably more challenging. At present, the model opts to disregard bulk viscosity due to the scarcity of pertinent experimental data. However, this is an area that warrants further investigation in future research endeavors.

Another critical factor that requires future reconsideration pertains to the potential non-equilibrium effects in dense gases. Many analyses of ideal gases conventionally presuppose a local thermodynamic equilibrium, where the gas properties are characterized by a single temperature, and the molecular velocities conform to a Maxwellian distribution. Nevertheless, under certain circumstances, dense gases could reside in a non-equilibrium state. In such a state, different energy modes within the gas could manifest disparate timescales. Specifically, in a dense gas or a gas with a complex molecular structure, the vibrational and rotational modes might exhibit significantly protracted relaxation times compared to the translational mode. This implies a more prolonged period for energy to distribute evenly among these modes, which could induce a variety of effects. Currently, for the sake of simplicity and computational ease, these considerations are not incorporated into our research. Nevertheless, as we continue to refine our understanding of these phenomena, it is anticipated that future models will integrate these complexities for a more holistic and accurate representation of the behaviors and properties of dense gases.

Generally, the internal energy is a function of density and temperature, and the enthalpy is a function of pressure and temperature

$$\begin{cases} e & = e(\rho, T) \\ h & = h(p, T) \end{cases} \tag{5.7}$$

and the viscosity coefficient μ and the thermal conductivity coefficient κ are functions of temperature

$$\mu = \mu(T), \qquad \kappa = \kappa(T) \tag{5.8}$$

In order to capture shocks or other discontinuities correctly, the Navier-Stokes equations are usually used in the conservation form. In the three-dimensional Cartesian coordinates (x, y, z), Equation (5.1) can be rewritten as

$$\frac{\partial W}{\partial t} + \frac{\partial f}{\partial x} + \frac{\partial g}{\partial y} + \frac{\partial h}{\partial z} = Q \tag{5.9}$$

where $f = f_c - f_v$, $g = g_c - g_v$, $h = h_c - h_v$.

The conservative variable W is

$$W = \begin{bmatrix} \rho \\ \rho u \\ \rho v \\ \rho w \\ \rho E \end{bmatrix} \tag{5.10}$$

where u, v, and w are the velocity components in the x, y, and z directions, respectively.

For advective flux,

$$f_c = \begin{bmatrix} u\rho \\ u\rho u + p \\ u\rho v \\ u\rho w \\ u\rho E + pu \end{bmatrix}, g_c = \begin{bmatrix} v\rho \\ v\rho u \\ v\rho v + p \\ v\rho w \\ v\rho E + pv \end{bmatrix}, h_c = \begin{bmatrix} w\rho \\ w\rho u \\ w\rho v \\ w\rho w + p \\ w\rho E + pw \end{bmatrix} \tag{5.11}$$

For diffusive flux,

$$f_v = \begin{bmatrix} 0 \\ \tau_{xx} \\ \tau_{xy} \\ \tau_{xz} \\ \sigma_x \end{bmatrix}, g_v = \begin{bmatrix} 0 \\ \tau_{yx} \\ \tau_{yy} \\ \tau_{yz} \\ \sigma_y \end{bmatrix}, h_v = \begin{bmatrix} 0 \\ \tau_{zx} \\ \tau_{zy} \\ \tau_{zz} \\ \sigma_z \end{bmatrix} \tag{5.12}$$

where

$$\begin{aligned} \sigma_x &= (\tau_{xx}u + \tau_{xy}v + \tau_{xz}w) - q_x \\ \sigma_y &= (\tau_{yx}u + \tau_{yy}v + \tau_{yz}w) - q_y \\ \sigma_z &= (\tau_{zx}u + \tau_{zy}v + \tau_{zz}w) - q_z \end{aligned} \tag{5.13}$$

5.2 The Finite-Volume Discretization

Before solving the flow field numerically, the governing equations obtained in section 3.2 need to be transformed into integral-differential equations within the control volume using the finite-volume method. After that, the majority of numerical schemes for solving the Euler and Navier-Stokes equations is to employ a separation discretization in space and time, which allows us to use the numerical approximation of different accuracy for the spatial and temporal derivatives.

The conservative form of Navier-Stokes equations above can be rewritten as

$$\frac{\partial W}{\partial t} + \nabla \cdot F = Q \tag{5.14}$$

where $F = (f_c - f_v, g_c - g_v, h_c - h_v)$.

Integrate Equation (5.14) on arbitrary control volume V to obtain

$$\int_V \frac{\partial W}{\partial t} dV + \int_V \nabla \cdot F dV = \int_V Q dV \tag{5.15}$$

Using Gauss's theorem we can get

$$\frac{\partial}{\partial t} \int_V W dV + \oint_{\partial V} F \cdot n dS = \int_V Q dV \tag{5.16}$$

where n is the normal vector on the control volume surface, and dS is the surface element.

Let $\bar{W}$ represents the average value of W in the control volume V, then $\bar{W} = \frac{1}{V} \int_V W dV$. Equation (5.16) can be rewritten as

$$\frac{d}{dt}(\bar{W} V) = -R \tag{5.17}$$

where R is the residual

$$R = \oint_{\partial V} F \cdot n dS - \int_Q dV \tag{5.18}$$

Equation (5.17) will be discretized using a cell-centered scheme on the structured grids. The so-called cell-centered scheme solves flow variables stored at the centers of the grid cells. A typical hexahedron grid cell in 3-D cases is shown in figure 5.1. This grid cell is labeled as (i, j, k), and the largest node index and smallest node index are (i, j, k) and $(i-1, j-1, k-1)$, respectively. Assuming $V_{i,j,k}$ is the grid cell (i, j, k), $W_{i,j,k}$ is the average value of W in the control volume, Equation (5.17) becomes

$$\frac{d}{dt}(W_{i,j,k}V_{i,j,k}) = -R_{i,j,k} \tag{5.19}$$

where $R_{i,j,k}$ includes the net flux leaving the grid cell surface and the source term, i.e.,

$$R_{i,j,k} = (F^I_{i+1/2,j,k} - F^I_{i-1/2,j,k}) + (F^J_{i,j+1/2,k} - F^J_{i,j-1/2,k}) + (F^K_{i,j,k+1/2} - F^K_{i,j,k-1/2}) - Q_{i,j,k}V_{i,j,k} \tag{5.20}$$

with $F^I_{i+1/2,j,k}$ being the flux at the interface between cell (i, j, k) and $(i + 1, j, k)$

$$F^I_{i+1/2,j,k} = \int_{S_{i+1/2,j,k}} F \cdot ndS = F_{i+1/2,j,k} \cdot S^I_{i+1/2,j,k} \tag{5.21}$$

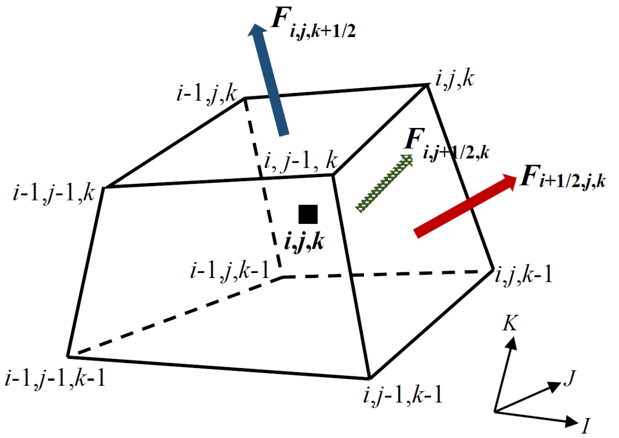

Figure 5.1: hexahedron grid cell in 3-D cases

$S^I_{i+1/2,j,k}$ is the surface normal vector on interface $(i + 1/2, j, k)$

$$S^I_{i+1/2,j,k} = \int_{S_{i+1/2,j,k}} ndS = (S^I_x, S^I_y, S^I_z)_{i+1/2,j,k} \tag{5.22}$$

F is the average of fluxes on the interface $(i+1/2, j, k)$

$$F_{i+1/2,j,k} = (f_c - f_v, g_c - g_v,_c - h_v)_{i+1/2,j,k} \tag{5.23}$$

The fluxes $F^J_{i,j+1/2,k}$ and $F^K_{i,j,k+1/2}$ can be computed in a similar way.

Numerical approximations are not involved in deriving the governing Equations (5.19-5.23). The methods to approximate flux term $F_{1+1/2,j,k}$ in Equation (5.21) are discussed in later sections. Generally, $F_{i+1/2,j,k}$ is reconstructed using the conservative variables $W_{i,j,k}$. The flux term $F^I_{i+1/2}$ includes two parts, convective fluxes and diffusive fluxes

$$F^I_{i+1/2} = F^I_{c,i+1/2} - F^I_{v,i+1/2} \tag{5.24}$$

where

$$\begin{aligned}
F^I_{c,i+1/2} &= f_{c,i+1/2} S^I_{x,i+1/2} + g_{c,i+1/2} S^I_{y,i+1/2} + h_{c,i+1/2} S^I_{z,i+1/2} \\
F^I_{v,i+1/2} &= f_{v,i+1/2} S^I_{x,i+1/2} + g_{v,i+1/2} S^I_{y,i+1/2} + h_{v,i+1/2} S^I_{z,i+1/2}
\end{aligned} \tag{5.25}$$

Due to the different physical properties between convective fluxes and diffusive fluxes, they will be separate.

5.3 Jacobian matrix for real gases

To include the real-gas effects, the Jacobian matrix will be different from the ideal-gas case. For the sake of simplicity, the 1D case will be presented without loss of generality for extensions to a higher dimension. The Euler equations in 1D can be written in the conservative form as

$$\frac{\partial W}{\partial t} + \frac{\partial F(W)}{\partial x} = 0 \tag{5.26}$$

where W is the conservative variable

$$W = \begin{pmatrix} \rho \\ \rho u \\ \rho E \end{pmatrix} = \begin{pmatrix} W_1 \\ W_2 \\ W_3 \end{pmatrix} \tag{5.27}$$

and F is the flux

$$F = \begin{pmatrix} \rho u \\ \rho u^2 + P \\ \rho u(E + \frac{P}{\rho}) \end{pmatrix} = \begin{pmatrix} W_1 \\ \frac{W_2^2}{W_1} + P \\ \frac{W_2 W_3}{W_1} + P\frac{W_2}{W_1} \end{pmatrix} \tag{5.28}$$

Then the Jacobian matrix A is

$$A = \frac{\partial F}{\partial W} = \begin{bmatrix} 0 & 1 & 0 \\ -\frac{W_2^2}{W_1^2} + \frac{\partial P}{\partial W_1} & 2\frac{W_2}{W_1} + \frac{\partial P}{\partial W_2} & \frac{\partial P}{\partial W_3} \\ -\gamma\frac{W_2 W_3}{W_1^2} + \frac{\partial P}{\partial W_1}\frac{W_2}{W_1} - P\frac{W_2}{W_1^2} & \frac{W_3}{W_1} + \frac{\partial P}{\partial W_2}\frac{W_2}{W_1} + \frac{P}{W_1} & \frac{W_2}{W_1} + \frac{\partial P}{\partial W_3}\frac{W_2}{W_1} \end{bmatrix} \tag{5.29}$$

To keep consistency with Chapter 2, here the Van der Waals equation is used for the partial derivatives.

$$P = \frac{RT}{v - b} - \frac{a}{v^2} \tag{5.30}$$

$$e = c_v T - \frac{a}{v}$$

Rewrite Equation.(5.30) in the form of pressure and internal energy

$$P = \frac{\rho\delta(e + a\rho)}{1 - b\rho} - a\rho^2 \tag{5.31}$$

where

$$\delta = \frac{R}{c_v}$$

Two useful partial derivatives are

$$P_\rho = \left(\frac{\partial P}{\partial \rho}\right)_e = \frac{(\delta e + 2a\rho)(1 - b\rho) + b(\delta e\rho + a\delta\rho^2)}{(1 - b\rho)^2} - 2a\rho \tag{5.32}$$

$$P_e = \left(\frac{\partial P}{\partial e}\right)_\rho = \frac{\rho\delta}{1 - b\rho} \tag{5.33}$$

Rearrange Equation. (5.29) to get the Jacobian matrix for Van der Waals gas

$$A = \frac{\partial F}{\partial W} = \begin{bmatrix} 0 & 1 & 0 \\ u^2(\frac{P_e}{2\rho} - 1) + P_\rho - \frac{P_e e}{\rho} & 2u - \frac{uP_e}{\rho} & \frac{P_e}{\rho} \\ u\left[P_\rho - \frac{P}{\rho} - \frac{u^2}{2}\left(1 - \frac{P_e}{\rho}\right) - e\left(1 + \frac{P_e}{\rho}\right)\right] & \frac{P}{\rho} + e + \frac{u^2}{2}\left(1 - \frac{P_e}{\rho}\right) & u + \frac{uP_e}{\rho} \end{bmatrix} \tag{5.34}$$

The eigenvalues and eigenvectors of this matrix are determined by using Mathematica.

Eigenvalues:

$$\lambda_1 = u + c, \quad \lambda_2 = u - c, \quad \lambda_3 = u \tag{5.35}$$

Eigenvectors:

$$\begin{aligned} \vec{e}_1 &= [1, u + c, H + uc]^T \\ \vec{e}_2 &= [1, u - c, H - uc]^T \\ \vec{e}_3 &= [1, u, H - \frac{c^2\rho}{P_e}]^T \end{aligned} \tag{5.36}$$

where

$$
\begin{aligned}
H &= \frac{P}{\rho} + E = \frac{P}{\rho} + e + \frac{1}{2}u^2 \\
c^2 &= \frac{PP_e}{\rho^2} + P_\rho
\end{aligned}
$$

Note that in Equations 5.32 and 5.33, both “a” and “b” are considered as constants. However, for some more nuanced and complex models of a real gas, “a” and “b” are considered as variables depending on the pressure and temperature. Under such scenarios, the variation of “a” could reflect changes in the strength of the intermolecular forces with changing conditions, and the variation of “b” will reflect changes in the effective size of the gas molecules. For instance, at very high pressures or very low temperatures, the intermolecular forces may become more prominent, so ’a’ might increase; but the molecules might be compressed such that the effective volume they occupy (’b’) decreases. However, in reality, such models can become extremely complex and may not provide significantly better predictions than simpler models like the van der Waals model. As a result, more complex models tend to be used only when necessary for a specific level of precision or under certain conditions where simpler models fail.

5.4 Matrix Dissipation for the JST Scheme

Central difference schemes are widely applied for solving the Euler or Navier-Stokes equations. The central difference scheme was proposed by Jameson, Schmidt, and Turkel [128] in 1981, and is also known as the JST scheme, according to the authors’ names. The basic idea of the central difference scheme is that the convection flux at the control volume interface is calculated from the arithmetic mean of the conserved variables of two adjacent grid cells. However, simple center discretization will lead to odd-even decoupling and nonphysical oscillations near the shock wave. Hence, to stabilize the numerical scheme to reach a steady state, the artificial viscosity was introduced in the central difference scheme to improve its stability.

Obviously, the real-gas effect increases the complexity of numerical computation. So the matrix dissipation scheme is used to reduce the amount of added artificial viscosity. Here the 2D case for ideal-gas calculation is given as an example.

The 2D JST scheme is presented below:

$$\frac{d}{dt}(V_{ij}W_{ij}) + R_{ij} = 0 \tag{5.37}$$

where V_{ij} is the cell volume, W_{ij} is the conservative flow variable, R_{ij} is the finite volume approximation for the net flux out of the cell.

The numerical approximation to the flux F at the cell interface is split into two parts. The j direction component is given as

$$R_{j+\frac{1}{2}} = h_{j+\frac{1}{2}} - d_{j+\frac{1}{2}} \tag{5.38}$$

The first term on the RHS is a second-order approximation to F

$$h_{j+\frac{1}{2}} = \frac{F(W_{j+1}) + F(W_{j-1})}{2} \tag{5.39}$$

The second term is the artificial dissipation term

$$d_{j+\frac{1}{2}} = \epsilon^{(2)}_{j+\frac{1}{2}} \Lambda_{j+\frac{1}{2}} \Delta W_{j+\frac{1}{2}} - \epsilon^{(4)}_{j+\frac{1}{2}} \Lambda_{j+\frac{1}{2}} \Delta^3 W_{j+\frac{1}{2}} \tag{5.40}$$

where

$$\Delta W_{j+\frac{1}{2}} = W_{j+1} - W_j$$
$$\Delta^3 W_{j+\frac{1}{2}} = W_{j+2} - 3W_{j+1} + 3W_j - W_{j-1}$$

$\epsilon^{(2)}_{j+\frac{1}{2}}$ and $\epsilon^{(4)}_{j+\frac{1}{2}}$ are related with the pressure sensor

$$\upsilon_j = \left| \frac{p_{j+1} - 2p_j + p_{j-1}}{p_{j+1} - 2p_j + p_{j-1}} \right| \tag{5.41}$$

$$S_{j+\frac{1}{2}} = max(\upsilon_{j+1}, \upsilon_j) \tag{5.42}$$

$$\epsilon^{(2)}_{j+\frac{1}{2}} = min(\alpha_1, \alpha_2 S_{j+\frac{1}{2}}) \tag{5.43}$$

$$\epsilon^{(4)}_{j+\frac{1}{2}} = max(0, \beta_1 - \beta_2 \epsilon^{(2)}_{j+\frac{1}{2}}) \tag{5.44}$$

$\Lambda_{j+\frac{1}{2}}$ is the maximum wave speed of the system. For the Euler equations,

$$\Lambda_{j+\frac{1}{2}} = |\vec{v}| + c \tag{5.45}$$

A matrix dissipation model can easily be constructed based on the JST scheme. The flux Jacobian matrix is used instead of using the eigenvalue scaling factor Λ.

In the Euler equations for real gas, the conservative variable and flux are given as

$$W = \begin{bmatrix} \rho \\ \rho u \\ \rho v \\ \rho E \end{bmatrix}$$

$$F = \begin{bmatrix} \rho \vec{v} \\ \rho u \vec{v} + n_x p \\ \rho v \vec{v} + n_y p \\ \rho H \vec{v} \end{bmatrix}$$

where the flux vector can be rewritten in terms of the conservation variables as

$$F = \begin{bmatrix} W_2 n_x + W_3 n_y \\ \frac{W_2^2}{W_1} n_x + \frac{W_2 W_3}{W_1} n_y + p n_x \\ \frac{W_2 W_3}{W_1} n_x + \frac{W_3^2}{W_1} n_y + p n_y \\ (\frac{W_4 + p}{W_1})(W_2 n_x + W_3 n_y) \end{bmatrix}$$

Then, the Jacobian matrix $A = \frac{\partial F}{\partial W}$ is given as

$$A = \frac{\partial F}{\partial W} = \begin{bmatrix} 0 & n_x & n_y & 0 \\ (-a_1^2 + b_1) n_x + a_1 a_2 n_y & (2a_1 + b_2) n_x + a_2 n_y & b_3 n_x + a_1 n_y & b_4 n_x \\ -a_1 a_2 n_x + (-a_2^2 + b_1) n_y & a_2 n_x + b_2 n_y & a_1 n_x + (2a_2 + b_3) n_y & b_4 n_y \\ (-a_3 + b_1)\phi & (a_3 + a_1 b_2) n_x + a_2 b_2 n_y & a_1 b_3 n_x + (a_3 + a_2 b_3) n_y & (b_4 + 1)\phi \end{bmatrix} \tag{5.46}$$

where

$$a_1 = \frac{W_2}{W_1} \qquad a_2 = \frac{W_3}{W_1} \qquad a_3 = \frac{W_4 + p}{W_1}$$

$$b_1 = \frac{\partial p}{\partial W_1} \qquad b_2 = \frac{\partial p}{\partial W_2} \qquad b_3 = \frac{\partial p}{\partial W_3} \qquad b_4 = \frac{\partial p}{\partial W_4}$$

$$\phi = (a_1 n_x + a_2 n_y)$$

The eigenvalues of A are readily determined.

$$\lambda_{1,2} = \vec{v} \qquad \lambda_3 = \vec{v} + c \qquad \lambda_4 = \vec{v} - c \tag{5.47}$$

Since the Euler equations are a strongly hyperbolic system, the matrix A can be diagonalized as

$$A = P^{-1} \Lambda P \tag{5.48}$$

where P^{-1} represent the matrix of the right eigenvectors and P is the matrix of the left eigenvectors of A.

The diagonal matrix is given by

$$\Lambda = \begin{bmatrix} \vec{v} & 0 & 0 & 0 \\ 0 & \vec{v} & 0 & 0 \\ 0 & 0 & \vec{v} + c & 0 \\ 0 & 0 & 0 & \vec{v} - c \end{bmatrix} \tag{5.49}$$

Now $|A|$ is define as

$$|A| = P^{-1} |\Lambda| P$$

where

$$|\Lambda| = diag(|\lambda_1|, |\lambda_2|, |\lambda_3|, |\lambda_4|)$$

Instead of the scaling factor in the original JST scheme, matrix $|A|$ is used in the artificial dissipation terms as follows

$$d_{j+\frac{1}{2}} = \epsilon^{(2)}_{j+\frac{1}{2}} |A|_{j+\frac{1}{2}} \Delta W_{j+\frac{1}{2}} - \epsilon^{(4)}_{j+\frac{1}{2}} |A|_{j+\frac{1}{2}} \Delta^3 W_{j+\frac{1}{2}} \tag{5.50}$$

5.5 Simulation Results

5.5.1 Shock Tube

The shock tube problem, often known as the Riemann problem, presents a nice example where flow is established by the action of shock waves and expansion waves. It is a classic fluid dynamics and computational fluid dynamics problem used to evaluate numerical algorithms. Shock tubes have also been used to supply supersonic and hypersonic wind tunnels with high-pressure and high-temperature gas. Figure 5.2a depicts the structure and corresponding initial condition of a shock tube, which comprises a driven section with pressure p_1 and a driver section with pressure $p_4 > p_1$. These two sections are separated by a diaphragm which is suddenly pulled out and the gases are then free to flow from the driver section to the driven section.

The shock tube problem for an ideal gas has been widely explored computationally and experimentally. As shown in Figure 5.2b, when the diaphragm is removed, it generates a shock wave and a contact surface that propagate toward the driven side and an expansion wave that travels toward the driver side. The contact surface cannot sustain velocity and pressure discontinuities, however, it may support a discontinuity in temperature and density.

For a nonclassical gas, the solution of a shock tube problem may exhibit a complicated wave field after removing the diaphragm. The wave structure is very sensitive to the value of Γ and the initial condition of the shock tube. Two examples of the nonclassical wave phenomena in a shock tube are shown below. The initial condition is kept the same as the ideal-gas case shown in Figure 5.2a, with the density and pressure value for both sections listed in Table 5.1. In each scenario, the p-v diagram and x-t diagram depict the flow development. In Table 5.1, “ES” represents expansion shock, “EF” represents expansion fan, “CS” represents compression shock, and “CF” represents compression fan. The initial condition for the high-

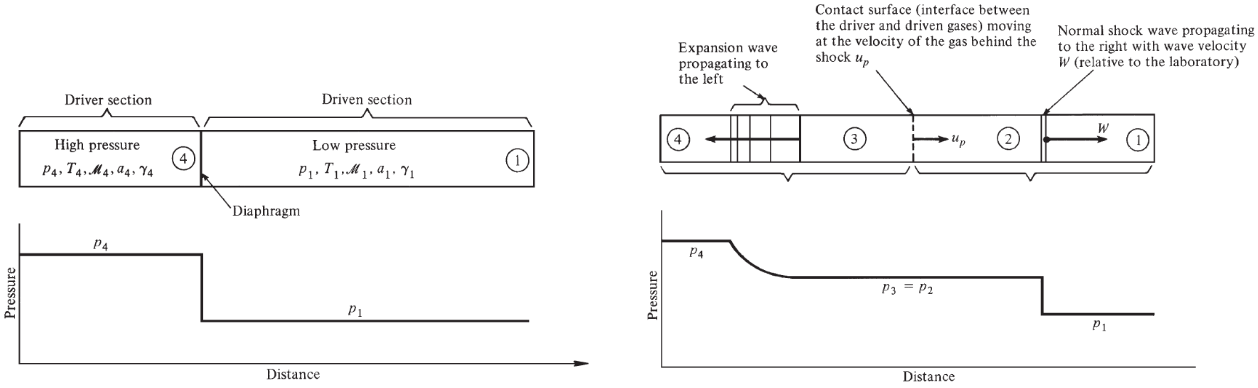

(a) Initial condition (b) Flow after the diaphragm is broken

Figure 5.2: Pressure-driven shock tube problem[3]

pressure section remains the same for both cases, whereas Case 1 has the initial condition for the low pressure section located in the $\Gamma < 0$ region and Case 2 in the $0 < \Gamma < 1$ region.

Table 5.1: Dense gas cases

	ρ_L	P_L	Γ_L	Wave Structure	ρ_R	P_R	Γ_R	Wave Structure
Case1	0.879	1.09	-0.0031	ES	0.562	0.885	-4.016	CF
Case2	0.879	1.09	-0.0031	ES+EF	0.275	0.575	0.703	CS

Case 1 is a typical nonclassical behavior since the initial states belong entirely to the region with $\Gamma < 0$ and it remains in this region in the whole flow field without crossing the boundary of $\Gamma = 0$. Figure 5.3a shows that both state 1 and state 4 are located inside the region of $\Gamma < 0$. Figure 5.3b shows that an expansion shock propagates into the high-pressure fluid with shock speed $u_s = 32\ m/s$. The compression fan is propagating to the right with the leading edge and trailing edge located at $x = 0.9\ m$ and $x = 0.81\ m$ respectively as shown in Figure 5.3c. The contact surface is located between the expansion shock and compression fan at $x = 0.6\ m$ and is propagating to the right. The contact surface in Figure 5.3b is not very sharp because of the artificial dissipation of the central scheme.

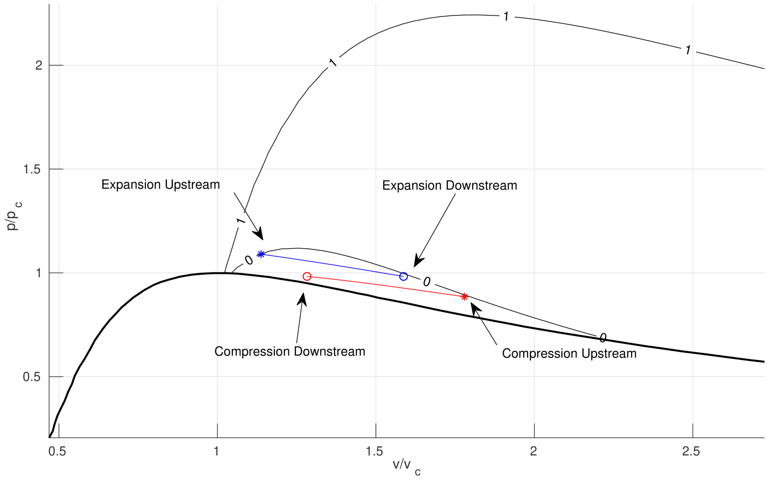

(a) p-v diagram

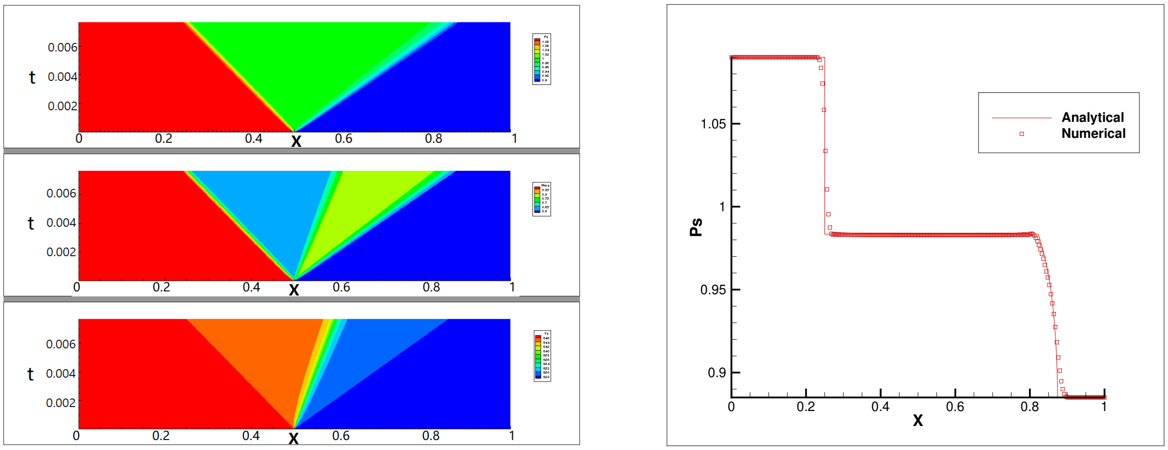

(b) x-t diagram (P, ρ, T)

(c) Pressure distribution

Figure 5.3: Case 1: Expansion Shock / Compression Fan

For Case 2, the initial condition for the high-pressure fluid is located in the region of $\Gamma < 0$ but the low-pressure fluid is located in the region of $\Gamma > 0$ as shown in Figure 5.4a. A mixed wave phenomenon is observed in Case 2. The boundary of $\Gamma = 0$ is crossed during the flow evolution. At $x = 0.81m$, a compression shock is propagating into the low-pressure fluid. The expansion shock is propagating to the left followed by a set of expansion fans with the leading edge at $x = 0.41m$. In computational results, it is very hard to capture the exact location where the shock is split into a set of fans because the shock wave is also represented by a set of discrete points rather than a very sharp discontinuity. In Figure 5.4c, it can be seen that more grid points appear after $x = 0.41$; this is also observed in the density distribution in Figure 5.4d. It indicates the location where the expansion shock collides with the leading edge of the expansion fan. This is later confirmed by the analytical results. Note that, at this point, the fluid is already in the region of $\Gamma > 0$; this indicates the transition from expansion shock to expansion fan does not occur within the $\Gamma \leq 0$ region. The high-pressure fluid in the nonclassical region is first expanded by an expansion shock into the region of $\Gamma > 0$; then, it is further expanded by a continuous expansion fan. The left-running wave speed $u - c$ is shown in Figure 5.4e, the expansion shock speed is propagating to the left at a speed of $29.2 m/s$ and the wave in front of the shock wave is propagating at a lower speed. The left-running waves must be faster than the wave behind the shock, but it slows down as it goes through the expansion fan. This behavior is shown by the sharp dip and gradual rise of the $u - c$ plot near $x = 0.4$ in Figure 5.4e. Upon crossing the contact surface, the speed of the left-running wave escalates further. Another point to note is the disparity in sound speed between the left (compressed air) and right side, with the former being slower. This is in alignment with the gas behavior outlined in Table 2.4.

5.5.2 Corner Flow

Supersonic flows over corner geometries provide important predictions of realistic flow phenomena in aerodynamics. For gas in the classical region, an oblique shock occurs when a supersonic flow is turned in by a compression corner. In contrast, an expansion wave is formed when a supersonic flow is turned away by an expansion corner, flow properties change smoothly through the expansion fan and entropy remains constant.

For a given incoming flow Mach number, the deflection angle and oblique shock angle of the flow over a compression corner can be determined by the $\theta - \beta - M$ relation [3]

$$\tan\theta = 2\cot\beta \left[\frac{M_1^2 \sin^2\beta - 1}{M_1^2(\gamma + \cos 2\beta) + 2} \right] \tag{5.51}$$

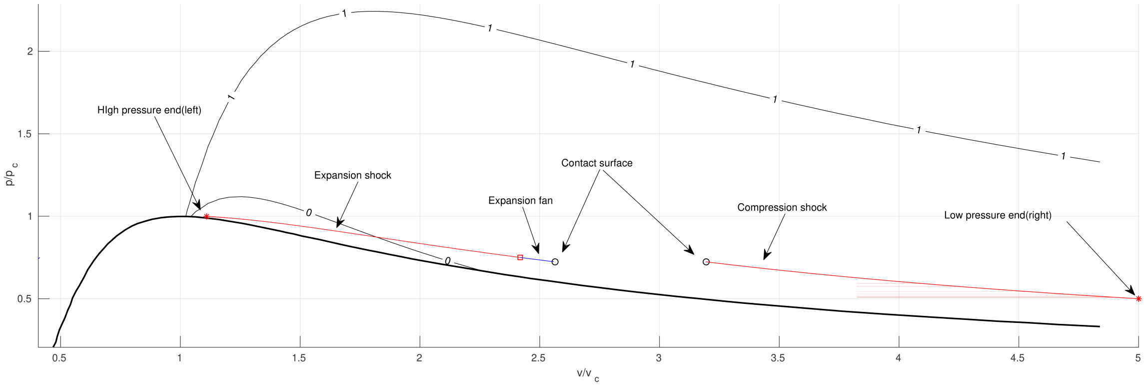

(a) p-v diagram

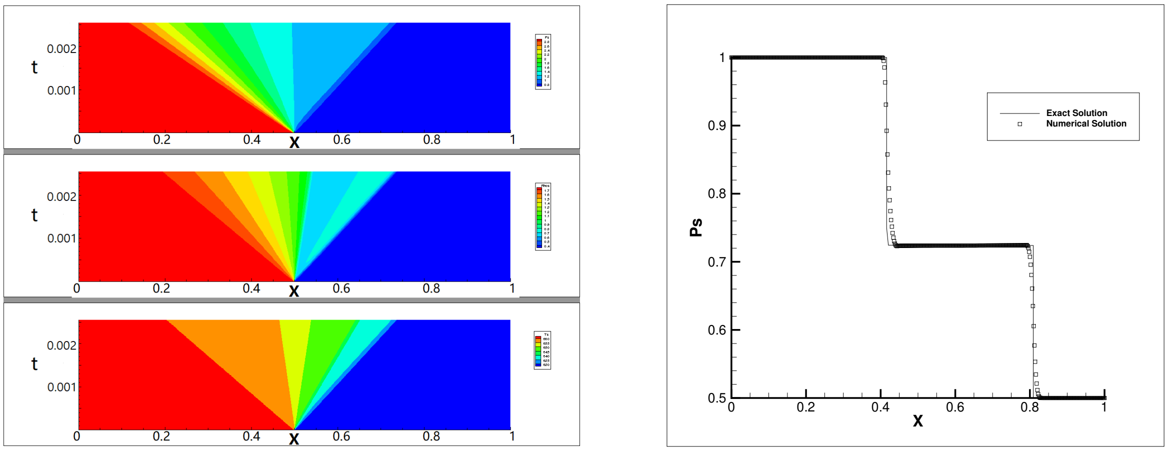

(b) x-t diagram (P, ρ, T)

(c) Pressure distribution

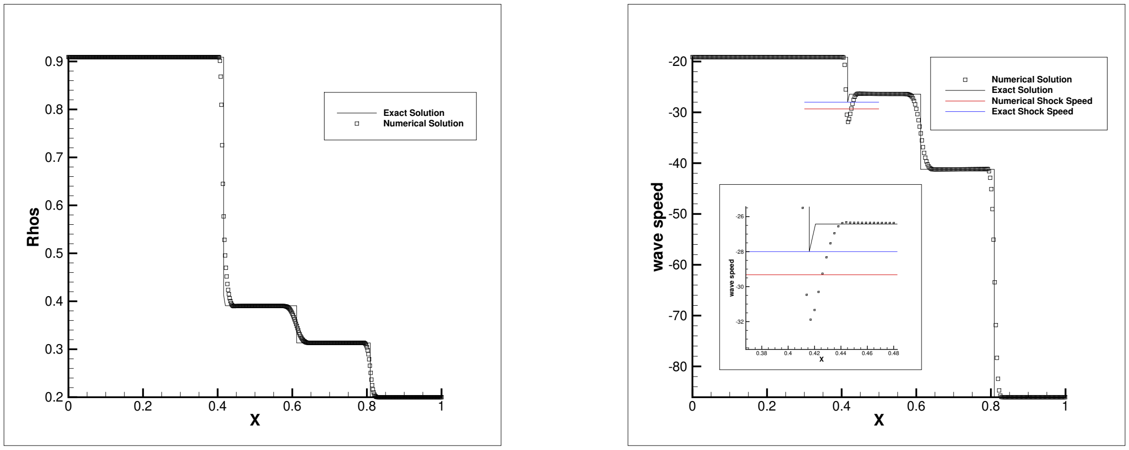

(d) Density distribution

(e) Left-running wave speed

Figure 5.4: Case 2: Expansion Shock + Expansion Fan / Compression Shock

where M_1 is the Mach number of the incoming flow, β is the oblique shock angle and θ is the deflection angle.

In contrast to classical gas, the wave fields are much more complex as discussed previously. The gas behavior over compression and expansion corners can no longer be predicted by classical gas theory. To understand nonclassical supersonic flow behavior over corner geometries, numerical simulations are performed using supersonic MDM flow for both classical and nonclassical cases.

Expansion Corner

The initial conditions for the expansion corner cases are in Table 5.2. Pressure p and the specific volume v are normalized by the critical-point values. A 600 × 600 mesh is used. C represents a classical gas case with the initial condition in the region $0 < \Gamma < 1$. NC represents the nonclassical gas case with the initial condition in the region $\Gamma < 0$.

Table 5.2: Initial conditions for the flow over an expansion corner

Case	$\frac{p}{p_c}$	$\frac{v}{v_c}$	Γ	M	Deflection δ
NC1	1	1.3	-0.915	3.21618484	-7^o
C1	1.2	1.7	0.558	3.21618484	-7^o

Figure 5.5 shows the solutions for cases C1 and NC1. In NC1, the upstream state was selected to generate a nonclassical expansion shock wave. The geometry consists of a simple domain containing a corner with slope $\theta = -7^o$. Figures 5.5c - 5.5d report the normalized entropy difference ds/R for both C1 and NC1. In C1, the flow recovers classical gas behavior and an expansion fan develops over the corner. The flow expands smoothly across the expansion fan and the fluid stays in the classical region both before and after the expansion fan. In contrast, an expansion shock can be observed in Figures 5.5b, 5.5d, and 5.5f for NC1. This non-negligible discontinuity separates the domain into two uniform regions. Mach number decreases across the shock. The fundamental derivative increases from negative to positive across the shock, which indicates that flow can jump from the nonclassical region to the classical region through an expansion shock. At the same time, a pressure drop and an

entropy increase are observed across the discontinuity as revealed in Figure 5.6, which further confirmed this is a nonclassical expansion shock.

Figure 5.6 compare the computed entropy and pressure on the corner surface with analytical results. The solid black line represents the analytical solution and the red squares represent the numerical solution. Overall, the numerical solution agrees with the analytical solution except for some entropy oscillation after the expansion shock. Future work is needed to improve the numerical scheme to reduce the oscillatory behavior across sharp discontinuities.

Compression Corner

The initial conditions of flow over a compression corner are given in Table 5.3. The geometry consists of a simple domain with a 10^o compression corner. The classical and nonclassical gas flow fields are compared.

Table 5.3: Initial conditions for the flow over a compression corner

Case	$\frac{p}{p_c}$	$\frac{v}{v_c}$	Γ	M	Deflection δ
C2	0.9	2.5	0.662	1.3	10^o
NC2	0.9	1.6	-0.476	1.3	10^o

The free-stream state is chosen such that $\Gamma > 0$ for case C2 and $\Gamma < 0$ for case NC2. Free-stream Mach number is 1.4 for C2 and 1.3 for NC2. Figure 5.7a - 5.7b compare the pressure fields between C2 and NC2. An oblique compression shock attached to the corner is shown in figure 5.7a. An entropy jump can be observed in the entropy contour (see Figure 5.7c). Figure 5.7b shows that flow is compressed smoothly through a compression fan centered at the corner. The entropy contour in Figure 5.7d confirms that the compression process in NC2 is completely isentropic. This agrees with the theory for nonclassical gas as discussed earlier.

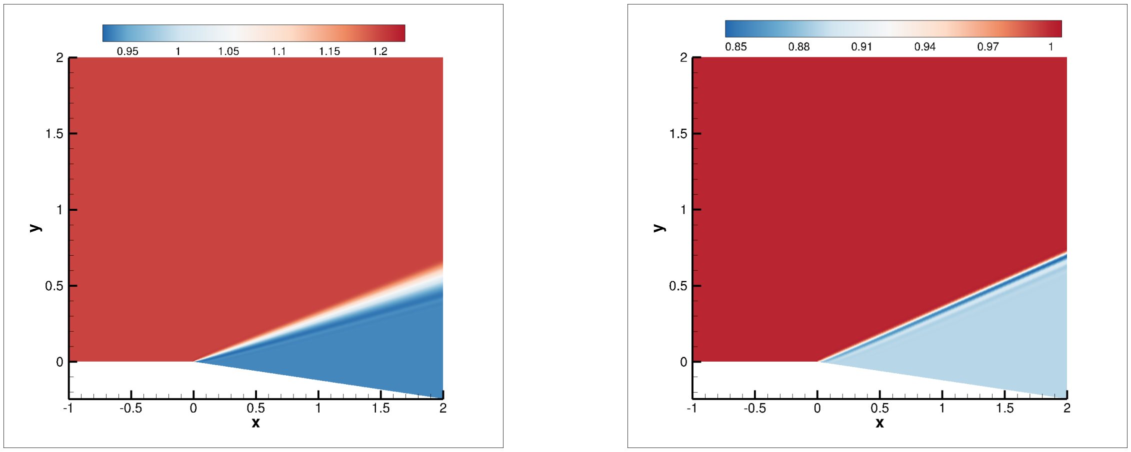

(a) C1: Pressure, p/p_c

(b) NC1: Pressure, p/p_c

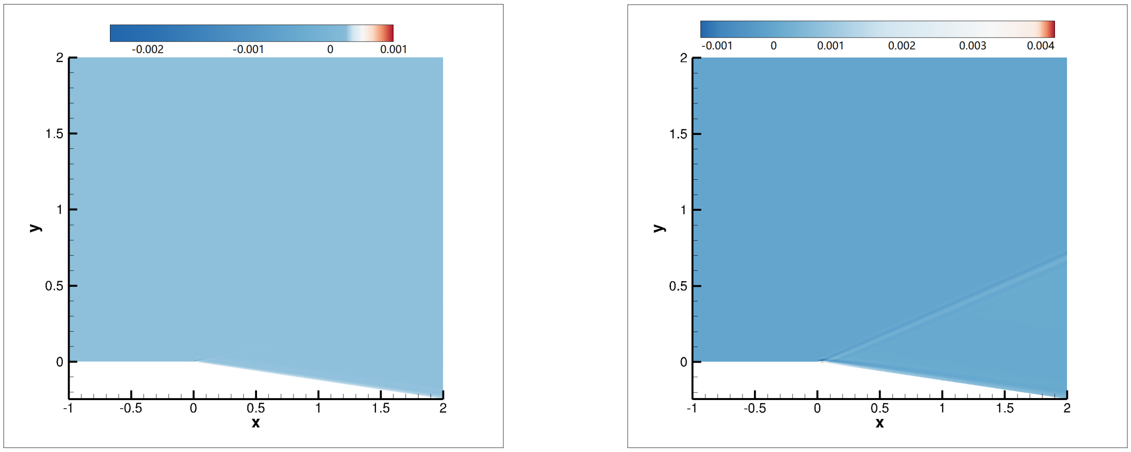

(c) C1:Entropy, $\Delta s/R$

(d) NC1:Entropy, $\Delta s/R$

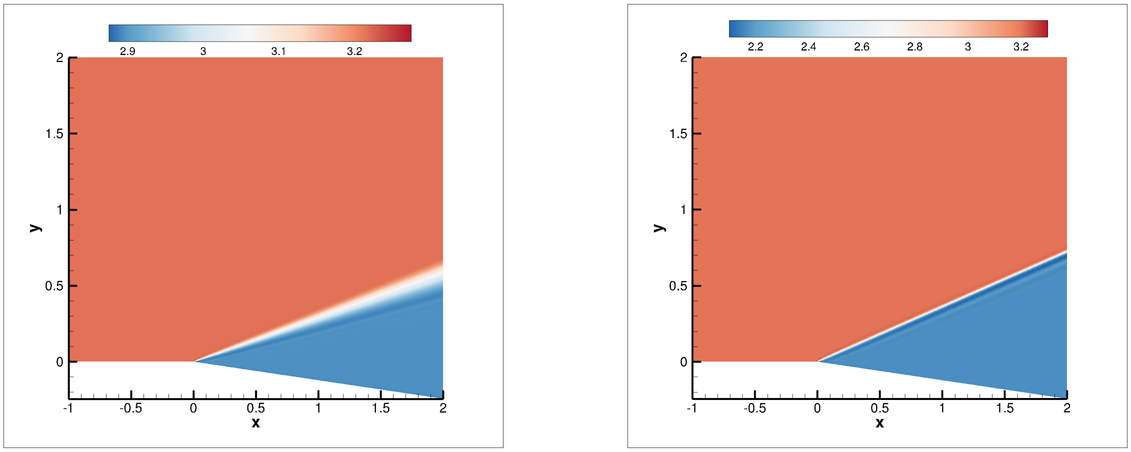

(e) C1: Mach number, M

(f) NC1: Mach number, M

Figure 5.5: Flow field of expansion corner C1/NC1

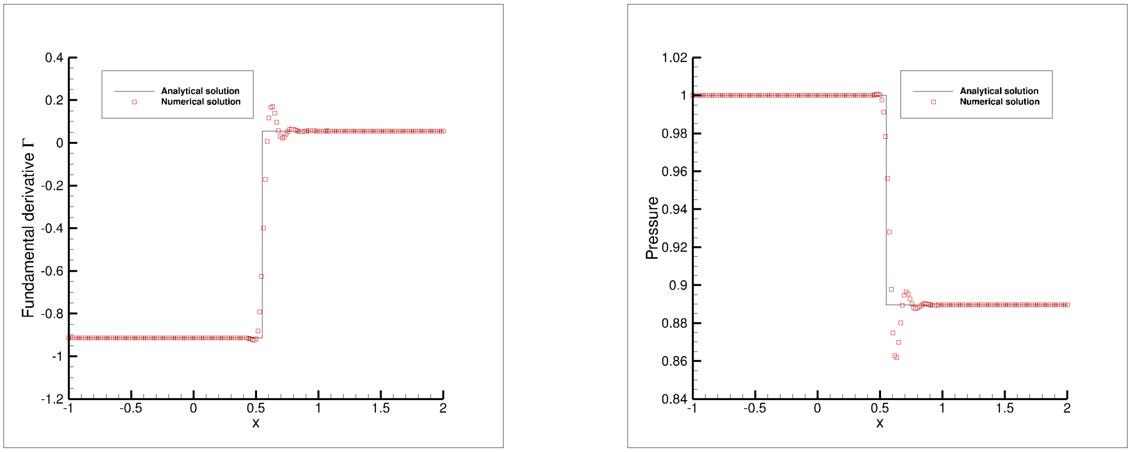

(a) Fundamental Derivative, Γ (b) Pressure, p/p_c

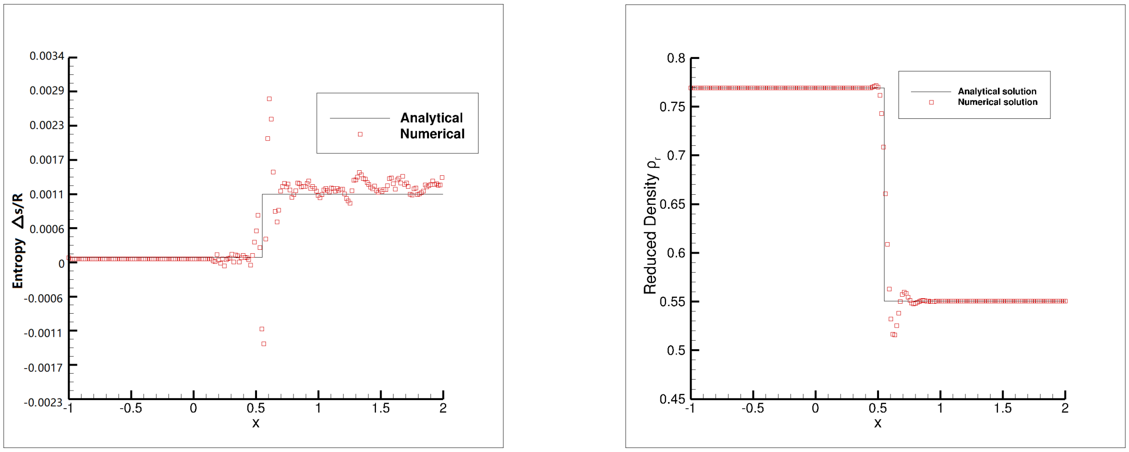

(c) Entropy, $\Delta s/R$ (d) Reduced Density, ρ/ρ_c

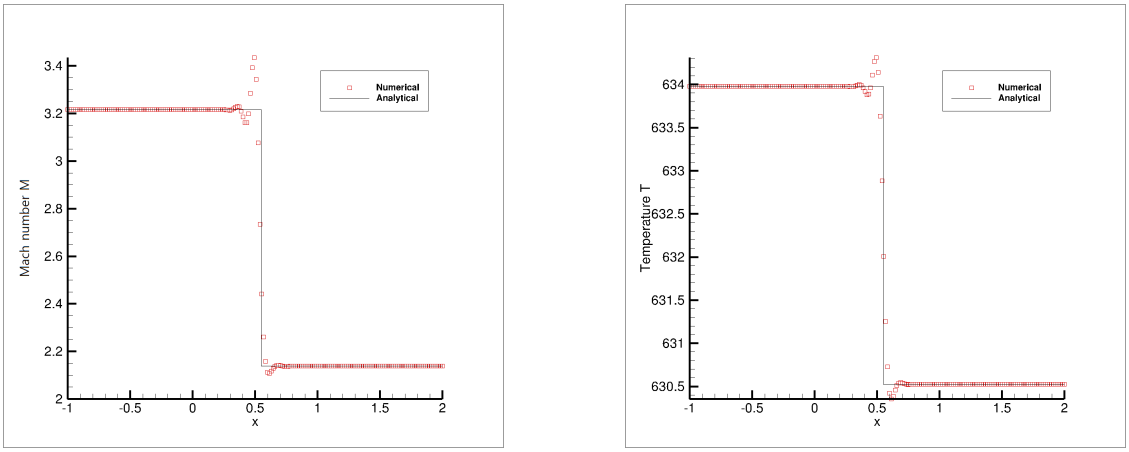

(e) Mach number, M (f) Temperature, T

Figure 5.6: Flow variable distribution at $y = 0.2$ for expansion corner NC1

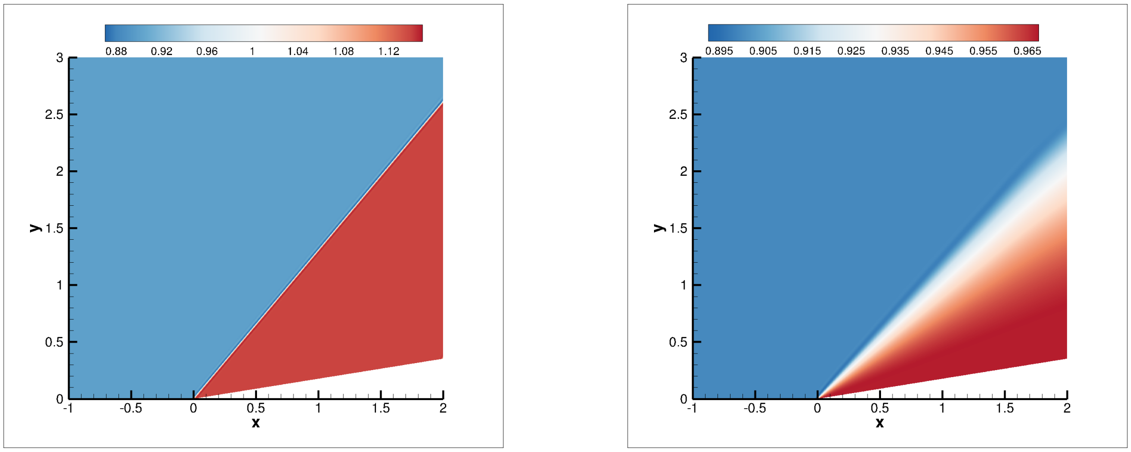

(a) C1: Pressure, p/p_c (b) NC1: Pressure, p/p_c

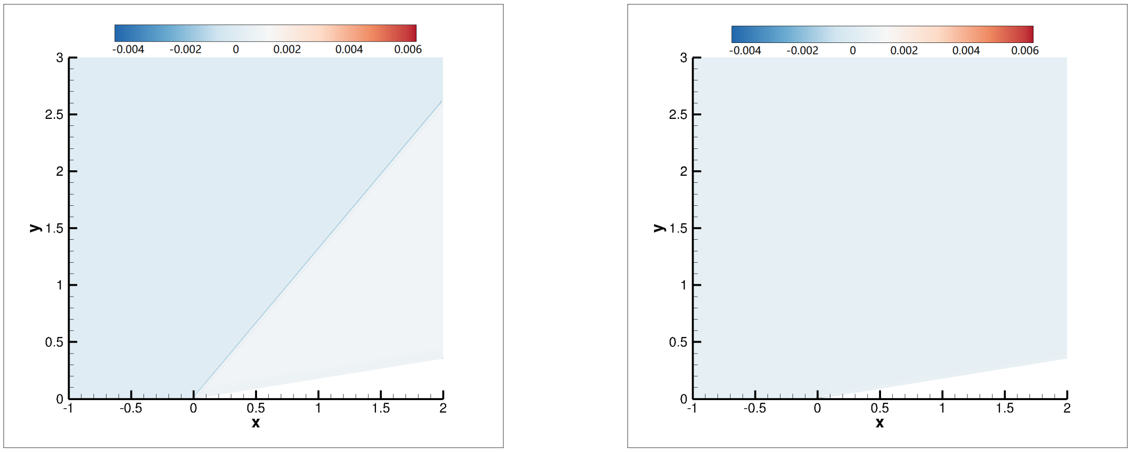

(c) C1: Entropy, $\Delta s/R$ (d) NC1: Entropy, $\Delta s/R$

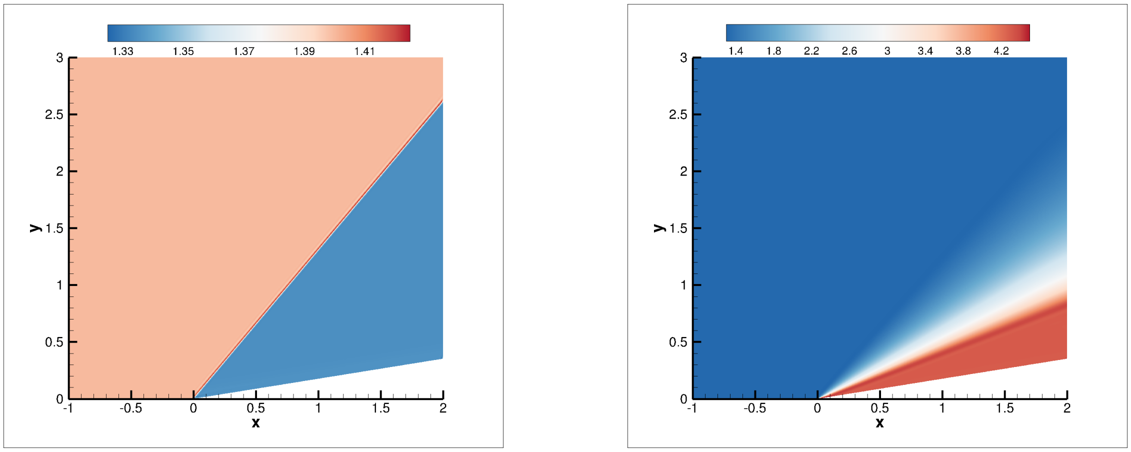

(e) C1: Mach number, M (f) NC1: Mach numbe, M

Figure 5.7: Flow field of compression corner C2/NC2

Chapter 6

Pressure-based Solution Method for Compressible Flow

Compressible flow analysis is indispensable in a variety of engineering disciplines, including aeronautics, turbomachinery, and propulsion systems, among others. Accurate simulation of compressible flow is vital for the rigorous examination and design of intricate systems. In the field of Computational Fluid Dynamics, the selection of a suitable solver is crucial for attaining reliable results. There are two primary categories of solvers utilized in CFD, pressure-based and density-based solvers. The suitability of a particular solver depends on the nature of the specific problem, as each class of solvers has its own advantages and disadvantages.

A challenging issue presents itself when a gas approaches its critical point. Under such circumstances, a stiffness problem may manifest due to the heightened sensitivity of pressure to density variations. This scenario necessitates consideration of the finite dimensions of gas molecules and the accompanying intermolecular interactions prevalent in dense gases under elevated pressure levels. The occurrence of these intricacies may result in the decoupling of the momentum equation from the energy equation, thereby leading to potential convergence difficulties or even outright solver failure in that specific region.

Delving into the thermodynamic properties of the gas and pondering the underlying physics, one finds that the ratio of kinetic energy to internal energy for dense gas flow is significantly smaller compared to that of ideal gas flow. Consequently, the Mach number ceases to serve as a reliable measure of this ratio. Furthermore, the heat capacity ratio, which is widely used in the thermodynamic analyses of a ideal gas, becomes less important in dense gas flow. In an ideal gas scenario, the heat capacity ratio is the ratio of specific heat capacities of a gas at a constant pressure to that at a constant volume, which is a constant specific to the type of gas under consideration. However, as discussed in Chapter 2, the heat capacity in the case of a dense gas becomes a state variable, thereby leading to the ratio varying throughout the flow. Given the significant disparity between the kinetic and internal energy and the decoupling of the momentum and energy equations, the conventional density-based solver fails to perform effectively when the flow is near the gas's critical point.

To address this challenge, an innovative pressure-based solver for handling the compressible flow simulation is proposed and validated in this chapter. This newly proposed method promises to provide more accurate and reliable results in these challenging situations.

6.1 Background

The development of pressure-based solvers can be traced back to the pioneering works of Harlow and Welch (1965) [129], who introduced the Marker and Cell (MAC) method for solving the incompressible Navier-Stokes equations. Following this, Patankar and Spalding (1972) [130] developed the Semi-Implicit Method for Pressure-Linked Equations (SIMPLE) algorithm for incompressible flows, which has become one of the most widely used pressure-based solvers in CFD. This groundbreaking technique provided a foundation for the development of pressure-based methods in incompressible flow problems. Subsequently, Chorin (1967) [131] proposed the method of artificial compressibility for solving incompressible viscous flow problems, which was later improved by Kim and Moin (1985) [132] as the FSM (Fractional Step Method). These early contributions served as the building blocks for more advanced pressure-based methods that emerged in the following years.

Pressure-based solution methods can be classified into two categories: coupled and segregated approaches. Coupled methods, such as the PISO (Pressure-Implicit with Splitting of Operators) algorithm introduced by Issa (1986) [133], solve the governing equations simultaneously, leading to faster convergence but increased computational complexity. On the other hand, segregated methods, including the SIMPLE algorithm and its variants, solve the equations sequentially, which reduces computational demands but may require more iterations to converge. Both coupled and segregated methods have their merits and drawbacks, with the choice between them depending on the specific application and computational resources available.

Recent research in pressure-based methods has focused on further improving the efficiency, stability, and accuracy of these algorithms. One area of advancement is the utilization of adaptive mesh refinement (AMR) techniques. Berger and Oliger (1984) [134] proposed AMR as a means to dynamically adapt the computational mesh, allowing for localized refinement in regions of interest and coarsening in less critical regions. This adaptive approach improves computational efficiency while maintaining accuracy, particularly for flows with regions of high gradients or sharp shock waves.

Another area of research involves the incorporation of high-order discretization schemes. Traditional pressure-based methods employ second-order accurate schemes, but recent efforts have focused on implementing higher-order schemes, such as the Weighted Essentially Non-Oscillatory (WENO) method proposed by Shu and Osher (1988) [135]. These schemes achieve greater accuracy by reducing numerical dissipation and effectively capturing complex flow features with fewer computational resources. Furthermore, the use of parallel computing and efficient data structures has gained prominence to accelerate the computational performance of pressure-based methods. By leveraging modern computing architectures and parallel algorithms, significant reductions in simulation time have been achieved, allowing for more complex and detailed simulations of the flow field.

Pressure-based solvers are often compared to density-based solvers in terms of accuracy, stability, and computational efficiency. In earlier applications, pressure-based solvers are often more suitable for incompressible and weakly compressible flow regimes, while density-based solvers are well-suited for high-speed compressible flows. Here, the main strengths and weaknesses of the classic pressure-based solvers are outlined:

Strengths

- Applicability to incompressible and weakly compressible flows: Pressure-based solvers are well-suited for low-speed flows with low Mach numbers (less than 0.3), where density variations are small.
- Convergence rate: Pressure-based solvers generally have better convergence properties for incompressible and low-speed compressible flows. The algorithm can be decoupled into smaller sub-problems, which results in faster convergence, especially when using iterative methods like SIMPLE, SIMPLER, or PISO.
- Robustness and stability: Pressure-based solvers are generally more robust and stable in handling incompressible flows. They can accommodate a wide range of flow regimes with relatively small changes in solver settings, making them suitable for industrial applications where various conditions need to be simulated.
- Algorithm complexity and implementation: Pressure-based solvers are typically easier

to implement and have lower computational complexity compared to density-based solvers.

- Mesh flexibility: Pressure-based solvers can work well with both structured and unstructured meshes, allowing for a high degree of mesh flexibility. This is important in complex geometries or when using adaptive mesh refinement techniques.

Weaknesses

- Limited applicability to compressible flows: Pressure-based solvers are less suitable for compressible flows with high Mach numbers, where significant density variations and shock waves are present.
- Sensitivity to pressure-velocity coupling: Pressure-based solvers can be sensitive to the choice of pressure-velocity coupling algorithm, which may affect the convergence rate and stability of the solution. Researchers need to select the appropriate coupling method based on the problem characteristics.
- Difficulties in handling strong density gradients: Pressure-based solvers can struggle to accurately capture strong density gradients or discontinuities, such as those found in supersonic or hypersonic flows, multiphase flows, or reacting flows.
- Inadequate resolution of shock waves: Pressure-based solvers may not accurately resolve shock waves or other discontinuities in compressible flows, which can lead to inaccurate solutions.

To bridge the gap between incompressible and compressible flow solvers, providing a unified approach to solving a wide range of flow problems with a single solver, a novel pressure-based solution method for compressible flow is developed in the next section.

6.2 The Proposed Pressure-based Algorithm

The mass, momentum, and energy conservation equations for a compressible flow are given by:

$$\frac{\partial \rho}{\partial t} + \nabla \cdot (\mathbf{V}\rho) = 0 \tag{6.1}$$

$$\frac{\partial (\rho \mathbf{V})}{\partial t} + \nabla \cdot (\mathbf{V}\rho\mathbf{V}) = -\nabla p + \nabla \cdot \boldsymbol{\tau} \tag{6.2}$$

$$\frac{\partial \rho E}{\partial t} + \nabla \cdot (\mathbf{V}\rho H) = -\nabla \cdot \mathbf{q} + \nabla \cdot \boldsymbol{\tau} \cdot \mathbf{V} \tag{6.3}$$

where ρ, $\mathbf{V}$, p, $\boldsymbol{\tau}$, E, H, $\mathbf{q}$, and t denote the density, velocity, pressure, deviatoric stress tensor, total energy, total enthalpy, heat, and time.

To develop an algorithm for solving these equations, a mixed explicit-implicit scheme with first-order accuracy is adopted. The resulting discretized form of the governing equations is as follows:

$$\rho^{n+1} = \rho^{n} - \Delta t \nabla \cdot (\rho \mathbf{V})^{n+1} \tag{6.4}$$

$$\rho^{n+1}\mathbf{V}^{n+1} = \rho^{n}\mathbf{V}^{n} - \Delta t \left[\nabla \cdot (\rho \mathbf{V}\mathbf{V})^{n} + \nabla p^{n+1} - \nabla \cdot \boldsymbol{\tau}^{n}\right] \tag{6.5}$$

$$\rho^{n+1}E^{n+1} = \rho^{n}E^{n} - \Delta t \left[\nabla \cdot (\rho H \mathbf{V})^{n+1} + \nabla \mathbf{q}^{n} - \nabla \cdot \boldsymbol{\tau}^{n+1} \cdot \mathbf{V}^{n+1}\right] \tag{6.6}$$

In order to obtain a solution for Equations 6.4 and 6.5 using pressure as the primary variable, a temporary assumption is made by setting $E^{n+1} = E^{*}$, where E^{*} is initially assigned the value of E^{n}. Subsequently, an outer loop is iteratively employed to refine this assumption.

During the inner iteration process aimed at solving Equations 6.4 and 6.5, an assumption is adopted:

$$\rho = f_{\rho}(E^{*}, p) \tag{$\rho - EOS$}$$

Directly advancing Equation 6.5 with a guessed pressure p^* for ρ^{n+1}, which can be initially taken as p^n, will yield $(\rho v)^{n+1}$ that does not satisfy Equation 6.4. It is therefore essential to determine a correction term for p^* such that

$$p^{\overline{n+1}} = p^* + \Delta p \tag{6.7}$$

satisfies Equation 6.4.

The temporary solutions obtained through the advancement of Equation 6.5 with the preliminary guess p^* can be denoted as follows:

$$(\rho \mathbf{V})^* = (\rho \mathbf{V})^n - \Delta t R^*_{mom} \tag{6.8}$$

where

$$R^*_{mom} = (\nabla \cdot (\rho \mathbf{V}\mathbf{V})^n - \nabla \cdot \boldsymbol{\tau}^n) + \nabla p^* \tag{6.9}$$

which is the momentum residual evaluated at time step n based on the guessed pressure p^*.

Evidently, the resulting value of $(\rho \mathbf{V})^*$ obtained through this process fails to satisfy Equation 6.4. However, by substituting Equation 6.7 into Equation 6.5, we can express it in the following form:

$$(\rho \mathbf{V})^{\overline{n+1}} = (\rho \mathbf{V})^* - \Delta t \nabla(\Delta p) \tag{6.10}$$

Taking the divergence of Equation 6.10 yields:

$$\nabla \cdot (\rho \mathbf{V})^{\overline{n+1}} = \nabla \cdot (\rho \mathbf{V})^* - \Delta t \nabla^2(\Delta p) \tag{6.11}$$

Upon substitution of Equation 6.11 into Equation 6.4, the resulting expression can be written as:

$$\frac{\rho^{\overline{n+1}} - \rho^n}{\Delta t} + \nabla \cdot (\rho \mathbf{V})^* - \Delta t \nabla^2 (\Delta p) = 0 \tag{6.12}$$

$$\Delta t \nabla^2 (\Delta p) = \frac{\rho^{\overline{n+1}} - \rho^n}{\Delta t} + \nabla \cdot (\rho \mathbf{V})^* \tag{6.13}$$

Utilizing the $(\Delta t \Delta p)$ computed through the resolution of Equation 6.13 for updating $(\rho \mathbf{V})^{n+1}$ via Equation 6.10 ensures that the resulting value of $(\rho \mathbf{V})^{n+1}$ satisfies the implicit continuity Equation 6.4.

It is important to note that in solving Equation 6.13 for Δp or $(\Delta t \Delta p)$, an update to ρ^{n+1} is required by utilization of the $(\rho - EOS)$:

$$\rho^{\overline{n+1}} = f_\rho(E^*, p^{\overline{n+1}}) = f_\rho(E^*, p^* + \Delta p) \tag{6.14}$$

Once the values of $p^{\overline{n+1}}$, $v^{\overline{n+1}}$, and $\rho^{\overline{n+1}}$ have been obtained (passively through Equation 6.14), a new value for $(\rho E)^{\overline{n+1}}$ or $E^{\overline{n+1}}$ can be determined by applying Equation 6.6.

$$(\rho E)^{\overline{n+1},new} = \rho^n E^n - \Delta t \left[\nabla \cdot (\rho H \mathbf{V})^{\overline{n+1}} + \nabla \cdot \mathbf{q}^n - \nabla \cdot \boldsymbol{\tau}^{\overline{n+1}} \cdot \mathbf{V}^{\overline{n+1}} \right] \tag{6.15}$$

The pressure correction process described above is repeated until a consistent and converged solution set is obtained for the time step $n+1$, which includes the values p^{n+1}, v^{n+1}, and E^{n+1}. Throughout this iterative process, the solution is achieved by balancing the pressure and flow velocity, with the density being treated as a passive variable that is indirectly obtained from pressure and total energy (or temperature for ideal-gas cases) through the equation of state. This approach effectively avoids the issue of stiffness arising from large $\frac{\partial p}{\partial \rho}$ values, which are relatively significant compared to v^2 in the momentum equation. However, it may be necessary to revert to the density-based method for hypersonic flows, where the issue of stiffness is less significant for any $M < 100$.

In the scenario of an isentropic flow, a simplified expression can be utilized as the initial guess in each time step during the computation:

$$\rho = Const\ p^{1/\gamma}$$

It needs to be noted that the given isentropic relation should not be employed in the computation of the updated density for the present time step, and the constant C may exhibit variability within each discrete time step. The concept being proposed involves the utilization of pressure and density from the last time step to generate a new value for density to initialize the iteration. Upon the end of each time step, the energy equation will be brought into the application to facilitate an update in the density.

The Poisson equation (actually an inhomogeneous Helmholtz equation if the dependence of ρ on p is replaced by p directly) can be solved by line relaxation, perhaps with multigrid. As an example, rewrite Equation 6.13 for ideal gas:

$$\nabla^2(\Delta p) + \frac{\Delta p}{\Delta t^2(1-\gamma)(E^* - \frac{1}{2}\mathbf{V}\cdot\mathbf{V})} = f(E^*, p^*, (\rho\mathbf{V})^*, \rho^n)$$

The aforementioned procedure can be delineated in a sequential manner, as outlined below:

- **Step 1:** Allocate the current solution at time step n:

$$\mathbf{V}^n, \quad p^n, \quad E^n, \quad and \quad \rho^n = f_\rho(E^n, p^n)$$

- **Step 2:** Assign $p^* = p^n$ and $E^{\overline{n+1}} = E^n$.
- **Step 3:** Determine $(\rho\mathbf{V})^*$ utilizing Equations 6.8 and 6.9.

- **Step 4:** Employ the Poisson Equation 6.13 in conjunction with Equation 6.14 to ascertain $\Delta\rho$ (an inner iteration may be required). Subsequently, update p and ρ.

- **Step 5:** Update $\mathbf{V}$ using Equation 6.10:

  $$(\rho\mathbf{V})^{\overline{n+1}} = (\rho\mathbf{V})^{*} - \Delta t \nabla(\Delta p)$$

  At this juncture, the mass and momentum equations have been resolved under the fixed E^{*}.

- **Step 6:** Modify E to obtain $E^{\overline{n+1},new}$ employing Equation 6.15, with the most recent $\mathbf{V}^{\overline{n+1}}$, $p^{\overline{n+1}}$, and $\rho^{\overline{n+1}}$ (while maintaining the previous temperature for $\mathbf{q}$) on the right-hand side of Equation 6.15.

- **Step 7:** Assess convergence by determining $|\Delta p| <$ tolerance and $|\Delta E| = |E^{\overline{n+1},new} - E^{\overline{n+1}}| <$ tolerance.

  If the convergence criteria are met, set $E^{\overline{n+1}} = E^{\overline{n+1},new}$, and the solution is deemed complete.

  If the convergence criteria are not satisfied, assign $E^{\overline{n+1}} = E^{\overline{n+1},new}$, $p^{*} = p^{\overline{n+1}}$ and revert to Step 3.

A visual representation of the outlined algorithm can further facilitate understanding of the procedure. Figure 6.1 depicts the sequence of steps involved in the process and provides a comprehensive overview of the algorithm's progression.

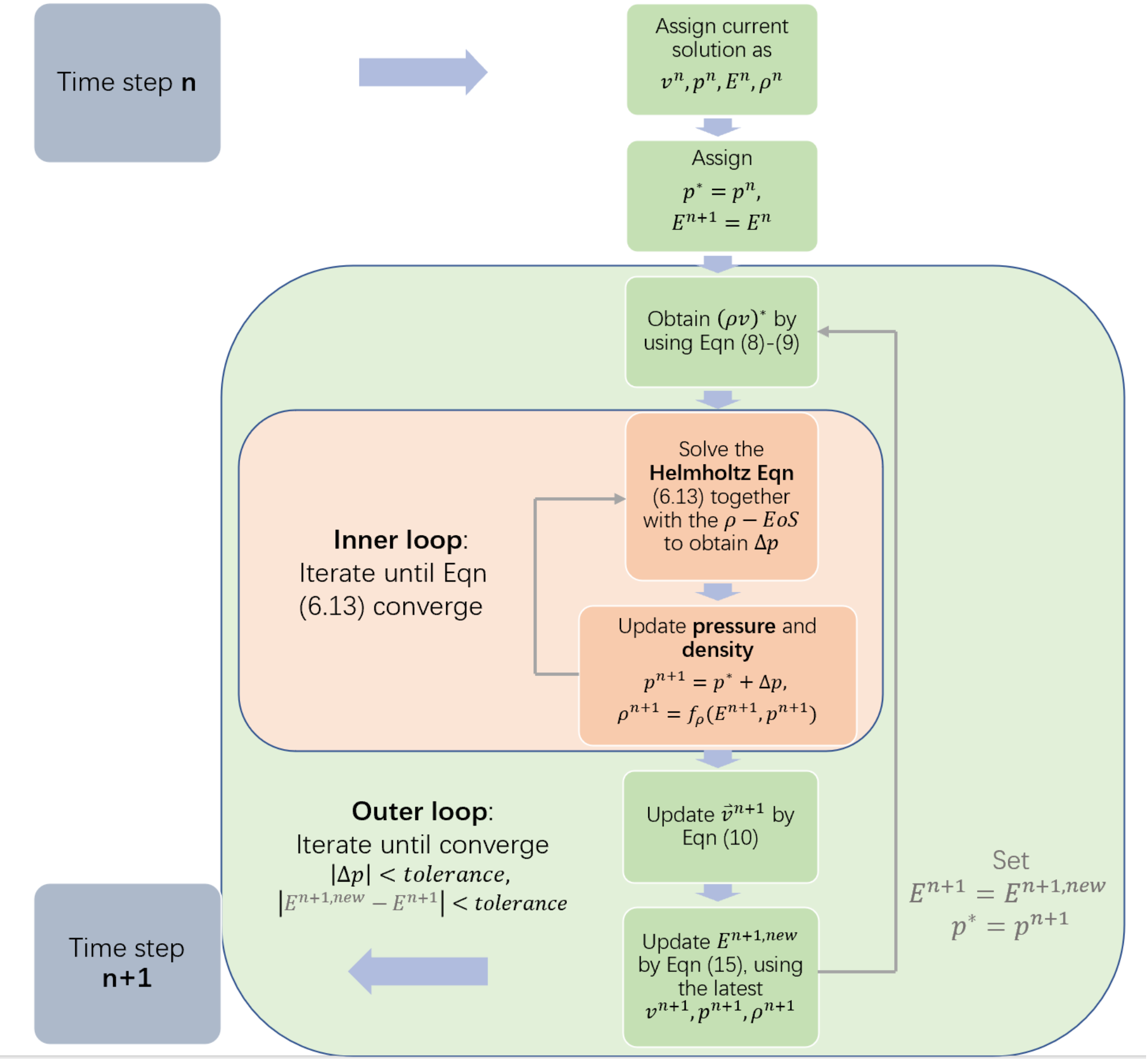

Figure 6.1: Flow chart of the core solver

To keep the scheme second-order accurate, a second-order central difference scheme in space and a fourth-order Runge-Kutta method in time are utilized to solve the discrete equation through practical application. The detailed discretized formulation of a quasi-one-dimensional channel example is shown in the next section.

6.3 Preliminary Numerical Results

In order to evaluate the stability and robustness of the algorithm under investigation, an examination is conducted by constructing a quasi-one-dimensional channel with a given gradually varying cross-sectional area, denoted as $S(x)$. This configuration serves as a benchmark problem, facilitating the evaluation of the performance of the pressure-based method in question. To maintain simplicity and focus on the essential attributes of the algorithm, the analysis employs the Euler equations as the governing equations for the channel flow.

By utilizing this simplified model, the study aims to provide valuable insights into the performance of the algorithm, focusing on its ability to maintain stability and demonstrate robustness under diverse conditions. The results obtained from the analysis will not only serve as a basis for validating the efficacy of the proposed method but also contribute to the ongoing advancement and refinement of pressure-based algorithms for solving more complex problems.

Nevertheless, within the scope of the Euler equations, the increase in entropy across the shock is not explicitly addressed due to the derivation of the Euler equations from a premise of reversible flow. When simulating real-world conditions, we usually incorporate the entropy condition. This condition is utilized to discern the physically relevant solution among the various mathematical solutions to the Euler equations. It requires that the entropy, or the measure of disorder in the system, must increase across the shock. Several numerical methods inherently satisfy the entropy condition, including the Jameson-Schmidt-Turkel (JST) scheme which is deployed in the current study. The JST scheme employs artificial viscosity terms to stabilize the numerical solution and emulate the physical process of energy dissipation. Thus, while the entropy condition is not explicitly imposed in the JST scheme, the artificial dissipation introduced by the method ensures that the entropy heightens across the shock, which is consistent with the physical reality and guarantees the numerical stability of the method.

For the flow in a 1D channel with a given cross-sectional area $S(x)$, the Euler equations can be written as

$$\frac{\partial(\rho S)}{\partial t}+\frac{\partial(\rho u S)}{\partial x}=0 \tag{6.16}$$

$$\frac{\partial(\rho u S)}{\partial t}+\frac{\partial(\rho u u S)}{\partial x}=-S\frac{\partial p}{\partial x} \tag{6.17}$$

$$\frac{\partial(\rho E S)}{\partial t}+\frac{\partial(\rho u H S)}{\partial x}=0 \tag{6.18}$$

Subsequently, the discretized formulation of the governing equations, as presented in Equations 6.4 through 6.6, can be simplified as:

$$(\rho S)^{n+1}=(\rho S)^{n}-\Delta t\nabla\cdot(\rho u S)^{n+1} \tag{6.19}$$

$$(\rho u S)^{n+1}=(\rho u S)^{n}-\Delta t\left[\nabla\cdot(\rho u u S)^{n}+S\nabla p^{n+1}\right] \tag{6.20}$$

$$(\rho E S)^{n+1}=(\rho E S)^{n}-\Delta t\nabla\cdot(\rho u H S)^{n+1} \tag{6.21}$$

Adhering to a similar methodology, the analogous expressions corresponding to Equation 6.10 is

$$(\rho u S)^{\overline{n+1}}=(\rho u S)^{*}-\Delta t S\nabla(\Delta p) \tag{6.22}$$

A significant challenge arises in the process of computing the divergence for the term $(\rho u S)^{\overline{n+1}}$. To illustrate this complexity, consider an arbitrary node point, denoted as i. The divergence of $(\rho u S)_i^{\overline{n+1}}$ is

$$\nabla\cdot(\rho u S)_i^{\overline{n+1}}=F_{i+\frac{1}{2}}-F_{i-\frac{1}{2}}$$

$$\nabla\cdot(\rho u S)_i^{\overline{n+1}}=\frac{(\rho u S)_{i+1}^{\overline{n+1}}+(\rho u S)_i^{\overline{n+1}}}{2\Delta x}-\frac{(\rho u S)_i^{\overline{n+1}}+(\rho u S)_{i-1}^{\overline{n+1}}}{2\Delta x}$$

where

$$(\rho u S)_i^{\overline{n+1}} = (\rho u S)_i^* - \Delta t S_i \frac{dp_{i+1} - dp_{i-1}}{2\Delta x}$$

Upon substituting the flux terms and reorganizing the equation, a refined expression for the divergence term, $\nabla \cdot (\rho u S)_i^{\overline{n+1}}$, at the node point i can be derived as

$$\nabla \cdot (\rho u S)_i^{\overline{n+1}} = \frac{(\rho u S)_{i+1}^* + (\rho u S)_{i-1}^*}{2\Delta x} - \frac{\Delta t}{4\Delta x^2}\left[S_{i+1}(dp_{i+2} - dp_i) - S_{i-1}(dp_i - dp_{i-2})\right] \quad (6.23)$$

This reformulation not only enables a more lucid representation of the mathematical relationship but also introduces additional complexities in solving the underlying equation system. Specifically, the construction of a pentadiagonal matrix for the pressure increment dp is needed, thereby increasing the intricacy of the problem. Moreover, extra attention must be devoted when establishing the boundary conditions and selecting appropriate parameters.

Prior to delving into the exploration of test cases, it is imperative to reaffirm the order of accuracy of the proposed solver, ensuring that each constituent element demonstrates, at a minimum, second-order accuracy. Given the employment of the second-order central difference scheme in the spatial dimension, our primary focus of scrutiny is the wider stencil term associated with pressure, a component that deviates from the traditional compact difference scheme assigned for pressure. This is particularly evident in the second term on the right-hand side of Equation 6.23. In the interest of maintaining simplicity, let us consider an instance with a constant cross-sectional area. We shall determine by Taylor expansions the truncation error of the following term:

$$\frac{dp_{i+2} - 2dp_i + dp_{i-2}}{4\Delta x^2}$$

The Taylor series expansions of dp_{i+2} and dp_{i-2} about the point dp_i are given by:

$$dp_{i+2} = dp_i + 2\Delta x \left(\frac{d(dp)}{dx}\right)_i + 2\Delta x^2 \left(\frac{d^2(dp)}{dx^2}\right)_i + \frac{8\Delta x^3}{6}\left(\frac{d^3(dp)}{dx^3}\right)_i + O(\Delta x^4),$$
$$dp_{i-2} = dp_i - 2\Delta x \left(\frac{d(dp)}{dx}\right)_i + 2\Delta x^2 \left(\frac{d^2(dp)}{dx^2}\right)_i - \frac{8\Delta x^3}{6}\left(\frac{d^3(dp)}{dx^3}\right)_i + O(\Delta x^4).$$

Now, substituting these expansions into the term $\frac{dp_{i+2} - 2dp_i + dp_{i-2}}{4\Delta x^2}$, we get:

$$\frac{dp_{i+2} - 2dp_i + dp_{i-2}}{4\Delta x^2} = \left(\frac{d^2(dp)}{dx^2}\right)_i + \frac{\Delta x^2}{3}\left(\frac{d^4(dp)}{dx^4}\right)_i + O(\Delta x^4).$$

The first term on the right side is the second derivative of dp, which is the exact term we expect from a second-order central difference scheme. The next term is the truncation error, which is proportional to Δx^2, confirming that this is indeed a second-order scheme. The higher order terms, which are represented by $O(\Delta x^4)$, become negligible as Δx tends to zero.

Three validation cases were conducted to evaluate the performance of the proposed pressure-based solution method, with results compared against the corresponding analytical solutions. The cross-sectional area of the nozzle utilized in these cases is illustrated in Figure 6.2. Furthermore, the distribution of pressure, Mach number, and density along the flow direction are depicted in a series of plots, as shown in Figures 6.3 through 6.5.

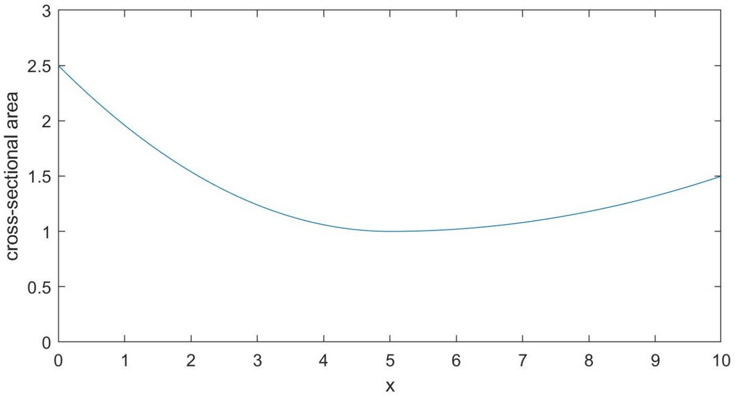

Figure 6.2: Cross-sectional area S(x)

The first validation case represents a common scenario, wherein the fluid flow experiences acceleration within the converging section of the nozzle and deceleration within the diverging portion, culminating in a subsonic outlet. A comparison of the distribution of flow variables within the nozzle demonstrates remarkable agreement with the analytical solution, highlighting the accuracy and reliability of the proposed numerical method.

The second validation case encompasses a scenario in which a normal shock wave is present within the nozzle. The proposed algorithm demonstrates its robustness by successfully capturing the shock and accurately computing the pre-shock and post-shock conditions. However, one area for potential improvement lies in the presence of cusps at the shock location, indicating a need for further optimization in future studies. In the current analysis, artificial viscosity is incorporated within the spatial discretization process, which may necessitate tuning the second-order parameters to enhance the performance around the shock. For the time being, to circumvent unwieldy computational complexity and excessive resource requirements, the algorithm does not incorporate viscous stresses and thermal conductivity. Despite the temporary omission of these factors, the intent is not to underestimate their significance. Indeed, these components can offer a more accurate representation of the flow, albeit at the cost of computational efficiency and resources. Future expansion will necessitate the resolution of the Navier-Stokes equations to provide a more detailed and accurate representation of the flow conditions.

The final validation case investigates a low Mach number flow scenario, wherein the Mach number reaches values as low as 10^{-3}. In such instances, conventional density-based solvers often face convergence challenges, primarily due to the amplification of numerical errors resulting from the disparity between the convective and pressure terms. This discrepancy arises as the Mach number approaches zero, rendering the governing equations ill-conditioned and subsequently causing the solver to fail. To circumvent this issue, preconditioning methods are typically employed to recalibrate the balance between the convective and pressure terms, thereby ensuring the proper functionality of density-based solvers. However, the algorithm proposed in this study exhibits a distinct advantage, as it eliminates the need for preconditioning and demonstrates robust performance within this low Mach number range. By exhibiting superior performance without the need for additional preconditioning techniques, the proposed method offers a valuable alternative to conventional density-based solvers and contributes significantly to the ongoing development of efficient and reliable numerical techniques in the field of fluid dynamics.

The examination of these cases serves as a critical assessment of the algorithm's performance, particularly in scenarios that pose unique challenges for traditional numerical methods. However, these results are only for regular ideal gas to demonstrate the ability of the proposed method to work efficiently for both transonic flows with shocks and low speed flows with Mach number as low as 10^{-3} without loss of efficiency and accuracy. Future work will be focusing on validating the new method for the dense gas model. Through the demonstration of the algorithm's ability to effectively handle such cases, the study highlights its potential for broader applicability and its capacity to address a wide range of CFD problems in both academic and industrial settings.

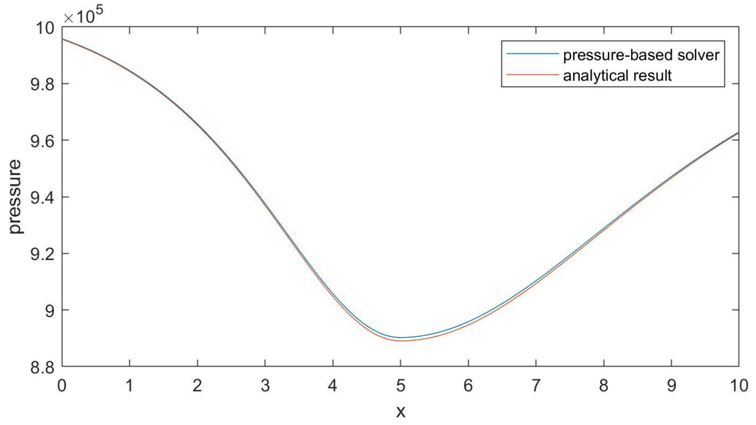

(a) Pressure

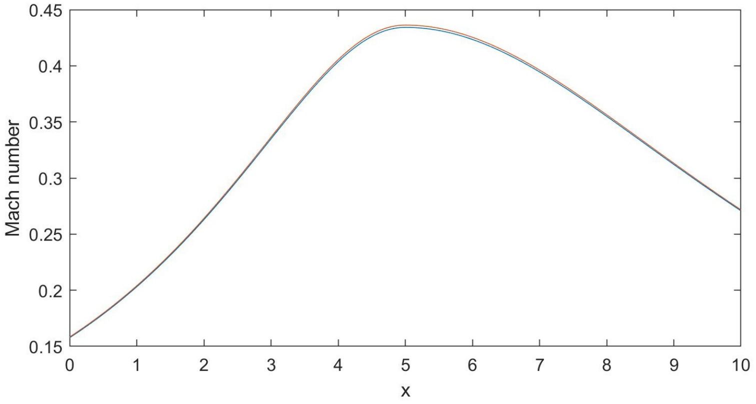

(b) Mach number

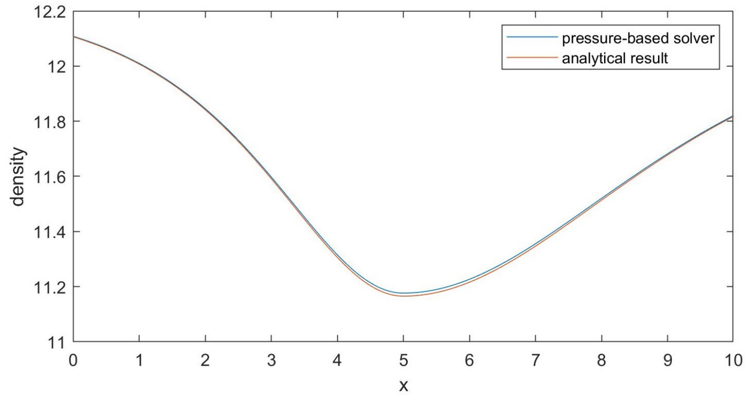

(c) Density

Figure 6.3: Validation of pressure-based solver: Case 1

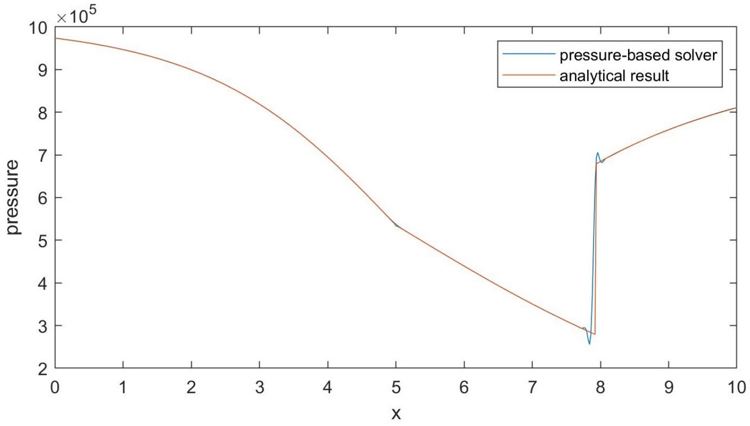

(a) Pressure

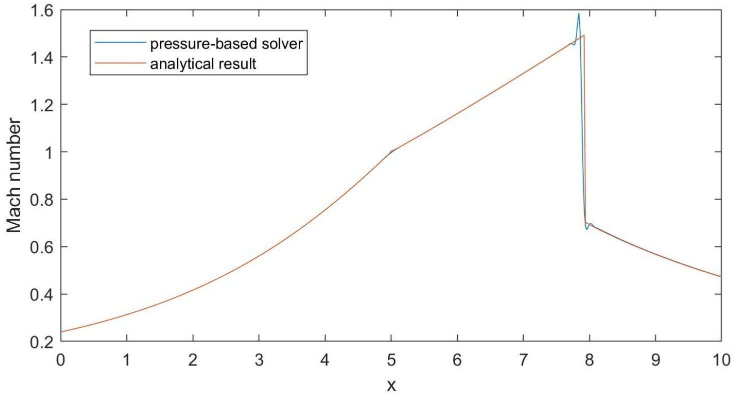

(b) Mach number

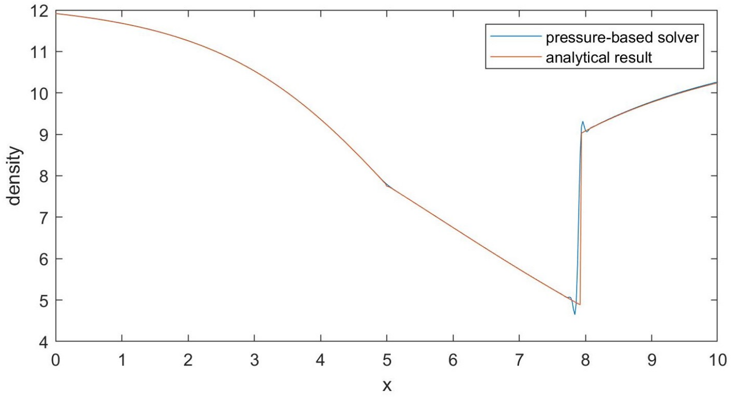

(c) Density

Figure 6.4: Validation of pressure-based solver: Case 2

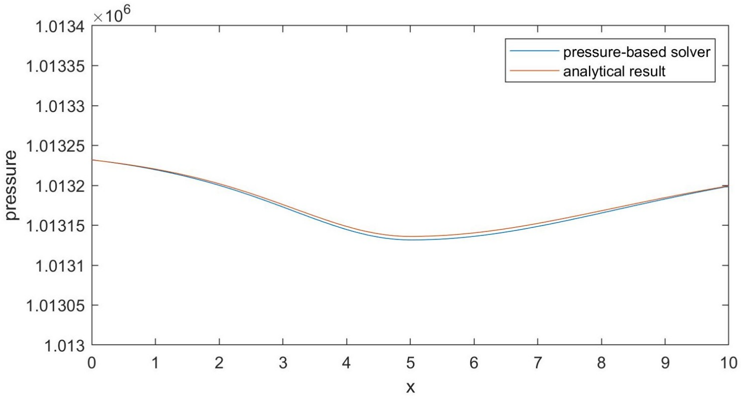

(a) Pressure

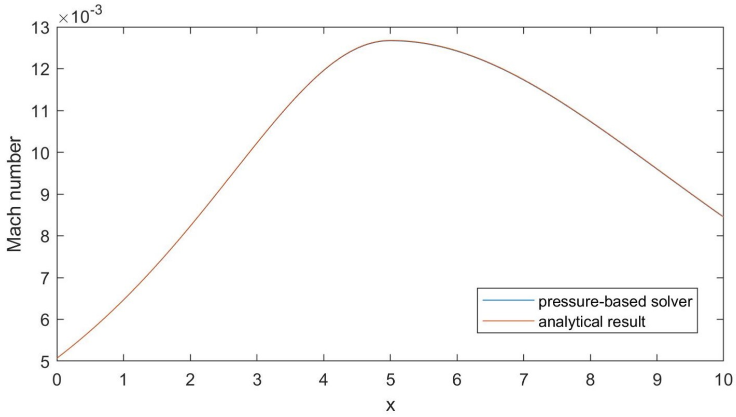

(b) Mach number

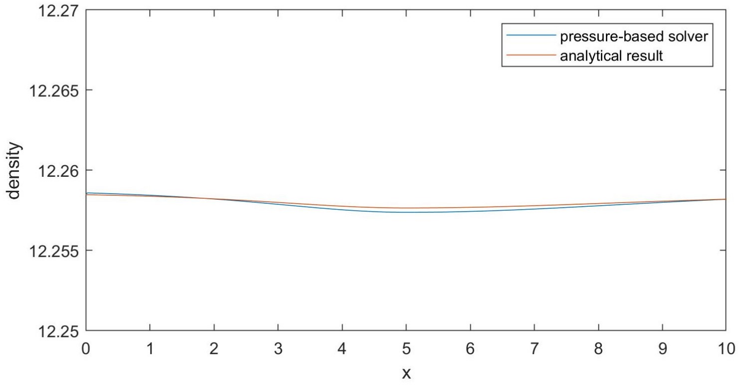

(c) Density

Figure 6.5: Validation of pressure-based solver: Case 3

Chapter 7

Conclusions and Future Work

This research has delved into the realm of nonclassical gas dynamics, with a primary focus on understanding the behavior of dense gases in various flow regimes. The study aimed to achieve the following objectives:

1. Thoroughly investigate the nonclassical gas dynamic behavior of BZT gases;
2. Identify a more accurate method for calculating thermodynamic properties of dense gases near their critical points;
3. Analyze and understand unconventional wave phenomena associated with nonclassical gas dynamics in BZT gases;
4. Develop an efficient and robust numerical method and computer code for computing dense gas flows.

The research commenced with an examination of the fundamental derivative and its physical implications, fostering a comprehensive understanding of dense gas phenomena. The relationships between the fundamental derivative and other flow variables were explored, leading to the detailed flow equations for quasi-one-dimensional channel flow. The investigation revealed that dense gas flows exhibit distinct behaviors compared to conventional gas dynamics, with the research findings highlighting unconventional flow behaviors in various regions. The MDM gas using the Van der Waals real-gas equation of state has been selected as the working fluid in this work to systematically and in-depth investigate the nonclassical gas behaviors.

The value of the fundamental derivative Γ is determined by the thermodynamic state variables and significantly influences the gas behavior and flow properties. For dense gas, there are certain regions that the flow behavior that is different from ordinary gas dynamics, and those regions are divided by two significant demarcation lines of Γ marked out in the p-v plane, $\Gamma = 0$ and $\Gamma = 1$.

- When $\Gamma > 1$, the gas behaves the same way as the conventional theory predicts.
- When $\Gamma < 1$, the speed of sound decreases with increasing pressure, and the Mach number is no longer a monotonic function of flow velocity. Meanwhile, the relationship between the velocity and cross-sectional area change is different. More specifically, it can be divided into two conditions. For $M^2 < \frac{1}{1-\Gamma}$, the gas behaves the same way as a conventional gas. The Mach number increases with increasing velocity, as well a converging channel accelerates a subsonic flow and decelerates a supersonic flow. For $M^2 > \frac{1}{1-\Gamma}$, the flow behaves in the complete opposite way to the classical theory. The Mach number decreases with increasing velocity, as well a diverging channel accelerates a subsonic flow and decelerates a supersonic flow.
- When $\Gamma < 0$, the nozzle geometry at the transonic location is changed. To access a transonic flow, the divergent-convergent nozzle is needed instead of the traditional convergent-divergent nozzle.

The outcomes emphasized the presence of unconventional flow patterns across different regions in a practical flow scenario, revealing instances of multiple non-conventional gas dynamics within a single flow. In certain cases, the presence of multiple sonic points within a nozzle necessitates the use of multiple throats to effectively accelerate the flow.

The study also investigated the generation of expansion shock waves and the Prandtl-Meyer relation for nonclassical gases. The research discovered the existence of a critical Mach number beyond which expansion shocks cannot occur and revealed a correlation between the critical Mach number and the size of the nonclassical area. Determining this critical value is not possible through explicit analytical expressions and requires the application of numerical methods.

The normal shock wave relations for dense gas are also different in the unconventional regime. The main results are listed below.

- Expansion shocks do exist and can be captured in a narrow area near the critical point. Static pressure, temperature, and density decrease across the expansion shock wave, except entropy.
- The total pressure drop is much smaller across an expansion shock, which means less energy is lost for nonclassical gas cases.
- For a dense gas, if the pre-shock thermodynamic state is near the critical point and the pre-shock Mach number is close to 1, there will be multiple post-shock solutions for one pre-shock condition.
- The classical theory only allows compression shock waves that the pre-shock flow is supersonic and the post-shock flow is subsonic. However, both the pre-shock flow and the post-shock flow can be supersonic for a dense gas case.

The unconventional gas model was implemented into the in-house code “cns2d”. A matrix dissipation method incorporating real-gas effects was proposed to accurately capture discontinuous compression and expansion shocks that might appear in the same flow field. Several test cases were conducted to evaluate the algorithm's performance and potential for broader applicability. The existence of expansion shock waves and compression fans in the nonclassical $\Gamma < 0$ region is confirmed numerically. Results show the wave structure's dependency on the upstream conditions. Computations are performed on flow in a shock tube, over an expansion corner, and over a compression corner. The resulting wave fields are presented and evaluated.

Additionally, the development of accurate models of thermodynamic properties for dense gases remains a formidable task with crucial implications for numerous fields. This research applied machine learning techniques to advance modeling thermodynamic properties for dense gases, utilizing the Artificial Neural Network (ANN) for its superior accuracy. A detailed comparison between the prediction results from different ANN models is presented, alongside the corresponding neural network structure and time for training. The results reveal that the Bayesian Regularization model exhibits the highest accuracy among the tested model. Numerical simulations were run to evaluate the performance of the trained ANN model. The ANN model demonstrated excellent agreement with the results computed via the traditional equation of state.

Another part of the study is to bridge the gap between incompressible and compressible flow solvers, providing a unified approach to solving a wide range of flow problems with a single solver. An innovative pressure-based solver was proposed and validated to address the stiffness issue arising from the increased sensitivity of pressure on density when a gas approaches its critical point. Special care should be given to solving the Helmholtz equation and setting up the appropriate boundary conditions. This solver demonstrated its effectiveness in handling challenging cases and showcased its potential for addressing a wide range of CFD problems in both academic and industrial settings.

We have developed the basic theory for the quasi-1D isentropic flow, normal shock waves, and flows past 2D compression, or expansion corner for dense gas in three different regimes of fundamental derivative, $\Gamma > 1$, $0 < \Gamma < 1$, and $\Gamma < 0$. We examined and mapped out conditions for which peculiar unconventional behavior of the flow can occur. We also developed numerical methods that meet special challenges in computing the flow of such dense gases. The fundamental knowledge and numerical technique provide a critical basis for future theoretical studies of complex flow involving BZT-type dense gases and application in the design of compressors or turbines in an Organic Rankine Cycles engine.

Immediate future work includes extending the new numerical method and the ANN gas model to study other types of dense gas and practical compressors. Another area of research is to use the method developed here to design experiments to verify the theoretical finding of the peculiar nonclassical flow phenomena.

Bibliography

[1] Tiemo Mathijssen. Experimental observation of non-ideal compressible fluid dynamics: with application in organic rankine cycle power systems. 2017.

[2] Philip A Thompson. *Compressible-fluid dynamics*. McGraw-Hill, 1971.

[3] John David Anderson. *Modern compressible flow: with historical perspective*, volume 12. McGraw-Hill New York, 1990.

[4] Shell. World energy model: a view to 2100. Technical report, 2017.

[5] Frederica Perera. Pollution from fossil-fuel combustion is the leading environmental threat to global pediatric health and equity: Solutions exist. *International journal of environmental research and public health*, 15(1):16, 2018.

[6] Core Writing Team et al. Intergovernmental panel on climate change (2014) climate change 2014: Synthesis report. contribution of working groups 646 i. *II and III to the Fifth Assessment Report of the Intergovernmental Panel on Climate Change*, page 151, 2014.

[7] A. Mahmoudi, M. Fazli, and M.R. Morad. A recent review of waste heat recovery by organic rankine cycle. *Applied Thermal Engineering*, 143:660–675, 2018.

[8] Steven Lecompte, Henk Huisseune, Martijn Van Den Broek, Bruno Vanslambrouck, and Michel De Paepe. Review of organic rankine cycle (orc) architectures for waste heat recovery. *Renewable and sustainable energy reviews*, 47:448–461, 2015.

[9] Michael J Moran, Howard N Shapiro, Daisie D Boettner, and Margaret B Bailey. *Fundamentals of engineering thermodynamics*. John Wiley & Sons, 2010.

[10] Giorgio Soave. Equilibrium constants from a modified redlich-kwong equation of state. *Chemical engineering science*, 27(6):1197–1203, 1972.

[11] Roland Span and Wolfgang Wagner. A new equation of state for carbon dioxide covering the fluid region from the triple-point temperature to 1100 k at pressures up to 800 mpa. *Journal of physical and chemical reference data*, 25(6):1509–1596, 1996.

[12] Ding-Yu Peng and Donald B Robinson. A new two-constant equation of state. *Industrial & Engineering Chemistry Fundamentals*, 15(1):59–64, 1976.

[13] Reginald Ivan Lewis. *Turbomachinery performance analysis*. Butterworth-Heinemann, 1996.

[14] Philip A Thompson. A fundamental derivative in gasdynamics. *The Physics of Fluids*, 14(9):1843–1849, 1971.

[15] P Colonna and ALBERTO Guardone. Molecular interpretation of nonclassical gas dynamics of dense vapors under the van der waals model. *Physics of Fluids*, 18(5):056101, 2006.

[16] Yuanbin Liu, Weixiang Hong, and Bingyang Cao. Machine learning for predicting thermodynamic properties of pure fluids and their mixtures. *Energy*, 188:116091, 2019.

[17] Yoonhan Ahn, Seong Jun Bae, Minseok Kim, Seong Kuk Cho, Seungjoon Baik, Jeong Ik Lee, and Jae Eun Cha. Review of supercritical co2 power cycle technology and current status of research and development. *Nuclear Engineering and Technology*, 47(6):647–661, 2015.

[18] Vaclav Dostal, Pavel Hejzlar, and Michael J Driscoll. The supercritical carbon dioxide power cycle: comparison to other advanced power cycles. *Nuclear technology*, 154(3):283–301, 2006.

[19] Junhyun Cho, Munkyoung Choi, Young-Jin Baik, Gilbong Lee, Ho-Sang Ra, Byunghui Kim, and Minsung Kim. Development of the turbomachinery for the supercritical carbon dioxide power cycle. *International Journal of Energy Research*, 40(5):587–599, 2016.

[20] Enrico Rinaldi, Rene Pecnik, and Piero Colonna. Computational fluid dynamic simulation of a supercritical co2 compressor performance map. *Journal of Engineering for Gas Turbines and Power*, 137(7):072602, 2015.

[21] Nikola D Baltadjiev, Claudio Lettieri, and Zoltán S Spakovszky. An investigation of real gas effects in supercritical co2 centrifugal compressors. *Journal of Turbomachinery*, 137(9):091003, 2015.

[22] Hans Albrecht Bethe. The theory of shock waves for an arbitrary equation of state, office of scientific research and development, washington. *Report*, 575:57, 1942.

[23] P Duhem. On the propagation of shock waves in fluids. *Z. Phys. Chem*, 69:169–186, 1909.

[24] Hermann Weyl. Shock waves in arbitrary fluids. *Communications on Pure and Applied Mathematics*, 2(2-3):103–122, 1949.

[25] Richard Courant and Kurt Otto Friedrichs. *Supersonic flow and shock waves*, volume 21. Springer Science & Business Media, 1999.

[26] Ya B Zel'dovich. Theory of shock waves and introduction to gas dynamics [in russian], izd. *AN SSSR, Moscow*, 946, 1946.

[27] Lev Davidovich Landau and Evgenii Mikhailovich Lifshits. *Fluid mechanics, by LD Landau and EM Lifshitz*, volume 11. Pergamon Press Oxford, UK, 1959.

[28] KC Lambrakis and PA Thompson. Existence of real uids with a negative fundamental derivative γ. *Physics of Fluids*, 15(5):933.

[29] MS Cramer and GM Tarkenton. Transonic flows of bethe-zel'dovich—thompson fluids. *Journal of Fluid Mechanics*, 240:197–228, 1992.

[30] P Colonna, ALBERTO Guardone, and NR Nannan. Siloxanes: a new class of candidate bethe-zel'dovich-thompson fluids. *Physics of Fluids*, 19(8):086102, 2007.

[31] Hugh Longbourne Callendar. On the thermodynamical properties of gases and vapours as deduced from a modified form of the joule-thomson equation, with special reference to the properties of steam. *Proceedings of the Royal Society of London*, 67(435-441):266–286, 1901.

[32] DA Sullivan. Historical review of real-fluid isentropic flow models. *Journal of Fluids Engineering*, 103(2):258–267, 1981.

[33] V Arp, JM Persichetti, and Guo-bang Chen. The gruneisen parameter in fluids. *Journal of fluids engineering*, 106(2):193–200, 1984.

[34] E Grüneisen. Zustand des festen körpers. In *Thermische Eigenschaften der Stoffe*, pages 1–59. Springer, 1926.

[35] JC Leung and M Epstein. A generalized critical flow model for nonideal gases. *AIChE journal*, 34(9):1568–1572, 1988.

[36] Robert C Johnson. Calculations of real-gas effects in flow through critical-flow nozzles. *Journal of Basic Engineering*, 86(21):519–526, 1964.

[37] W Bober and WL Chow. Nonideal isentropic gas flow through converging-diverging nozzles. *Journal of fluids engineering*, 112(4):455–460, 1990.

[38] William A Sirignano. Normal shocks with high upstream pressure. *Physical Review Fluids*, 3(9):093401, 2018.

[39] William A Sirignano. Compressible flow at high pressure with linear equation of state. *Journal of Fluid Mechanics*, 843:244–292, 2018.

[40] Piero Colonna and Paolo Silva. Dense gas thermodynamic properties of single and multicomponent fluids for fluid dynamics simulations. *J. Fluids Eng.*, 125(3):414–427, 2003.

[41] G Angelino and C Invernizzi. Cyclic methylsiloxanes as working fluids for space power cycles, 1993.

[42] Alberto Guardone, Piero Colonna, Emiliano Casati, and Enrico Rinaldi. Non-classical gas dynamics of vapour mixtures. *Journal of fluid mechanics*, 741:681–701, 2014.

[43] Al A Borisov, SS Kutateladze, and VE Nakoryakov. Rarefaction shock wave near the critical liquid–vapour point. *Journal of Fluid Mechanics*, 126:59–73, 1983.

[44] SS Kutateladze, VE Nakoryakov, and AA Borisov. Rarefaction waves in liquid and gas-liquid media. *Annual review of fluid mechanics*, 19(1):577–600, 1987.

[45] MS Cramer. Negative nonlinearity in selected fluorocarbons. *Physics of Fluids A: Fluid Dynamics*, 1(11):1894–1897, 1989.

[46] Mark S Cramer, A Kluwick, Layne T Watson, and Wolfgang Pelz. Dissipative waves in fluids having both positive and negative nonlinearity. *Journal of Fluid Mechanics*, 169:323–336, 1986.

[47] Stephen Fergason, Alberto Guardone, and Brian Argrow. Construction and validation of a dense gas shock tube. *Journal of thermophysics and heat transfer*, 17(3):326–333, 2003.

[48] MS Cramer. Shock splitting in single-phase gases. *Journal of Fluid Mechanics*, 199:281–296, 1989.

[49] MS Cramer and AB Crickenberger. The dissipative structure of shock waves in dense gases. *Journal of fluid mechanics*, 223:325–355, 1991.

[50] Philip A Thompson, Garry C Carofano, and Yoon-Gon Kim. Shock waves and phase changes in a large-heat-capacity fluid emerging from a tube. *Journal of Fluid Mechanics*, 166:57–92, 1986.

[51] SC Gulen, PA Thompson, and HJ Cho. Rarefaction and liquefaction shock waves in regular and retrograde fluids with near-critical end states. In *Adiabatic waves in liquid-vapor systems*, pages 281–290. Springer, 1990.

[52] SH Fergason, TL Ho, BM Argrow, and G Emanuel. Theory for producing a single-phase rarefaction shock wave in a shock tube. *Journal of Fluid Mechanics*, 445:37–54, 2001.

[53] Stephen Fergason and Brian Argrow. Simulations of nonclassical dense gas dynamics. In *35th AIAA Thermophysics Conference*, page 2752, 2001.

[54] Stephen Fergason and Brian Argrow. Construction and operation of a dense gas shock tube. In *35th AIAA Thermophysics Conference*, page 2747, 2001.

[55] Rolf Radespiel, Malte Estorf, Dirk Heitmann, Federico Muñoz, and Torsten Wolf. Hypersonic ludwieg tube. *Experimental Methods of Shock Wave Research*, pages 433–458, 2016.

[56] P Colonna, A Guardone, NR Nannan, and C Zamfirescu. Design of the dense gas flexible asymmetric shock tube. *Journal of fluids engineering*, 130(3), 2008.

[57] Andrea Spinelli, Vincenzo Dossena, Paolo Gaetani, Carlo Osnaghi, and D Colombo. Design of a test rig for organic vapours. In *Turbo Expo: Power for Land, Sea, and Air*, volume 44007, pages 109–120, 2010.

[58] Andrea Spinelli, Giorgia Cammi, Marta Zocca, Simone Gallarini, Fabio Cozzi, Paolo Gaetani, Vincenzo Dossena, and Alberto Guardone. Experimental observation of non-ideal expanding flows of siloxane mdm vapor for orc applications. *Energy Procedia*, 129:1125–1132, 2017.

[59] Andrea Spinelli, Fabio Cozzi, Giorgia Cammi, Marta Zocca, Paolo Gaetani, Vincenzo Dossena, and Alberto Guardone. Preliminary characterization of an expanding flow of siloxane vapor mdm. In *Journal of Physics: Conference Series*, volume 821, page 012022. IOP Publishing, 2017.

[60] BM Argrow. Computational analysis of dense gas shock tube flow. *Shock Waves*, 6(4):241–248, 1996.

[61] AC Aldo and BM Argrow. Dense gas flow in minimum length nozzles, 1995.

[62] Andrew C Aldo and Brian M Argrow. Supersonic minimum length nozzle design for dense gases, 1993.

[63] BP Brown and BM Argrow. Two-dimensional shock tube flow for dense gases. *Journal of Fluid Mechanics*, 349:95–115, 1997.

[64] Brady P Brown and Brian M Argrow. Nonclassical dense gas flows for simple geometries. *AIAA journal*, 36(10):1842–1847, 1998.

[65] Brady P Brown and Brian M Argrow. Application of bethe-zel'dovich-thompson fluids in organic rankine cycle engines. *Journal of Propulsion and Power*, 16(6):1118–1124, 2000.

[66] ALBERTO Guardone, Vittorio Selmin, and Luigi Vigevano. An investigation of roe's linearization and average for ideal and real gases, 1999.

[67] ALBERTO Guardone and Luigi Vigevano. Roe linearization for the van der waals gas. *Journal of Computational Physics*, 175(1):50–78, 2002.

[68] Jeffrey Francis Monaco, Mark S Cramer, and Layne Terry Watson. Supersonic flows of dense gases in cascade configurations. *Journal of Fluid Mechanics*, 330:31–59, 1997.

[69] Paola Cinnella and Pietro M Congedo. Numerical solver for dense gas flows. *AIAA journal*, 43(11):2458–2461, 2005.

[70] Donald Stephen Lowell Cardwell. *From Watt to Clausius: The rise of thermodynamics in the early industrial age.* Cornell University Press Ithaca, NY, 1971.

[71] Luigi D'Amelio. *L'impiego di vapori ad alto peso molecolare in piccole turbine e l'utilizzazione del calore solare per energia motrice.* INAG, 1935.

[72] WS Findlay. Some suggestions for diphenyl heat engine cycles. *Power Engineering*, 29:89–91, 1934.

[73] DC Purdy. Diphenyl as a thermodynamic fluid. *Nucleonics (US) Ceased publication*, 15, 1957.

[74] H Tabor and L Bronicki. Establishing criteria for fluids for small vapor turbines. *SAE Transactions*, pages 561–575, 1965.

[75] John W Bjerklie. Working fluid as a design variable for a family of small rankine power systems. In *ASME 1967 Gas Turbine Conference and Products Show*. American Society of Mechanical Engineers Digital Collection, 1967.

[76] Hans D Linhardt and GP Carver. Development progress of organic rankine cycle power systems. Technical report, Philco-Ford Corp., Newport Beach, Calif., 1967.

[77] S Luchter. Current status of the technology of organic rankine cycle power plants. Technical report, Mechanical Tech. Inc., Latham, NY, 1967.

[78] AW Adam and RE Niggemann. Organic rankine cycle technology program: A status report., 1969.

[79] Gerald S Leighton. Organic rankine cycle. In *IEEE TRANSACTIONS ON AEROSPACE AND ELECTRONIC SYSTEMS*, number 5, page 811. IEEE-INST ELECTRICAL ELECTRONICS ENGINEERS INC 345 E 47TH ST, NEW YORK, NY, 1968.

[80] R GARCIA. Jet condenser development for an organic rankine-cycle power conversion system(jet condenser at very low pressure in organic rankine cycle power conversion system noting role in power efficiency), 1969.

[81] JH VanOsdol, RF Wilson, and RE Niggemann. Zirconium hydride reactor–organic rankine power systems. In *pp 456-64 of Proceedings of the Fourth Intersociety Energy Conversion Engineering Conference, September 22–26, 1969, Washington, DC New York American Inst. of Chemical Engineers (1969).* Atomics International, Canoga Park, Calif., 1969.

[82] Harry L Solberg and Keith H Hawks. Thermal performance of fluids in a rankine cycle power plant for automotive applications. In *pp 813-23 of 1971 Intersociety Energy Conversion Engineering Conference. New York Society of Automotive Engineers, Inc.(1971).* Purdue Univ., Lafayette, Ind., 1971.

[83] DR Miller, HR Null, and QE Thompson. Optimum working fluids for automotive rankine engines. volume ii. technical section, 1973.

[84] DB Wigmore, RE Niggemann, and JB O'Sullivan. Specification of an optimum working fluid for a small rankine cycle turboelectric power system. In *7th intersociety energy conversion engineering conference*, 1972.

[85] DK Werner and RE Barber. Working fluid selection for a small rankine cycle total energy system for recreation vehicles. In *8th Intersociety Energy Conversion Engineering Conference, Philadelphia, Aug*, pages 13–17, 1973.

[86] HM Curran, M Lokmanhekin, T Alereza, and M Miller. Assessment of rankine cycle for potential application to solar-powered cooling of buildings. In *American Society of Mechanical Engineers, Winter Annual Meeting*, 1974.

[87] JE Boretz. Technology considerations for organic rankine cycle electric power systems. In *9th Intersociety Energy Conversion Engineering Conference*, pages 61–67, 1974.

[88] FR Biancardi, MD Meader, WA Blecher, and JB Hall. Design and operation of a solar-powered turbocompressor air-conditioning and heating system. In *iece*, pages 186–194, 1975.

[89] GS Somekh. Water-pyridine azeotrope is an excellent rankine cycle fluid, 1975.

[90] LI Stiel, RA Allen, and KP Murphy. Optimum properties of working fluids for solar powered heat pumps. In *Energy 10; Annual Intersociety Energy Conversion and Engineering Conference*, pages 171–177, 1975.

[91] RE Barber. Solar powered organic rankine cycle engines-characteristics and costs. In *11th Intersociety Energy Conversion Engineering Conference*, pages 1151–1156, 1976.

[92] V Maizza et al. The use of unconventional fluids for single stage supersonic turbines of low power output., 1976.

[93] CO Langebrake. Refrigerant-114 rankine cycle energy recovery technology from the gaseous diffusion industry. Technical report, Goodyear Atomic Corp., Piketon, OH (USA), 1978.

[94] RE Niggemann, WJ Greenlee, and PD Lacey. Fluid selection and optimization of an organic rankine-cycle waste heat power conversion system. In *Mechanical Engineering*, volume 101, pages 93–93. ASME-AMER SOC MECHANICAL ENG 345 E 47TH ST, NEW YORK, NY 10017, 1979.

[95] JP Durand and D Mercier. Solar plants for water pumping and/or electricity supply in intertropical zones. In *Proc. ISES Silver Jubilee Cong.*, page 1506, 1979.

[96] C Maccio, G Tomei, G Angelino, M Gaia, and E Macchi. Operational experience of a 3.0 kw solar powered water pump. In *Sun II*, pages 1501–1505, 1979.

[97] WD Batton and RE Barber. Rankine engine solar power generation-2. the power generation module. *Am. Soc. Mech. Eng.,(Pap.);(United States)*, 81, 1981.

[98] RE Barber. Solar and geothermal rankine cycle engines can convert petroleum industry waste heat into electrical power. In *asme*, 1980.

[99] RM Cheek and PD Lacey. 600 kw organic rankine cycle waste heat power conversion system. In *12th Intersociety Energy Conversion Engineering Conference*, pages 1095–1099, 1977.

[100] Andrew PS Wheeler and Jonathan Ong. The role of dense gas dynamics on orc turbine performance. In *ASME Turbo Expo 2013: Turbine Technical Conference and Exposition*. American Society of Mechanical Engineers Digital Collection, 2013.

[101] Hans Albrecht Bethe. On the theory of shock waves for an arbitrary equation of state. In *Classic papers in shock compression science*, pages 421–495. Springer, 1998.

[102] James Serrin. The area rule for simple fluid phase transitions. *Journal of Elasticity*, 90:129–159, 2008.

[103] Hongqin Liu. The maxwell crossover and the van der waals equation of state. *arXiv preprint arXiv:2010.14739*, 2020.

[104] P Cinnella, PM Congedo, and D Laforgia. Transonic flows of bzt fluids through turbine cascades. In *Computational Fluid Dynamics 2004*, pages 227–232. Springer, 2006.

[105] MS Cramer. Nonclassical dynamics of classical gases. In *Nonlinear waves in real fluids*, pages 91–145. Springer, 1991.

[106] Luuc Keulen, Elisabeth Mansfield, Ian H Bell, Andrea Spinelli, and Alberto Guardone. Bubble-point measurements and modeling of binary mixtures of linear siloxanes. *Journal of Chemical & Engineering Data*, 63(9):3315–3330, 2018.

[107] Dimitrios A Kouremenos and Xenofon K Kakatsios. The three isentropic exponents of dry steam. *Forschung im Ingenieurwesen A*, 51(4):117–122, 1985.

[108] Pim Nederstigt. Real gas thermodynamics: and the isentropic behavior of substances, 2017.

[109] H Gray Funkhouser. A short account of the history of symmetric functions of roots of equations. *The American mathematical monthly*, 37(7):357–365, 1930.

[110] A Kluwick. Non-ideal compressible fluid dynamics: a challenge for theory. In *Journal of Physics: Conference Series*, volume 821, page 012001. IOP Publishing, 2017.

[111] Jingyi Zeng, Jie Zhu, and Feng Liu. Non-classical isentropic flow behavior of a bethe-zel'dovich-thompson gas. In *AIAA Scitech 2021 Forum*, page 0970, 2021.

[112] Jie Zhu, Jingyi Zeng, and Feng Liu. Expansion shock wave in bethe-zel'dovich-thompson fluids. In *AIAA Scitech 2020 Forum*, page 1804, 2020.

[113] CJ Long, J Hattrick-Simpers, Makoto Murakami, RC Srivastava, Ichiro Takeuchi, Vicky L Karen, and X Li. Rapid structural mapping of ternary metallic alloy systems using the combinatorial approach and cluster analysis. *Review of Scientific Instruments*, 78(7):072217, 2007.

[114] Geoffroy Hautier, Christopher C Fischer, Anubhav Jain, Tim Mueller, and Gerbrand Ceder. Finding nature's missing ternary oxide compounds using machine learning and density functional theory. *Chemistry of Materials*, 22(12):3762–3767, 2010.

[115] Stefano Curtarolo, Dane Morgan, Kristin Persson, John Rodgers, and Gerbrand Ceder. Predicting crystal structures with data mining of quantum calculations. *Physical review letters*, 91(13):135503, 2003.

[116] Ghanshyam Pilania, Chenchen Wang, Xun Jiang, Sanguthevar Rajasekaran, and Ramamurthy Ramprasad. Accelerating materials property predictions using machine learning. *Scientific reports*, 3(1):1–6, 2013.

[117] Katja Hansen, Grégoire Montavon, Franziska Biegler, Siamac Fazli, Matthias Rupp, Matthias Scheffler, O Anatole Von Lilienfeld, Alexandre Tkatchenko, and Klaus-Robert Muller. Assessment and validation of machine learning methods for predicting molecular atomization energies. *Journal of Chemical Theory and Computation*, 9(8):3404–3419, 2013.

[118] Venkat Venkatasubramanian. The promise of artificial intelligence in chemical engineering: Is it here, finally? *AIChE Journal*, 65(2):466–478, 2019.

[119] Yann LeCun, Yoshua Bengio, and Geoffrey Hinton. Deep learning. *nature*, 521(7553):436–444, 2015.

[120] Ian Goodfellow, Yoshua Bengio, and Aaron Courville. *Deep learning*. MIT press, 2016.

[121] Michael A Nielsen. *Neural networks and deep learning*, volume 25. Determination press San Francisco, CA, USA, 2015.

[122] Huimin Lu, Yujie Li, Min Chen, Hyoungseop Kim, and Seiichi Serikawa. Brain intelligence: go beyond artificial intelligence. *Mobile Networks and Applications*, 23:368–375, 2018.

[123] Geoffrey Hinton, Li Deng, Dong Yu, and George Dahl. rahman mohamed. *A., Jaitly, N., Senior, A., Vanhoucke, V., Nguyen, P., Sainath, T., and Kingsbury, B*, pages 82–97, 2012.

[124] Harsh Kukreja, N Bharath, CS Siddesh, and S Kuldeep. An introduction to artificial neural network. *Int J Adv Res Innov Ideas Educ*, 1:27–30, 2016.

[125] Frank Rosenblatt. The perceptron: a probabilistic model for information storage and organization in the brain. *Psychological review*, 65(6):386, 1958.

[126] Hao Yu and Bogdan M Wilamowski. Levenberg–marquardt training. In *Intelligent systems*, pages 12–1. CRC Press, 2018.

[127] Yong Wang. Gauss–newton method. *Wiley Interdisciplinary Reviews: Computational Statistics*, 4(4):415–420, 2012.

[128] Antony Jameson, Wolfgang Schmidt, and Eli Turkel. Numerical solution of the euler equations by finite volume methods using runge kutta time stepping schemes. In *14th fluid and plasma dynamics conference*, page 1259, 1981.

[129] J Eddie Welch, Francis Harvey Harlow, John P Shannon, and Bart J Daly. The mac method-a computing technique for solving viscous, incompressible, transient fluid-flow problems involving free surfaces. Technical report, Los Alamos National Lab.(LANL), Los Alamos, NM (United States), 1965.

[130] Suhas V Patankar and D Brian Spalding. A calculation procedure for heat, mass and momentum transfer in three-dimensional parabolic flows. In *Numerical prediction of flow, heat transfer, turbulence and combustion*, pages 54–73. Elsevier, 1983.

[131] Alexandre Joel Chorin. A numerical method for solving incompressible viscous flow problems. *Journal of computational physics*, 135(2):118–125, 1997.

[132] John Kim and Parviz Moin. Application of a fractional-step method to incompressible navier-stokes equations. *Journal of computational physics*, 59(2):308–323, 1985.

[133] Raad I Issa. Solution of the implicitly discretised fluid flow equations by operator-splitting. *Journal of computational physics*, 62(1):40–65, 1986.

[134] Marsha J Berger and Joseph Oliger. Adaptive mesh refinement for hyperbolic partial differential equations. *Journal of computational Physics*, 53(3):484–512, 1984.

[135] Chi-Wang Shu and Stanley Osher. Efficient implementation of essentially non-oscillatory shock-capturing schemes. *Journal of computational physics*, 77(2):439–471, 1988.

Appendix A

Thermodynamic Identities

A.1 Exact Differential and Triple Product Rule

In thermodynamics, there is a set of equations that are derived by the application of Euler's reciprocity relation to the thermodynamic characteristic functions. Consider a function described by three variables $z = f(x, y)$, where x, y, z may be regarded as three state variables, where any two of them may be regarded as independent and the third as a function of the other two. It can be differentiated as

$$dz = Adx + Bdy \tag{A.1}$$

The exactness criteria for this function state that

$$\left(\frac{\partial A}{\partial y}\right)_x = \left(\frac{\partial B}{\partial x}\right)_y \tag{A.2}$$

where the three variables are related by the triple product relation for a system governed by $x = x(y,z)$

$$\left(\frac{\partial x}{\partial y}\right)_z \left(\frac{\partial y}{\partial z}\right)_x \left(\frac{\partial z}{\partial x}\right)_y = -1 \tag{A.3}$$

A.2 Maxwell Relations

The general form of Gibbs equation gives that

$$du = Tds - pdv \tag{A.4}$$

$$dh = vdp + Tds \tag{A.5}$$

By applying exactness criteria, the four most common Maxwell relations are

$$\left(\frac{\partial T}{\partial v}\right)_s = -\left(\frac{\partial p}{\partial s}\right)_v \tag{A.6}$$

$$\left(\frac{\partial T}{\partial p}\right)_s = \left(\frac{\partial v}{\partial s}\right)_p \tag{A.7}$$

$$\left(\frac{\partial s}{\partial v}\right)_T = \left(\frac{\partial p}{\partial T}\right)_v \tag{A.8}$$

$$\left(\frac{\partial s}{\partial p}\right)_T = -\left(\frac{\partial v}{\partial T}\right)_p \tag{A.9}$$

A.3 Derivation of Eqn. (2.10)

Equation (2.5) states that

$$\Gamma = \frac{v^3}{2c^2}\left(\frac{\partial^2 p}{\partial v^2}\right)_s$$

To derive $\left(\frac{\partial^2 p}{\partial v^2}\right)_s$ in terms of thermodynamic state variables, start with the first order derivative along the isentrope $\left(\frac{\partial p}{\partial v}\right)_s$.

$$
\begin{aligned}
\left(\frac{\partial p}{\partial v}\right)_s &= -\left(\frac{\partial p}{\partial s}\right)_v \left(\frac{\partial s}{\partial v}\right)_p \\
&= \left(\frac{\partial T}{\partial v}\right)_s \left(\frac{\partial p}{\partial T}\right)_s \\
&= \left(\frac{\partial T}{\partial s}\right)_v \left(\frac{\partial s}{\partial v}\right)_T \left(\frac{\partial p}{\partial s}\right)_T \left(\frac{\partial s}{\partial T}\right)_p \\
&= -\frac{T}{c_v} \left(\frac{\partial p}{\partial T}\right)_v \left(\frac{\partial T}{\partial v}\right)_p \frac{c_p}{T} \\
&= -\frac{c_p}{c_v} \left(\frac{\partial v}{\partial T}\right)_p \left(\frac{\partial p}{\partial v}\right)_T \left(\frac{\partial p}{\partial v}\right)_T \left(\frac{\partial T}{\partial p}\right)_v \\
&= -\left[1 + \frac{T}{c_v} \left(\frac{\partial v}{\partial T}\right)_p \left(\frac{\partial p}{\partial T}\right)_v\right] \left[\left(\frac{\partial v}{\partial T}\right)_p \left(\frac{\partial p}{\partial v}\right)_T^2 \left(\frac{\partial T}{\partial p}\right)_v\right] \\
&= \left(\frac{\partial p}{\partial v}\right)_T + \frac{T}{c_v} \left(\frac{\partial v}{\partial T}\right)_p \left(\frac{\partial p}{\partial T}\right)_v \left(\frac{\partial p}{\partial v}\right)_T \\
&= \left(\frac{\partial p}{\partial v}\right)_T - \frac{T}{c_v} \left(\frac{\partial p}{\partial T}\right)_v^2
\end{aligned}
$$

Then another differentiation gives

$$
\begin{aligned}
\left(\frac{\partial^2 p}{\partial v^2}\right)_s &= \left(\frac{\partial \left(\left(\frac{\partial p}{\partial v}\right)_T - \frac{T}{c_v}\left(\frac{\partial p}{\partial T}\right)_v^2\right)}{\partial v}\right)_s \\
&= \underbrace{\left(\frac{\partial \left(\left(\frac{\partial p}{\partial v}\right)_s\right)}{\partial v}\right)_T}_{①} - \frac{1}{c_v}\left(\frac{\partial p}{\partial T}\right)_v^2 \underbrace{\left(\frac{\partial T}{\partial v}\right)_s}_{②} + \frac{T}{c_v^2}\left(\frac{\partial p}{\partial T}\right)_v^2 \underbrace{\left(\frac{\partial c_v}{\partial v}\right)_s}_{③} - \frac{2T}{c_v}\left(\frac{\partial p}{\partial T}\right)_v \underbrace{\left(\frac{\partial \left(\left(\frac{\partial p}{\partial v}\right)_s\right)}{\partial T}\right)_v}_{④}
\end{aligned}
$$

The four terms marked in the equation above are derived below. To keep the expression elegant, here $\partial/\partial T$ implies that v is kept constant, and vice versa.

$$
\begin{aligned}
① &= \frac{\partial^2 p}{\partial v^2} + \frac{T}{c_v^2}\left(\frac{\partial p}{\partial T}\right)^2 \frac{\partial c_v}{\partial v} - \frac{2T}{c_v}\frac{\partial p}{\partial T}\frac{\partial^2 p}{\partial v \partial T} \\
② &= -\frac{T}{c_v}\frac{\partial p}{\partial T} \\
③ &= \frac{\partial c_v}{\partial v} - \frac{T}{c_v}\frac{\partial p}{\partial T}\frac{\partial c_v}{\partial T} \\
④ &= \frac{\partial^2 p}{\partial v \partial T} - \frac{1}{c_v}\left(\frac{\partial p}{\partial T}\right)^2 + \frac{T}{c_v^2}\left(\frac{\partial p}{\partial T}\right)^2 \frac{\partial c_v}{\partial T} - \frac{2}{c_v}\frac{\partial p}{\partial T}\frac{\partial c_v}{\partial v}
\end{aligned}
$$

Substitute the above expressions back into $\left(\frac{\partial^2 p}{\partial v^2}\right)_s$ and reorganize the equation, we obtain

$$
\left(\frac{\partial^2 p}{\partial v^2}\right)_s = \frac{\partial^2 p}{\partial v^2} - \frac{3T}{c_v}\frac{\partial p}{\partial T}\frac{\partial^2 p}{\partial v \partial T} + \left(\frac{T}{c_v}\frac{\partial p}{\partial T}\right)^2 \left[\frac{3}{T}\frac{\partial c_v}{\partial v} + \frac{1}{T}\frac{\partial p}{\partial T}\left(1 - \frac{T}{c_v}\frac{\partial c_v}{\partial T}\right)\right] \tag{A.10}
$$

A.4 Derivation of Eqn. (2.13)

The first step involves the definitions of specific heat capacities at constant pressure, represented by c_p, and at constant volume, represented by c_v. These are mathematically expressed as follows

$$
c_p = T\left(\frac{\partial s}{\partial T}\right)_p \tag{A.11}
$$

$$
c_v = T\left(\frac{\partial s}{\partial T}\right)_v \tag{A.12}
$$

By subtracting Equation A.12 from Equation A.11, we obtain

$$
c_p - c_v = T\left[\left(\frac{\partial s}{\partial T}\right)_p - \left(\frac{\partial s}{\partial T}\right)_v\right] \tag{A.13}
$$

Subsequently, express the entropy change of the system in terms of dT and dv

$$ds = \left(\frac{\partial s}{\partial T}\right)_v dT + \left(\frac{\partial s}{\partial v}\right)_T dv \tag{A.14}$$

In a similar fashion, dv is expressed in terms of dp and dT

$$dv = \left(\frac{\partial v}{\partial T}\right)_p dT + \left(\frac{\partial v}{\partial p}\right)_T dp \tag{A.15}$$

Substitute Equation A.15 into Equation A.14

$$ds = \left[\left(\frac{\partial s}{\partial T}\right)_v + \left(\frac{\partial s}{\partial v}\right)_T \left(\frac{\partial v}{\partial T}\right)_p\right] dT + \left(\frac{\partial s}{\partial v}\right)_T \left(\frac{\partial v}{\partial p}\right)_T dp \tag{A.16}$$

By comparing Equation A.16 with Equation A.14, we can deduce that

$$\left(\frac{\partial s}{\partial T}\right)_p = \left(\frac{\partial s}{\partial T}\right)_v + \left(\frac{\partial s}{\partial v}\right)_T \left(\frac{\partial v}{\partial T}\right)_p \tag{A.17}$$

Finally, we arrive at the following expression

$$c_p - c_v = T \left(\frac{\partial v}{\partial T}\right)_p \left(\frac{\partial p}{\partial T}\right)_v \tag{A.18}$$